BEAM DYNAMICS DESIGN OF AN ENERGY-VARIABLE SUPERCONDUCTING HEAVY ION ACCELERATOR

DISSERTATION ZUR ERLANGUNG DES DOKTORGRADES DER NATURWISSENSCHAFTEN

vorgelegt am Fachbereich Physik
der Johann Wolfgang Goethe-Universität
in Frankfurt am Main

von
Malte Alexander Schwarz
aus
Frankfurt am Main

Frankfurt am Main, 2021
(D30)

vom Fachbereich Physik der Johann Wolfgang Goethe-Universität als Dissertation angenommen.

DEKAN:
Prof. Dr. Harald Appelshäuser

1. GUTACHTER:
Prof. Dr. Holger Podlech

2. GUTACHTER:
Prof. Dr. Ulrich Ratzinger

DATUM DER DISPUTATION:
08.11.2021

Malte Alexander Schwarz: *Beam Dynamics Design of an Energy-Variable Superconducting Heavy Ion Accelerator*, 2021

This work is licensed under a Creative Commons Attribution 4.0 International License (CC BY 4.0). To view a copy of this license, visit http://creativecommons.org/licenses/by/4.0/.

ZUSAMMENFASSUNG

Diese Dissertation beschreibt die Entwicklung des Strahldynamikdesigns eines neuartigen supraleitenden Linearbeschleunigers (Linacs). Bei einer Haupt-Betriebsfrequenz von 216,816 MHz können dabei Ionen mit einem Masse-zu-Ladungsverhältnis von bis zu 6 bei hohen Tastverhältnissen bis hin zum CW-Betrieb beschleunigt werden. Angedacht für einen Bau am GSI Helmholtzzentrum für Schwerionenforschung in Darmstadt lag der Schwerpunkt der Arbeit in der strahldynamischen Auslegung des Beschleunigerabschnitts nach dem Hochladungsinjektor (HLI) bei einer Injektionsenergie von 1,39 MeV/u. Wesentliches Merkmal dieses Linacs ist dabei die Verwendung des EQUUS (Equidistant Multigap Structure) Strahldynamikkonzeptes für eine variabel einstellbare Ausgangsenergie zwischen 3,5 und 7,3 MeV/u (entspricht etwa 12,4 % der Lichtgeschwindigkeit) bei einer erforderlichen geringen Energieunschärfe von maximal ± 3 keV/u.

Das GSI Helmholtzzentrum für Schwerionenforschung ist eine Großforschungseinrichtung, die mit ihren Teilchenbeschleunigern Grundlagenforschung mit Ionenstrahlen durchführt, insbesondere um neue Erkenntnisse über die Bausteine der Materie zu gewinnen. Seit seiner Gründung 1969 wird an der GSI auf einem breiten Themenfeld, von Kernphysik, Atomphysik, Plasmaphysik und Materialwissenschaften bis hin zu Biophysik und Tumortherapie mit einem ebenso breiten Spektrum an Ionensorten von Helium bis Uran geforscht. Nach der Gründung begann der Bau des 150 Meter langen Linearbeschleunigers UNILAC. Als Erweiterungen sind seit 1990 das Schwerionen-Synchrotron SIS18 und der Experimentelle Speicherring ESR in Betrieb. Um weitere fundamentale Fragen zum Aufbau der Materie und des Universums untersuchen zu können, wird an der GSI aktuell eine internationale Forschungsanlage namens FAIR (engl. *Facility for Antiproton and Ion Research*) für die Forschung mit Antiprotonen und Ionen gebaut. Die bestehende Beschleunigeranlage an der GSI wird dann als Injektor für die FAIR-Beschleunigeranlage dienen, wobei FAIR Ionenstrahlen mit bisher unerreichten Intensitäten und Energien für die Forschung bereitstellen soll. Zu diesem Zweck werden einige der bestehenden GSI-Anlagen aufgerüstet bzw. erweitert.

Forschung zu superschweren Elementen („SHE“ von engl. *superheavy element*) ist ein wesentlicher Schwerpunkt an der GSI. Während Uran das schwerste Element ist, das in signifikanten Mengen in der Natur vorkommt, erwartet man von der Produktion und Erforschung noch schwererer Elemente Antworten auf eine Vielzahl wissenschaftlicher Fragestellungen. Dies beginnt bei grundlegenden Fragen zur Herkunft von Atomkernen und Elementen und deren Erzeugung im

Kosmos, über die Langlebigkeit superschwerer Elemente und deren chemischen Eigenschaften, bis hin zur Frage nach fundamentalen Symmetrien der Natur und wo das Periodensystem der Elemente möglicherweise endet. Viele Eigenschaften von Atomkernen lassen sich in einem makroskopischen Ansatz durch das Tröpfchenmodell des Atomkerns erklären, welches Anfang der 1930er Jahre von G. Gamow, H. Bethe und C. F. von Weizsäcker entwickelt wurde. Es basiert auf einer starken Anziehungskraft zwischen den Nukleonen und der abstoßenden elektrischen Kraft, die auf die Protonen wirkt. Nach diesem Modell sollte es Elemente mit Ordnungszahlen (Protonenzahlen) größer als $Z \approx 100$ nicht geben, da ab hier die elektrische Abstoßung die Anziehung der Kernkraft überwiegt.

Das Tröpfchenmodell kann jedoch das Phänomen der sogenannten magischen Zahlen nicht erklären. Durch präzise Massenmessungen ist bekannt, dass bei bestimmten Protonen- und Neutronenzahlen die Kerne gegenüber dem Durchschnittstrend besonders stabil gebunden sind. Dies ist auf eine erhöhte Bindungsenergie zurückzuführen. Am stabilsten ist diese Bindung bei den doppelt magischen Kernen, wie ^{208}Pb mit 82 Protonen und 126 Neutronen. Eine Erklärung war erst Ende der 1940er Jahre mit dem Schalenmodell für den Atomkern, vor allem durch M. Goeppert-Mayer und J. H. D. Jensen, möglich. Ab den 1950er Jahren wurden mit diesem Modell die nächsten magischen Zahlen („magische Schalenabschlüsse“) jenseits von ^{208}Pb berechnet, und das Konzept der superschweren Elemente wurde eingeführt.

Der Begriff „superschwer“ ist in der Literatur nicht einheitlich definiert. Üblicherweise bezeichnet er die Elemente der Transactinoiden mit Werten zwischen $Z \geqslant 103$ und $Z \geqslant 114$. Alle derzeit bekannten superschweren Kerne sind radioaktiv und wurden in Kernreaktionen erzeugt. Die Produktion und der Nachweis der Elemente mit den Ordnungszahlen 107 bis 112 (Bohrium, Hassium, Meitnerium, Darmstadtium, Röntgenium und Copernicium) gelang in den Jahren 1981 bis 1996 erstmals an der GSI. Hierzu wurden Atome einer Sorte („Projektile“) auf Energien beschleunigt, die hoch genug sind, um sich einem Atom einer anderen Sorte bzw. dessen Atomkern („Target“) so weit zu nähern, dass die abstoßende Coulombbarriere (Größenordnung je nach Atomkern in etwa 10^0-10^1 MeV/u) überwunden wird. Die beiden wechselwirkenden Kerne entwickeln sich zu einem Compoundkern. Im günstigsten Fall kommt es nun weder zu einem Zerfall in die ursprünglichen Kerne, noch zu einer Quasi-Spaltung, sondern zur Aussendung von γ-Strahlen und der Abdampfung eines oder mehrerer Neutronen mit anschließender Bildung eines Verdampfungsrestkerns. Dies ist dann der Kern des gesuchten superschweren Elements, dessen Nachweis über den radioaktiven Zerfall zu bekannten Kernen und Elementen möglich ist.

Zentral für diese bemerkenswerten Fortschritte in der SHE Forschung waren kontinuierliche Weiterentwicklungen und technische

Innovationen. Einerseits auf dem Feld der experimentellen Sensitivität und Detektion der Kernreaktionsprodukte und andererseits auf dem Gebiet der Beschleunigertechnologie. Zur Beschleunigung des Projektilstrahls wird an der GSI bislang der 1975 in Betrieb genommene UNILAC (für engl. *Universal Linear Accelerator*) verwendet. Im Zuge des Umbaus und der Erweiterung der Forschungsinfrastruktur an der GSI für die künftige FAIR-Anlage befindet sich mit HELIAC (für engl. *Helmholtz Linear Accelerator*) nun auch ein dedizierter neuer Teilchenbeschleuniger in der Entwicklung, der die besonderen Erfordernisse der Strahlparameter zur Synthese neuer superschwerer Elemente berücksichtigt. Typischerweise sind die Produktionsraten superschwerer Elemente mit Wirkungsquerschnitten im Bereich von picobarn sehr niedrig. Daher ist ein hohes Tastverhältnis (bis hin zum CW-Betrieb) ein wesentliches Merkmal des HELIAC. So lässt sich die benötigte Strahlzeit für die gewünschten Kernreaktionen signifikant verkürzen.

Erste Überlegungen für einen dedizierten Linearbeschleuniger (Linac) für die Forschung zu SHE an der GSI wurden in Workshops in den frühen 2000er Jahren international diskutiert. 2009 veröffentlichten Minaev *et al.* einen ersten vorläufigen Entwurf für das strahldynamische Design eines entsprechenden Linacs. Dieser sollte supraleitend konzipiert sein, um hohe Beschleunigungsgradienten bei gleichzeitig hohem Tastverhältnis zu ermöglichen. Der Schwerpunkt dieser Forschungsarbeit lag jedoch auf der Analyse und theoretischen Beschreibung des EQUUS-Strahldynamikkonzepts sowie auf der rudimentären Untersuchung, ob dieses Konzept grundsätzlich für einen solchen Beschleuniger in Frage kommt. Im vergangenen Jahrzehnt hat daran anschließend die Erforschung und Entwicklung von supraleitenden Beschleunigerkavitäten viele Erkenntnisse geliefert. So wurden am IAP erfolgreich mehrere Prototypen für supraleitende CH-DTLs entwickelt und getestet. Hierbei wurden mehrfach weltweite Spitzenwerte für die Beschleunigungseffizienz im Nieder- und Mittelenergiebereich aufgestellt. Weiterentwicklungen gab es dabei insbesondere an der Resonatorgeometrie mit Schwerpunkten auf einem kompakten Design, effektivem Frequenztuning, günstigen Präparationsmöglichkeiten und bei dem Design von Leistungskopplern für den Strahlbetrieb. So haben letztlich die theoretischen Vorarbeiten von Minaev *et al.* und das neu geschaffene Wissen um Design, Herstellung und Betrieb von supraleitenden Driftröhrenkavitäten den Grundstein für diese Arbeit und somit die Entwicklung des Linearbeschleunigers HELIAC gelegt.

Als Injektor für HELIAC dient der GSI-Hochladungsinjektor HLI. Dieser wird aktuell für die künftigen Anforderungen aufgerüstet und erhält eine neue 18 GHz Elektronenzyklotron-Resonanz-Ionenquelle (ECR), einen neuen CW-fähigen Radiofrequenz-Quadrupol (RFQ) sowie einen neuen IH-Driftröhrenbeschleuniger mit einer HF-Betriebsfrequenz von 108,408 MHz. HELIAC besteht aus einem supraleitenden und einem normalleitenden Teil. Die Beschleunigung findet im su-

praleitenden Teil bei einem Frequenzsprung auf 216,816 MHz in vier Kryomodulen mit jeweils etwa 5 m Länge statt. Diese beinhalten je drei CH-Kavitäten, eine Buncher-Kavität vom Single-Spoke-Typ, zwei Solenoidmagnete zur transversalen Strahlfokussierung, sowie zwei Strahlpositionsmonitore (kurz BPM für engl. *beam position monitor*).

Der dann folgende etwa 10 m lange normalleitende Teil dient primär zum Strahltransport und schließt mit einer Buncherkavität ab. Diese wird mit einer halbierten Frequenz von 108,408 MHz betrieben, um von dem durch die Frequenzhalbierung verlängerten quasi-linearen Teil der HF-Flanke profitieren zu können. Dies schafft eine größere Flexibilität bei der Transformation des Strahls im longitudinalen Phasenraum hin zur benötigten Energieschärfe.

2016 haben F. Dziuba *et al.* erfolgreich Kalttests an einer am IAP entwickelten 15-spaltigen CH-Struktur durchgeführt. 2018 folgte dann mit der gleichen Kavität durch W. Barth *et al.* an der GSI der weltweit erste Strahlbetrieb einer vielspaltigen supraleitenden Driftröhrenkavität, so dass diese CH-Struktur als erste von 12 CH-Kavitäten des HELIAC eingesetzt werden kann.

Wesentliches Merkmal dieses Beschleunigers ist die Variabilität der Ausgangsenergie von 3,5 bis 7,3 MeV/u bei einer geringen Energieunschärfe von maximal ± 3 keV/u über den gesamten Ausgangsenergiebereich hinweg. Üblicherweise wird die Energievariation entlang der Beschleunigungsstrecke durch Aneinanderreihung kurzer Kavitäten mit möglichst wenigen Beschleunigungsspalten realisiert. So ist die Energieakzeptanz jeder Kavität verhältnismäßig groß, es lassen sich viele HF-Amplituden und -Phasen individuell regeln und das Strahldynamikdesign ist unkompliziert. Die Beschleunigungseffizienz ist dagegen bei diesem Verfahren gering, da mit einer großen Anzahl an Kavitäten auch viele Driftstrecken einhergehen, in denen der Strahl nicht beschleunigt wird. Für die Entwicklung von HELIAC wurden mit dem verwendeten EQUUS-Strahldynamikkonzept daher die Vorteile konventioneller Linac-Designs mit dem hohen Beschleunigungsgradienten von supraleitenden CH-DTLs kombiniert. Die Auslegung und Simulation der Strahldynamik wurde mit dem Simulationscode LORASR durchgeführt, der am IAP ständig weiterentwickelt wird. Durch den Frequenzsprung auf 216,816 MHz in der supraleitenden Sektion und die Verwendung von CH-Kavitäten mit 5 (CH10 und CH11) bis 15 (CH0) Beschleunigsspalten bei einem Beschleunigungsgradienten von maximal 7,1 MV/m wird eine weltweit bislang einmalige Beschleunigungseffizienz mit supraleitenden Driftröhrenstrukturen ermöglicht. Gleichzeitig wird mit kompakten Längen der CH-Kavitäten von 59–81 cm ein dennoch gutes Handling sowohl für die Fertigung als auch den Betrieb gewährleistet. EQUUS führt mit der gleitenden Bewegung der Synchronphase innerhalb jeder CH-Kavität zu longitudinaler Strahlstabilität in allen Energiebereichen des Beschleunigers. Das rms-Emittanzwachstum ist in allen

Ebenen mit $+10\,\%$ (xx'), $+11\,\%$ (yy') und $+14\,\%$ (zz') moderat. Der modulare Aufbau des HELIAC mit 4 Kryomodulen ermöglicht die Inbetriebnahme des Beschleunigers grundsätzlich bereits ab dem ersten Kryomodul, dem sogenannten Advanced Demonstrator. In der darauffolgenden Ausbaustufe mit lediglich den ersten beiden Kryomodulen des HELIAC, kann bereits die untere Grenze des von HELIAC zur Verfügung zu stellenden Energiebereiches ($3,5\,\mathrm{MeV/u}$) deutlich übertroffen werden, so dass die Verwendung im regulären Strahlbetrieb an der GSI ab hier bereits denkbar ist.

Mittels Fehlertoleranzstudien konnte die Stabilität des HELIAC-Strahldynamikdesigns gegenüber möglicher Justierfehler der magnetischen Fokussierelemente und Beschleunigerkavitäten sowie Fehler der elektrischen Feldamplituden und -phasen untersucht und kritische Parameter ermittelt werden. Ein zusätzliches Steeringkonzept über Dipolkorrekturspulen an den Solenoidmagneten erlaubt eine transversale Strahlsteuerung sowie -diagnose mittels zweier BPMs pro Kryomodul. Letztlich zeigte sich sowohl bei Betrachtung einzelner als auch kombinierter Fehlertypen eine ausreichende Strahlstabilität gegenüber zu erwartender Abweichungen. Mittels eines zweiten Simulationscodes (TraceWin) konnte die HELIAC-Strahldynamik zudem grundsätzlich verifiziert werden.

Parallel zu den unmittelbaren Arbeiten am Strahldynamikdesign von HELIAC wurde mit der Entwicklung des Java-basierten Computerprogramms LINAC-Multitool ein Werkzeug geschaffen, um Routineaufgaben im Beschleunigerbereich zu automatisieren und zu vereinfachen. So können nun Störkörpermessungen, als zentrale Prozedur bei der Werksabnahme von gefertigten Kavitäten, effizient über eine grafische Benutzeroberfläche steuerbar, ausgewertet werden. Auch der Designprozess mit dem Strahldynamikprogramm LORASR gestaltet sich dank einer umfassenden Erweiterung der Plotting-Funktionalitäten über das LINAC-Multitool nun wesentlich komfortabler.

Mit Fertigstellung dieser Arbeit im Sommer 2021 wurden die Kavitäten CH1 und CH2 bereits gebaut und befinden sich in der finalen Präparations- und Kalttestphase. Parallel wurde die Entwicklung der CH-Kavitäten CH3–11 auch gestartet. Der Erfolg dieses Strahldynamik-Designs hängt letztlich insbesondere von der Leistungsfähigkeit der Kavitäten ab. Das zuverlässige Erreichen der hohen Beschleunigungsgradienten in den CH-Kavitäten ist der wichtigste Schlüssel zu diesem ehrgeizigen Projekt. Angesichts der großen Fortschritte auf diesem Forschungsgebiet im letzten Jahrzehnt ist dies sicherlich ein anspruchsvolles, aber erreichbares Beschleunigervorhaben. Somit ist die hier dargelegte Entwicklung eines effizienten, supraleitenden Linearbeschleunigers mit variabler Ausgangsenergie und hohem Tastverhältnis auch von Interesse für die Auslegung zukünftiger vergleichbarer Anlagen zur Beschleunigung von Ionenstrahlen.

CONTENTS

LIST OF FIGURES

LIST OF TABLES

ACRONYMS

APF	Alternating phase focusing
BPM	Beam position monitor
CH	Crossbar *H*-mode (DTL cavity)
CM	Cryomodule
CW	Continuous-wave
DTL	Drift-tube linac
EQUUS	Equidistant multi-gap structure
FB	Final buncher cavity
FFT	Fast Fourier transformation
GSI	GSI Helmholtz Centre for Heavy Ion Research, Darmstadt, Germany
GUI	Graphical user interface
HELIAC	Helmholtz linear accelerator
HIM	Helmholtz Institute Mainz, Mainz, Germany
HLI	High Charge-state Injector (ger. *Hochladungsinjektor*) at GSI
HWR	Half-wave resonator
IAP	Institute of Applied Physics, Goethe University Frankfurt, Germany
IH	Interdigital *H*-mode (DTL cavity)
KONUS	Combined zero degree structure (ger. *Kombinierte Null Grad Struktur*)
LINAC	Linear accelerator
LORASR	Longitudinal and Radial Beam Dynamics Calculations including Space Charge (ger. *Longitudinale und radiale Strahldynamikrechnungen mit Raumladung*)
NC	Normal conducting (in terms of electrical resistance)
PIC	Particle-in-cell
QWR	Quarter-wave resonator

RF	Radio frequency
RMS	Root mean square
SC	Superconducting
SHE	Super-heavy element
SRR	Split-ring resonator
SSR	Single-spoke resonator

1 INTRODUCTION

1.1 MOTIVATION AND RESEARCH CONTEXT

In 1869 Russian chemistry professor Dmitri Mendeleev[1] devised the periodic table of elements. Since then it was continuously refined. In the last decades it has been significantly extended up to the nucleon with proton number $Z = 118$ and mass number $A = 294$, named oganesson. Historically, the periodic table was of particular importance for predicting as yet undiscovered elements and their properties. Today, it serves primarily as an organizational scheme of the elements, as framework for analyzing chemical reactions, and is widely used in chemistry and nuclear physics. While uranium ($Z = 92$) is the heaviest element found in significant quantities in nature, the production and exploration of even heavier elements is expected to provide answers to many scientific questions [1] and is therefore of high scientific interest [2]. The work summarized in this thesis is specifically concerned with the synthesis of so-called *super-heavy elements* (SHE), the definition of which is not uniform but assumes at least a proton number $Z \geqslant 103$ [3].

For the synthesis of SHE fusion-evaporation reactions of accelerated medium or heavy ions with heavy-element targets have recently been the most successful methods [4]. Due to the very low cross sections of these reactions, long beam times are required in order to observe a sufficient number of events. Obviously, a higher experimental sensitivity and an increased projectile intensity, especially in continuous wave (CW) mode, could remarkably enhance the SHE yield [5–7].

For that purpose, this thesis has been started to develop and investigate possible beam dynamics layouts of a future machine for an efficient SHE-production. As a result, the development of the heavy ion superconducting CW linac HELIAC (HElmholtz LInear ACcelerator) has been started. It will be built at GSI Helmholtz Centre for Heavy Ion Research at Darmstadt under key support of the Helmholtz Institute Mainz (HIM) [8–10] and the Institute of Applied Physics (IAP) at Goethe University Frankfurt [11, 12] and with contributions from Moscow Engineering Physics Institute (MEPhI) and Moscow Institute for Theoretical and Experimental Physics (KI-ITEP) [13, 14].

The construction and operation of CW-operated proton and ion linacs are key goals of the worldwide accelerator development. Large-scale facilities [15–17], such as spallation neutron sources (SNS) or

1 in Russian (modern Cyrillic script): Дмитрий Иванович Менделеев; transliteration: *Dmitriy Ivanovich Mendeleyev*

accelerator driven systems (ADS) are based essentially on high-energy CW linacs. Medium-energy superconducting CW linacs are used or investigated for numerous applications [18], i. e. particle physics, nuclear astrophysics, material science, R&D of radiopharmaceuticals, neutron radiography and novel cancer therapy methods (accelerator-based boron-neutron capture therapy) [19–21]. Consequently, further elaboration of superconducting RF technology [22–24] and in particular the development of linacs using this technology is of high relevance for the particle accelerator community.

The most essential element of the developed accelerator design in this thesis is the use of superconducting multigap CH-DTL cavities which allow very high acceleration gradients of 7 MV/m and beyond [8]. While the IH-DTL structure is already well known for its high shunt impedance at low-β values [25, 26], the CH-DTL structure derived from it offers new properties. With operation in the $H_{21(0)}$ mode, the transverse cavity dimensions are significantly larger than that of the IH-cavity at a given frequency and beam velocity, allowing the operation at higher frequencies. Especially the mechanical rigidity makes it also suitable for superconducting operation. Superconducting CH-cavities have been developed and continuously improved at IAP for about 20 years [27]. Following previous work by Minaev et al. [28] and incorporating new research outcomes and findings from recent years, this sets the baseline for this work.

Part I

OVERVIEW AND THEORY

2 BEAM DYNAMICS

In this chapter, fundamentals of the main beam dynamics principles of heavy ion linacs are presented. RF linacs operate by accelerating electrically charged particles with longitudinal electric fields generated in a resonant cavity. The motion of particle bunches in the transverse and longitudinal planes is summarized under the term **beam dynamics**. More in-depth descriptions of accelerator physics can be found in *RF Linear Accelerators* by T. P. Wangler [29] and in the regularly and open-access[1] published *Proceedings of the CAS – CERN Accelerator School*. For further discussions on the subject of beam dynamics, the book *Theory and design of charged particle beams* by M. Reiser [30] is highly recommended.

Details on the cavity research and development, in particular on the mechanical design of the superconducting HELIAC accelerator cavities of the CH-DTL type can be found in the PhD theses of F. Dziuba [31] (for CH0) and M. Basten [32] (focusing on CH1/2) as well as for CH3–CH11 in [33] and [34].

2.1 CHARACTERIZATION OF A PARTICLE BEAM

The term *particle beam* (or in other words *beam*) is used in this thesis to refer to an ensemble of similar particles, for which the following applies:

$$v_z \gg v_x, y. \tag{2.1}$$

The longitudinal velocity component v_z is thus significantly larger than the transverse ones v_x (horizontal) and v_y (vertical).

Figure 2.1 schematically depicts the general time structure of bunched beams in pulsed operation. Here, the smallest unit is the *particle bunch*, also referred to as *bunch*. In principle, individual bunches are initially spaced by one RF period T_{RF}, which is the inverse of the linac operating frequency f:

$$T_{\mathrm{RF}} = f^{-1}. \tag{2.2}$$

Several bunches form a pulse with the pulse length τ and the average pulse current I_{pulse}, in the following referred to as *beam current*. The beam current plays an important role in the strength of the *space charge forces*. These have a repulsive effect in a bunch due to the equally electrically charged particles and defocus the beam. At the same time the movement of the charged particles along the beam axis z generates an azimuthal magnetic field component B' which has

1 https://cas.web.cern.ch

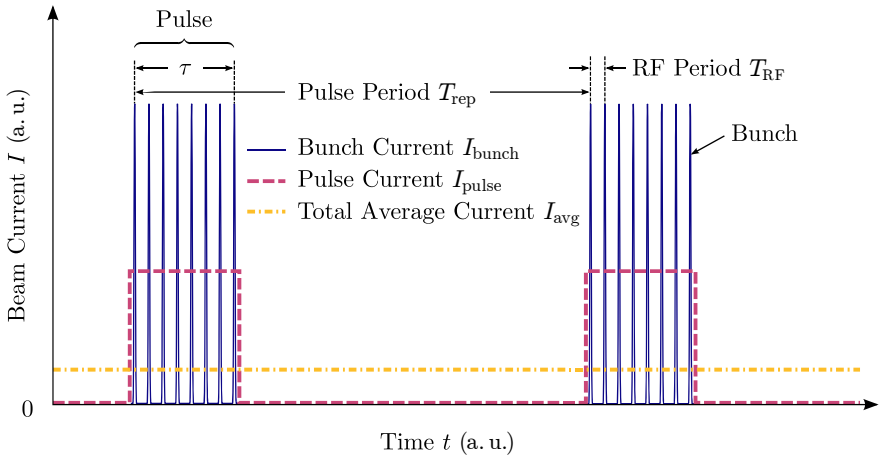

Figure 2.1: Definition of different beam currents and time structures.

an attractive effect. However, its influence only becomes relevant for highly relativistic beams and is not relevant for the investigations in this work at $\beta = v/c \ll 1$. Here v is the particle velocity and c the vacuum velocity of light.

The *duty cycle* D of the beam is defined as

$$D = \frac{\tau}{T_{\text{rep}}} \cdot 100\,\%. \tag{2.3}$$

If the linac continuously accelerates the beam the duty cycle equals 100 % and the linac is said to operate in *continuous wave* (CW) mode.

2.1.1 *Emittance*

While the motion of a single electrically charged particle (i. e. $N = 1$) in external electromagnetic fields can be specified compactly and unambiguously via its position in the 6-dimensional phase space $(x,\ p_x,\ y,\ p_y,\ z,\ p_z)$, the complete description and measurement of a particle ensemble $N \gg 1$ requires an extended concept. Although the motion of each individual particle over a single point in the $6N$-dimensional phase space could also be described, it is usually more useful and efficient to view the particle ensemble as a whole and in two-dimensional subspaces to simplify handling. For the description of a beam, the divergence angle x' in rad is often chosen instead of the transverse momentum p_x:

$$x' = \frac{dx}{dz} = \frac{v_x}{v_z} = \frac{p_x}{p_z} = \tan\theta_x. \tag{2.4}$$

In general (see Equation 2.1) the divergence angle θ_x is small, so the paraxial approximation $\tan\theta_x \approx \theta_x$ can be used, and therefore $x' \approx \theta_x$. This applies accordingly and, in the following, also to the transverse components in y. In the phase space consisting of x and x', all N

particles can now be represented with their corresponding spatial coordinates and angles. For easy detection of the occupied area in this phase space, the particle distribution can be surrounded by an ellipse in such a way that all beam particles are enclosed with a minimum area A. The emittance ε_x is obtained as

$$\varepsilon_x = \frac{A_x}{\pi}, \tag{2.5}$$

with the phase-space area A_x:

$$A_x = \iint dx\, dx' = \varepsilon_x \pi\,. \tag{2.6}$$

This (often elliptical) area in 2-dimensional phase space A_x resp. the emittance ε_x is conserved when **Liouville's theorem** is satisfied and when the forces in the three orthogonal directions are uncoupled. However, a prerequisite for calculating the motion in these subspaces is the neglect or external description of particle-particle interactions and horizontal and vertical planes that are not coupled with each other. In particular, the latter is in principle not given in drift-tube accelerators, since the longitudinal electric field component and thus the acceleration of the particle is a function of the transverse position.

*The **Liouville Theorem** states that the volume occupied by a given number of particles in phase space is invariant with respect to canonical transformations. It applies for the time evolution of a particle beam in the 6D phase space, given that there are no binary collisions, no dissipative forces and no particle losses or charge exchanges. For further details see [29] and [30].*

For use in beam dynamics simulations, a 6-dimensional (6D) particle distribution is usually generated such that the particles randomly populate a 6D hyperellipsoid. The most common distributions are:

- **KV-distribution**[2] which has homogeneously filled ellipses in the 2D projections (e. g. xx') so that the forces resulting from the electric beam potential are linear,
- the **Gaussian distribution** where the 6D hyperellipsoid is filled with a 6D Gaussian density distribution, which also implies that the 2D projections are Gaussian in shape,
- and the **Waterbag distribution** which is a 6D hyperellipsoid homogeneously filled with particles.

Simulations in this thesis have been done with Waterbag distributions for the input beam as they were considered to be the most suitable approximations available.

2.1.2 *Twiss Parameters*

As parameter to determine the beam quality and to better describe the size and position of the distributions in the 2D phase space, ellipses can be defined, which enclose all or a certain fraction of the particles in the phase space (see Figure 2.2). These ellipses can be characterized

2 named by I. M. **K**apchinskij and V. V. **V**ladimirskij [35]

by the so-called *Twiss* or *Courant-Snyder* parameters, corresponding to the equations

$$\gamma x^2 + 2\alpha x x' + \beta x'^2 = \varepsilon_x \tag{2.7}$$

and

$$\gamma = \frac{1+\alpha^2}{\beta}, \tag{2.8}$$

where α, β and γ are the Twiss parameters and ε_x is the emittance of the ellipse [29]. The parameter α is dimensionless and refers to the tilt of the ellipse. If $\alpha = 0$, the ellipse is not tilted, if $\alpha > 0$ or $\alpha < 0$, the ellipse is tilted counterclockwise or clockwise respectively.

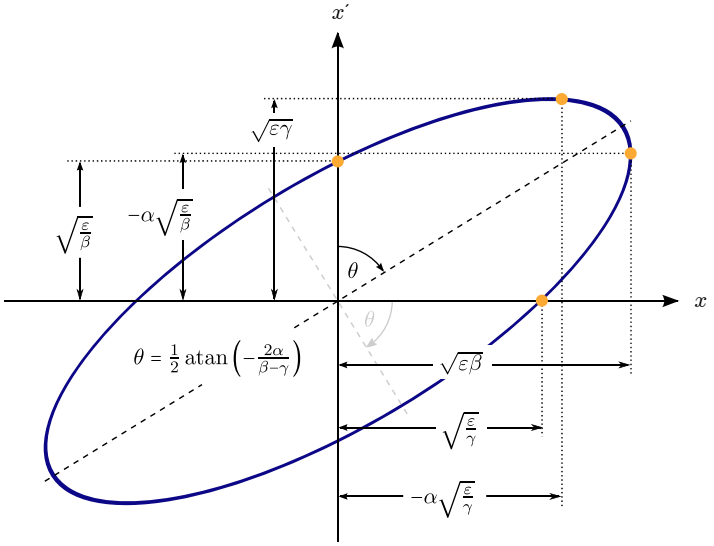

Figure 2.2: Geometrical relations of the Twiss parameters and the corresponding ellipse in the xx' 2D phase space. The enclosed area is $A = \pi\varepsilon$.

2.1.3 *Emittance Growth*

As a measure of beam quality, one of the goals of beam dynamics designs is to limit the growth of emittance during beam acceleration and transport. In this context, according to Fraser [36] the sources of emittance growth can be classified in several groups:

- **Couplings:** The emittance transfer between coupled phase space planes (e. g. transversal ↔ longitudinal) can cause the emittance in a particular phase space plane (e. g. xx') to increase, even though the total 6-dimensional phase space volume remains invariant. This is the case in DTL-cavities due to the phase dependence of the transverse RF defocusing (see Section 2.2.2). It results in a different transverse force on the front and back part of a bunch when traversing the cavity gaps. Another example are asymmetric beams (with respect to their horizontal and vertical

dimensions) whose projected emittance oscillates when they are rotated in solenoids.

- **Imperfections:** E. g. misalignment of components, manufacturing errors and dynamic errors such as RF-jitter or beam current variations.
- **Non-linearities:** Non-linear fields, e. g. as a function of the distance x or y to the ideal beam axis, resulting in a filamented or distorted phase space such that the effective emittance is increased. This also applies to the particularly non-linear regions of the RF waveform (also compare Figure 4.22 on page 60) near $\varphi = 0°$. This is the key source of emittance growth for EQUUS. Furthermore, intrinsic aberrations of optical elements (for the superconducting HELIAC part: Solenoids) can introduce non-linearities and increase the effective beam emittance.
- **Parametric resonances:** Single-particle resonances and space-charge driven transverse parametric resonances (see also Section 2.2.1).

2.2 TRANSVERSE BEAM DYNAMICS

2.2.1 *Space Charge*

The particle motion in a linac depends not only on the applied external fields from the RF or magnetic lenses, but also on the fields from the Coulomb interactions between the particles within a bunch due to their electrical charge Q. These have a repulsive effect due to the equally charged particles within a bunch and therefore defocus the beam. For HELIAC, this effect becomes visible when comparing the transverse emittance growth for different beam currents (see Figure 2.3). Nevertheless, since the maximum beam current of $I = 1\,\mathrm{mA}$ at HELIAC is still relatively small - compared to other hadron accelerator projects - the influence of space charge effects on the beam plays a rather minor role here. Nevertheless, since space charge forces act inversely proportional to the particle mass - as shown below - attention should be paid to their effect at decreasing mass-to-charge ratios[3] A/z. In order to estimate the strength of acting space charge forces, the *generalized perveance* K for non-relativistic beams is defined as [30]

mass-to-charge ratio A/z

$$K = \frac{QI}{2\pi\epsilon_0 m v^3}, \tag{2.9}$$

3 The symbol used for the mass-to-charge ratio in this thesis is A/z (dimensionless), referring to A as *atomic mass number* respectively *nucleon number* and z as *charge number* being the electric charge Q in Coulombs divided by the elementary-charge constant e. Other common terms used in literature are also A/q, A/Q, m/q and m/z.

where ϵ_0 is the vacuum permittivity, m the particle mass and v its velocity. After passing an accelerating voltage U_a, v can be substituted ($v = \sqrt{U_a 2Q/m}$) and Equation 2.9 can therefore be written as

$$K = \frac{1}{4\pi\epsilon_0}\sqrt{\frac{m}{2Q}}\frac{I}{U_a^{3/2}}. \tag{2.10}$$

More details on multiparticle dynamics with space charge can be found in [29, chap. 9].

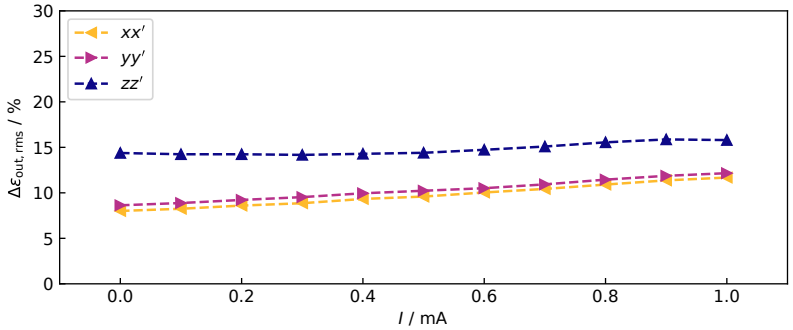

Figure 2.3: Simulated rms emittance growth $\Delta\varepsilon_{out,\,rms}$ of a preliminary HELIAC design for both transverse and the longitudinal plane in dependence of the beam current I; $A/z = 6$, $W_{out} = 7.3\,\mathrm{MeV/u}$.

2.2.2 *RF Defocusing in Drift Tube Linacs*

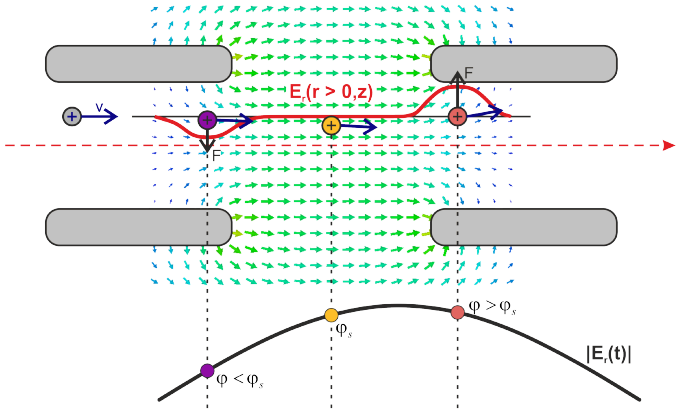

Figure 2.4: Schematic electric field distribution in an accelerating gap. The accelerating force F_z is caused by the longitudinal component E_z of the electric field on the beam axis (radius $r = 0$). The beam is moving in the direction z (to the right). [37, modified]

RF defocusing is the transverse defocusing experienced by a particle that crosses an accelerating gap on a longitudinally focusing RF phase [38]. When an off-axis particle enters an acceleration gap and is accelerated by a longitudinal electric RF field, it also experiences radial

φ_s	**longitudinal motion**	**transverse motion**	**average velocity**
−90°	focusing/bunching	defocusing	≈ constant
0°	light defocusing	≈ constant	largest gain
90°	defocusing/debunching	focusing	≈ constant

Table 2.1: Approximate effect of a particle bunchs' synchronous phase in a gap on the longitudinal and transverse motion as well as the average velocity of the bunch.

forces (see Figure 2.4). However, these oppositely directed radial electric forces in the two halves of the gap do not cause the entire radial force to be canceled out. In contrast, a net radial force is generated. This is due to the time-variation of the electric field amplitude as the particle traverses the gap. Considering a single cavity, then φ_s must be negative for longitudinal stability, i. e. the field increases when the synchronous particle is injected. However, this also means that most particles in the second half of the gap pass through an electric field that is higher than the field in the first half, resulting in a net defocusing force. Table 2.1 shows the corresponding relationships and effects.

2.2.3 *Magnetic Lenses*

To compensate for the RF defocusing of beams in drift-tube linacs, the use of magnetic lenses is the method of choice. Most common are solenoids or quadrupole magnets [39], which are mostly used in groups as quadrupole doublets or quadrupole triplets. The choice of which option is the most suitable depends on various factors such as beam energy, pulse frequency (resp. duty cycle of the beam) and the choice of overall technology (room temperature or superconducting).

2.2.3.1 *Quadrupoles*

Conventional quadrupole magnets consist of a yoke made of iron or cobalt-iron (CoFe) alloys and four pole shoes, arranged 90° apart around the beam axis where the opposing poles have the same polarity and an approximately hyperbolic surface. Excitation is provided by copper coils (sometimes water-cooled) wound around the pole shoes. Figure 2.5 depicts a schematic layout and the magnetic field distribution of a quadrupole magnet. It produces a magnetic field which is zero at the radial center of the beam line and increases linearly with distance from the center. Due to its configuration, a horizontally focused beam gets at the same time defocused in the vertical plane (and vice versa) by a single quadrupole. This is why quadrupole magnets are usually grouped to doublets or triplets with alternating

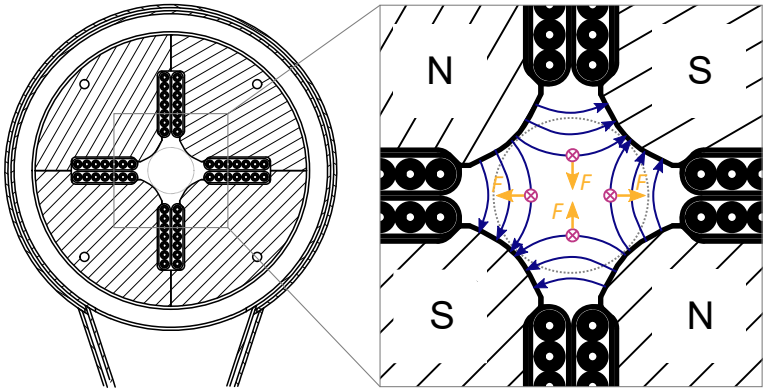

Figure 2.5: Schematic layout and magnetic field distribution of a quadrupole magnet. Shown is the Lorentz force F on 4 positively charged particles at different positions which move away from the reader into the paper plane. In this configuration (N = north pole, S = south pole), this quadrupole singlet focuses in the vertical plane and defocuses in the horizontal plane.

polarity which leads to a focusing in both transverse planes, called *alternating-gradient focusing* or *strong focusing*.

2.2.3.2 *Solenoids*

The magnetic field of solenoids is created by a rotationally symmetric coil. Unlike a single quadrupole magnet, solenoids have the advantage of focusing in both transverse planes simultaneously. From the Maxwell equation $\nabla \cdot B = 0$ it follows that the magnetic field, which is purely longitudinal in the inner part of the coil, must contain radial components at the input and output of the solenoid. While particles moving exactly in the center of the ideal beam axis do not experience any force, the others experience an azimuthal acceleration at the entrance and exit due to the radial component (see Figure 2.6). Due to the azimuthal movement, a radial force is generated along the longitudinal field. This force is proportional to the radial distance from the axis which ultimately leads to a focusing of the beam. The radially linear increasing focusing force leads to a convergence of the charged particles towards a common focal point. Furthermore, to minimize stray fields in adjacent superconducting RF cavities, so called bucking coils are frequently used.

2.3 LONGITUDINAL BEAM DYNAMICS

2.3.1 *Energy Gain in an Accelerating Gap*

An electrically charged particle passing the gap between two drift tubes with the velocity v experiences an electric field E_z (Figure 2.7):

$$E_z(r,z,t) = E_z(r,z)\cos(\omega t(z) + \phi), \tag{2.11}$$

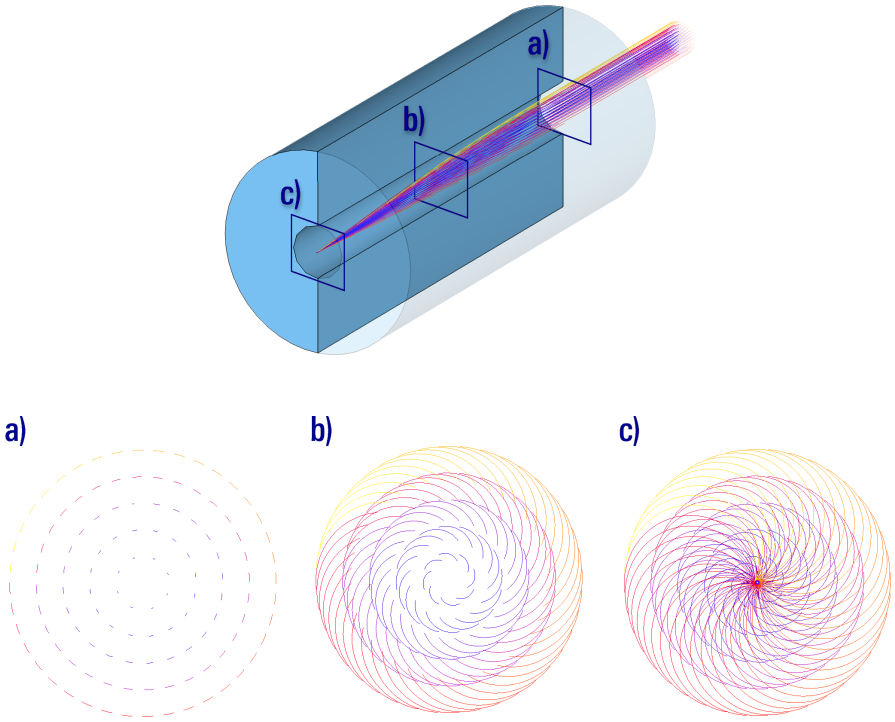

Figure 2.6: Solenoid focusing principle shown by a simulated (CST STUDIO SUITE) proton beam coming from the top right. *Bottom:* Three cross sectional views show the movement of 121 individually color-coded beam paths at the entrance into the solenoid (a), in its center (b) and at the exit (c).

with r being the radius from the beam axis z and the phase ϕ being the position of the particle relative to the RF cycle with the angular frequency ω when passing the center of the gap. The energy gain ΔW of a particle after passing the gap is generally given by

$\omega = 2\pi f$

$$\begin{aligned} \Delta W &= q \int_{\frac{-l_{\text{eff}}}{2}}^{\frac{-l_{\text{eff}}}{2}} E_z(r,z,t)\, dz \\ &= q \int_{\frac{-L_{\text{eff}}}{2}}^{\frac{-L_{\text{eff}}}{2}} E_z(r,z) \cos(\omega t(z) + \phi)\, dz, \end{aligned} \tag{2.12}$$

with the particle charge q and the effective gap length l_{eff} within which there is a significant axial E-field. The voltage amplitude U_0 on the beam axis ($r = 0$) between two adjacent drift tubes is given by:

$$U_0 = \int_{\frac{-l_{\text{eff}}}{2}}^{\frac{-l_{\text{eff}}}{2}} E_z(r=0,z)\, dz\,. \tag{2.13}$$

Due to the time-variable electric field and the finite speed of the particle, the effective electric voltage U_a is given by

$$U_a = \int_{\frac{-l_{\text{eff}}}{2}}^{\frac{-l_{\text{eff}}}{2}} E_z(r=0,z) \cos(\omega t(z))\, dz\,. \tag{2.14}$$

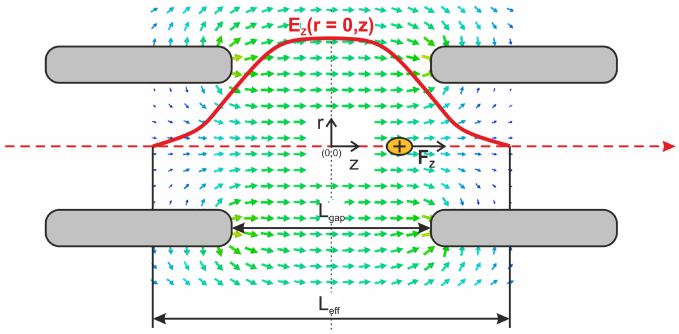

Figure 2.7: Schematic illustration of the E-field distribution in an accelerating gap [37, modified].

The *transit time factor* T then indicates this ratio:

$$T = \frac{U_a}{U_0} = \frac{\int_{\frac{-l_{\text{eff}}}{2}}^{\frac{-l_{\text{eff}}}{2}} E_z(r=0,z)\cos(\omega t(z))\,dz}{\int_{\frac{-l_{\text{eff}}}{2}}^{\frac{-l_{\text{eff}}}{2}} E_z(r=0,z)\,dz} \leqslant 1. \tag{2.15}$$

As the change in velocity in relation to the initial particle velocity while traversing a gap is generally small, we can approximate $\omega t(z) \approx \omega z/v = 2\pi z/\beta\lambda$ with $\beta = v/c$ and $\beta\lambda$ being the distance the particle travels in one RF-period. This leads to

$$T = \frac{\int_{\frac{-l_{\text{eff}}}{2}}^{\frac{-l_{\text{eff}}}{2}} E_z(0,z)\cos\left(\frac{2\pi z}{\beta\lambda}\right)dz}{\int_{\frac{-l_{\text{eff}}}{2}}^{\frac{-l_{\text{eff}}}{2}} E_z(0,z)\,dz} \leqslant 1 \tag{2.16}$$

and thus the energy gain of the particle can be derived:

$$\begin{aligned}\Delta W &= q \cdot U_0 \cdot T \cdot \cos(\phi)\\ &= q \cdot U_a \cdot \cos(\phi).\end{aligned} \tag{2.17}$$

It can be useful to express the energy gain ΔW in terms of another quantity: $E_0 T$. Here, E_0 is defined as the mean axial E-field amplitude $E_0 = U_0/l$ and l is the geometric cell length. The energy gain then becomes

$l = \beta\lambda/2$

$$\begin{aligned}\Delta W &= q \cdot E_0 \cdot T \cdot l \cdot \cos(\phi)\\ &= q \cdot E_a \cdot l \cdot \cos(\phi).\end{aligned} \tag{2.18}$$

The acceleration gradient E_a is an important quantity to classify the acceleration efficiency of a superconducting multi-gap cavity. From here on, it is therefore no longer used for just one gap, but as a parameter for the combined acceleration gradients of all gaps in a cavity. Thus, for an n-gap cavity l generally becomes with the so-called $\beta\lambda$-definition $l = n \cdot \beta\lambda/2$. This is a commonly used and good approximation of the cavity length L within which acceleration occurs.

2.3.2 *Longitudinal Phase Focusing*

The phase stability of particle bunches is crucial for a beam to be accelerated synchronously in an RF particle accelerator. The phase focusing of the particles around the synchronous particle, which by design remains synchronous to the RF fields, can be achieved by the bunch seeing an in time increasing accelerating field within the RF gaps. As a result, the slower particles ($\beta < \beta_s$) that arrive later than the synchronous particle see a stronger accelerating field and receive a larger velocity boost than the faster particles ($\beta > \beta_s$) that crossed the cavity earlier. The slower particles that are at the back of the bunch catch up with the faster particles at the front of the bunch and vice versa, as shown schematically in Figure 2.8. The term *synchronous particle* is not used fully consistently in the literature, as beam dynamics concepts such as KONUS or EQUUS are based precisely on the fact that the bunch in each gap passes through a somewhat different RF phase on average (i. e. is not "synchronous" to the RF). Thus, an efficient acceleration close to $\varphi = 0°$, can be combined with a less efficient, but beam-dynamically conventional and more stable acceleration close to values of e. g. $\varphi = -30°$. In these cases, one therefore often refers to a *reference particle* or *virtual synchronous particle* instead of a *synchronous particle*. Nevertheless, for simplicity, the term *synchronous particle* is used synonymously in this thesis. *Synchronous phase* φ_s refers to the RF phase position of the geometric center of mass of the bunch at the time a gap center is reached. As already mentioned above, this inherently changes from gap center to gap center in the EQUUS beam dynamics concept used and is explained in the following.

synchronous particle

φ_s

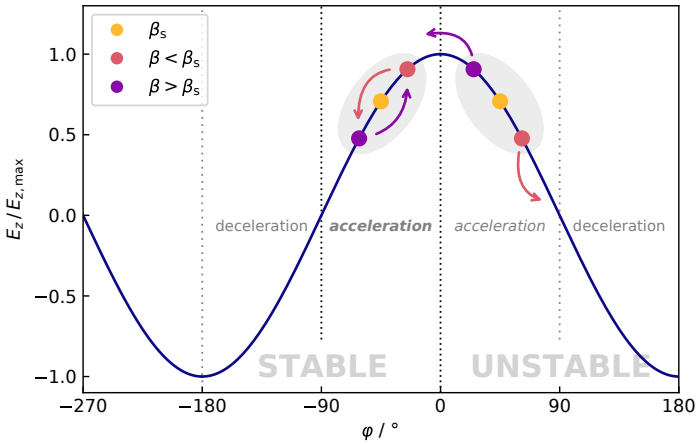

Figure 2.8: Longitudinal phase focusing keeps bunches stable in linacs if an increasing rf-field (here, the longitudinal *E*-field component located between adjacent drift tubes) is seen by the beam in the cavities.

2.4 EQUUS BEAM DYNAMICS CONCEPT

constant-phase

There are many different design concepts for developing the beam dynamics of linacs. Probably the most common is the **constant-phase** approach, in which a constant design phase of for example $\varphi_s = -30°$ is used at each gap within one multi-gap cavity (see Figure 2.9). This leads to gap center distances of $l = \frac{\beta\lambda}{2}$ with $\lambda = \frac{c}{f}$ being constant within one cavity and with the particle velocity $\beta = \frac{v}{c}$. The gap-to-gap distance thus increases successively with increasing particle velocity to ensure a constant synchronous phase.

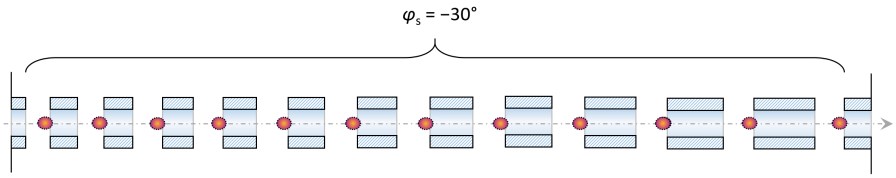

Figure 2.9: Schematic illustration of a constant-phase acceleration scheme showing a bunch in subsequent gaps, each at the time of the formation of the maximum electric field within the gap. The distance between the gap centers increases to ensure a constant synchronous phase φ_s while the bunch is accelerated.

However, depending on the application, other concepts can be advantageous. This includes the three concepts KONUS[4], APF[5] and EQUUS[6].

KONUS

KONUS is a beam dynamics concept for efficient acceleration with a minimum number of magnetic focusing elements. A KONUS section usually starts with a triplet lens and a short rebunching section around $\varphi_s = -35°$, followed by the main multigap acceleration starting near a synchronous phase of $\varphi_s = 0°$ with an excess energy compared to a hypothetical zero degree synchronous particle. Therefore, it moves towards more negative phases with each gap and the difference between the excess energy and the hypothetical reference energy for each gap decreases (see Figure 2.10). While KONUS and EQUUS have the similarity of the most negative phases at the start and end of the section, the gap center distance within a cavity changes for KONUS while it remains constant for EQUUS. Further details on KONUS and corresponding in-depth studies can be found in [37, 40, 41].

APF

APF [42–44] uses its DTL cavities not only for longitudinal but also for transverse focusing and therefore gives the possibility to be operated without magnetic lenses which could save costs and reduce the linac length. It has been developed since the 1950's but has only been used to a limited extent due to a decisive feature and disadvantage: As the transverse focusing is (only) depending on the

4 Acronym for ger. *Kombinierte Null Grad Struktur* (*Combined Zero Degree Structure*)
5 Acronym for *Alternating Phase Focusing*
6 Acronym for *Equidistant Multi-Gap Structure*

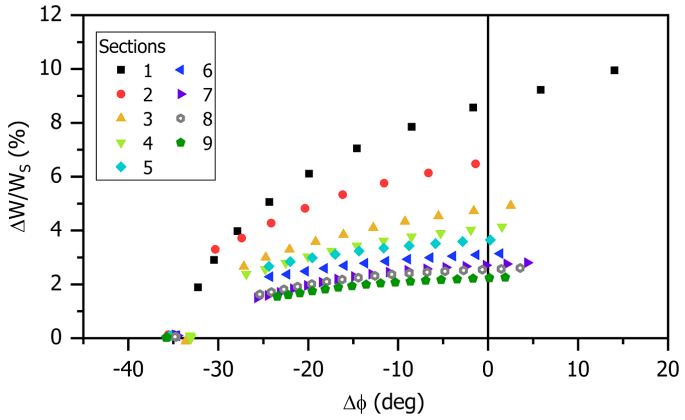

Figure 2.10: Exemplary bunch center motion of a KONUS design. [40]

phase position of the particles (in contrast to the use of magnetic lenses for transverse focusing) there is a strong coupling between transverse and longitudinal motion. This inevitably leads to emittance growth (especially at low energies where the bunch usually has a larger phase width) and to a significantly reduced energy acceptance at the entrance of the respective cavity.

EQUUS

The **EQUUS** concept was first named and studied in detail in 2009 by Minaev et al. [28]. Prior to that, there were first approaches with multi-gap constant-β DTLs already in 1994 by R. von Hahn *et al.* [45] and in 1998 by H. Podlech *et al.* [46, 47]. Even earlier in history, the Argonne Tandem Linac Accelerator System (ATLAS) at Argonne National Laboratory (ANL) in the USA can be considered as the origin of a cw-capable superconducting heavy ion linac [48–50]. Superconducting split-ring resonators (3 gaps, constant-β design) were used here. EQUUS features an efficient acceleration with some similarity to KONUS and special advantage for variable final energies. In contrast to KONUS, at EQUUS the beam is usually injected with an energy *deficiency*[7] at a synchronous phase of $\varphi_s \ll 0°$ into the cavity.

The basic principle of the design can be described as follows:

A. The beam is injected into the cavity with an energy deficiency of $-5\,\%$ to $-20\,\%$ to the reference energy of the cavity, defined by its geometrical parameters, namely the $\beta\lambda/2$ distance of neighboring gap centers. The value that is reasonably taken for the design depends, among other things, on the achievable gap voltage, the length of the cavity, the selected input synchronous phase (in the first gap) and the particle distribution. At the same time, the synchronous phase in the first gap is chosen within the range of about $-55°$ to $-25°$ ensuring longitudinal stability through the focusing effect in this phase region.

7 *energy deficiency* in relation to the cavity's design energy (also *reference energy*) defined by the gap center to gap center distance $\beta\lambda/2$. When $\beta\lambda/2$ is kept constant within a cavity, it is also called *constant-β cavity*.

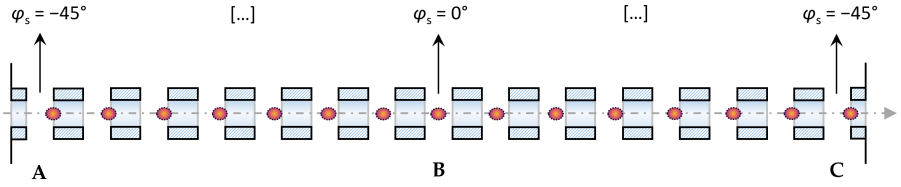

Figure 2.11: Schematic illustration of an EQUUS acceleration scheme with a bunch in subsequent gaps, each at the time of the formation of the maximum electric field within the gap. While the bunch crosses the center of the gap with $\varphi_s \ll 0°$ for both the first (**A**) and the last gap (**C**) at the time of a rising *E*-field and therefore is depicted at the end of the gaps, the bunch is located within the middle of the cavity (**B**) in the center of the gap ($\varphi_s = 0°$).

B. Based on the previously selected parameters, the accelerated bunch now performs a sliding movement in the longitudinal phase space (Figure 2.12), as in KONUS partly, but starting in the third quadrant (see Figure 2.13) moving towards a positive synchronous phase direction near the coordinate system's origin. The acceleration efficiency increases with each gap, while the bunch is still slower than the reference particle. Finally, the synchronous phase approaches $\varphi_s \approx 0°$ and the cavity's reference energy at the same time. The cavity could now end at this point and the beam could be extracted.

C. It is also possible to accelerate the beam further in a cavity with enough gaps. In this case, the beam would become faster than the reference energy and with each gap slide back to more negative synchronous phases as it arrives earlier than the reference particle in each gap. This slightly lowers the acceleration efficiency again but ensures longitudinal stability one more time.

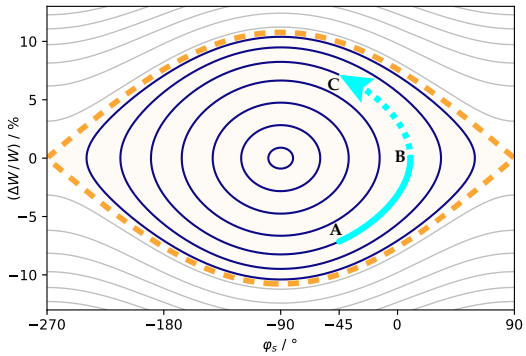

Figure 2.12: Schematic illustration of the typical movement of an accelerated bunch in an EQUUS-section in the longitudinal phase space. The stable region is within the dashed orange so-called Separatrix.

To increase the flexibility with this beam dynamics approach, the EQUUS movement can be split up on two separate cavities at the point

where the reference energy of the cavity is reached, and the bunch continues to accelerate to higher energies and again to synchronous phases of $\varphi_s \ll 0°$. While CH0 of HELIAC has been designed for a full EQUUS-movement, the split-up is used for all subsequent CH cavities. Furthermore, the main structure design parameters for EQUUS are given in Figure 2.13.

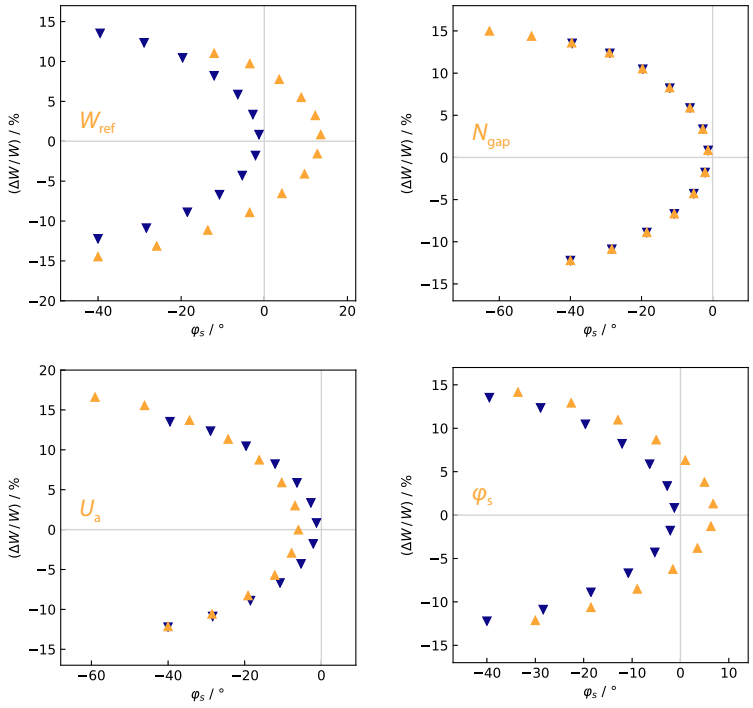

Figure 2.13: Exemplary variation of the four main equidistant structure design parameters reference energy W_{ref}, number of gaps N_{gap}, effective cavity voltage U_a and synchronous phase φ_s of the first gap.

2.5 SIMULATION CODES

To efficiently calculate the trajectory of charged particles, most computer programs use either analytical charge distributions or so-called particle-in-cell methods (PIC) [51] based on Fast Fourier Transformation (FFT) [52]. While analytical distribution models can be useful for theoretical investigations, they do not allow detailed simulations for real accelerator facilities. In principle, space-charge effects could be determined by calculating the Coulomb forces between all particles. However, given particle numbers in the range of 10^9, this approach is inefficient. PIC therefore uses a temporal and spatial discretization of an often-reduced number of particles, so-called *macroparticles*, in which several particles are combined into a common particle and

location. After subdividing the Cartesian space in and around the particle ensemble, the Poisson equation for electrostatics

$$\Delta\phi = -\frac{\rho}{\epsilon_0} \tag{2.19}$$

with $\Delta\phi$ being the Laplacian of the electric potential, ρ the total volume charge density and ϵ_0 the vacuum permittivity, is solved for each grid point. Then, the resulting forces are interpolated from the grid points to the macroparticles.

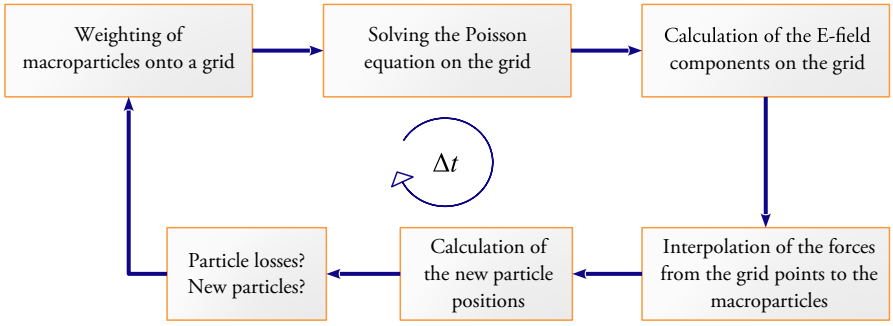

Figure 2.14: Simplified schematic illustration of a PIC algorithm with time step Δt.

With PIC, realistic space-charge distributions can thus be assumed, whereby discretization errors play a decisive role here. While the forces between charged particles act continuously, in the simulations they are only considered as single pulses interrupted by particle transport (Figure 2.14). If these time steps are too large, the simulation accuracy is reduced [53]. However, the other way around, if the spatial discretization is too fine, the number of particles per grid cell decreases, which can lead to numerical noise and artificial emittance growth [54]. When performing beam dynamics simulations, it is therefore essential to consider their accuracy as a function of various parameters such as beam current, particle number and spatial/temporal discretization of internal and external fields.

2.5.1 *LORASR*

The beam dynamics design for HELIAC was performed with LORASR[8], a simulation program especially for drift-tube accelerators which use the KONUS beam dynamics. Details on the general functionality of LORASR can be found in [55], on the PIC-FFT algorithm in [56] and with focus on KONUS in [40]. Among the accelerator facilities where LORASR has been used so far are:

8 Acronym for ger. *Longitudinale und radiale Strahltransportrechnungen unter Berücksichtigung der Raumladung* (longitudinal and radial beam transport calculations including space charge).

- GSI high-current injector (HSI) [57], high charge injector (HLI) [58], ion trap facility HITRAP [59] and FAIR proton injector [60],
- CERN Linac3 [26] and REX-ISOLDE (Geneva, Switzerland) [61],
- Fission fragment accelerator (MAFF) at the Munich II research reactor [62],
- Heidelberg Ion Beam Therapy Center (HIT) [63],
- Ion Beam Therapy Center MedAustron (Wiener Neustadt, Austria) [64],
- CNAO (Pavia, Italy) [40],
- MIT (Marburg, Germany) [40],
- SPHIC (Shanghai, China) [40],
- EBIS pre-injector at BNL (Upton, USA) [65],
- TRIUMF ISAC-I (Vancouver, Canada) [41],
- FRANZ at Goethe University (Frankfurt, Germany) [66–68],
- Injector for CSRm at HIRFL (Lanzhou, China) [69],
- HILac and LILac injectors for NICA at JINR (Dubna, Russia) [70, 71],
- MYRRHA injector (Mol, Belgium) [72, 73].

Probably the most important characteristic of a simulation is whether it is *realistic*, in the sense that the results determined by it, or in this case the particle beam dynamics, are actually true in reality or at least are reasonably accurate approximations. The successful construction and long-term operation of the accelerator facilities mentioned above can be regarded as a very strong indication of this. Therefore, LORASR has been chosen as primary simulation code for design and optimization of the beam dynamics layout in this thesis.

To model the acceleration gaps inside a cavity, LORASR proceeds as follows [56]: After defining the array and geometry of the acceleration gaps (based on the input parameters of the designer) each gap field is approximated by an axially symmetric E-field ($E_\phi = \text{const.}$). In radial direction, 4 zones with linearized longitudinal fields $E_z(z, r)$ are defined (zone borders are at 20 %, 31.5 % and 40 % of the inner drift tube diameter $\varnothing_i$) divided into 5 individual zones along the beam axis for each gap, resulting in a total of 20 rings (Figure 2.15). Each particle is then tracked along each gap in a 30-step process.

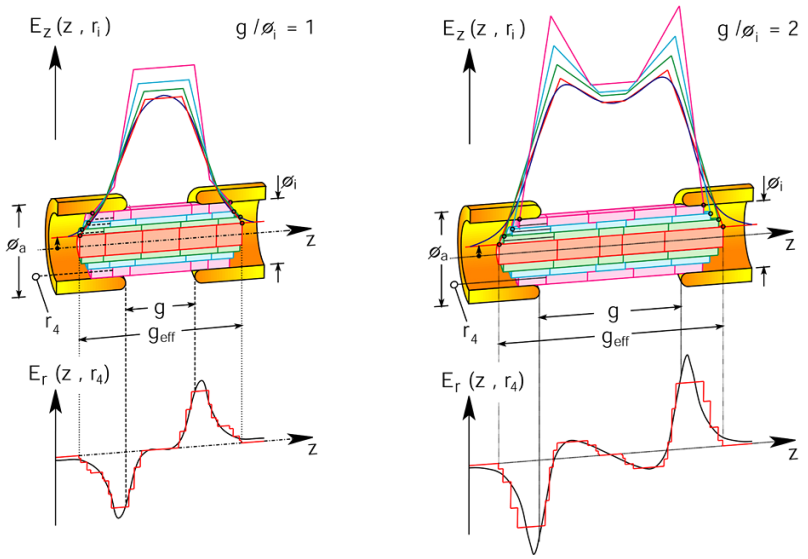

Figure 2.15: Schematic illustration of the longitudinal and radial *E*-field approximations used in LORASR for different gap geometries. [55]

2.5.2 *TraceWin*

Simulations for HELIAC have also been performed with TraceWin [74]. It is a widely used and feature-rich beam dynamics code allowing start-to-end simulations from ion source to target. For large accelerator projects like ESS, MYRRHA, IFMIF, LINAC4, SPIRAL2, EUROTRANS, EUROISOL and SPL it has been chosen as reference code. Furthermore, a benchmark with the codes LORASR, DYNAMION and PARMILA at the UNILAC (GSI) has shown good agreement between the results. Also C. Zhang *et al.* [75] and H. Hähnel [76] found only minimal discrepancies between results from TraceWin and LORASR.

A crucial parameter for the accuracy of beam trajectories simulated with TraceWin is the way gaps in cavities are modeled in the simulation. In principle, three variants can be distinguished here:

A. **Thin Gap:** In the *Thin Gap* approximation, the forces on the particles of a bunch are only computed once – while the bunch center traverses the center of a gap. Thus, it is approximated to a literally infinitesimal thin gap. The great advantage of this variant is the high simulation speed it allows. Especially for error studies, which usually require a large number of simulations (order of magnitude 10^3), this advantage comes in handy. However, the highly simplifying approximation of the gap geometry is at the same time the disadvantage of this method. Longitudinally, often the largest emittance growth occurs compared to the other two methods, which approximate the longitudinal gap geometry more realistically. Especially for complex beam dynamics concepts like KONUS and EQUUS, this approximation therefore leads to errors that should be taken into account. Fine tuning of

parameters such as the RF phase of cavities can help to account for the simplified gap geometry. For HELIAC, this approximation already showed sufficiently accurate agreement to LORASR for the relevant beam parameters.

B. **2D (LORASR) Field Map:** TraceWin gives the possibility to import electric and magnetic field maps of external programs, so 2D field maps of $E_z(z)$, generated by LORASR and sufficiently converted to the required data structure format by TraceWin could be used. Thus, the main disadvantage of the Thin Gap method can be eliminated, since the longitudinal field profile is now reproduced much more accurately. At the same time, the variable and by default smaller step size of the approximated radial field in TraceWin can be utilized. The transverse E-field components are not exported from LORASR and imported into TraceWin in this method but are approximated by TraceWin so that the transverse RF defocusing of the beam in acceleration gaps is also taken into account. This ultimately leads to an already quite detailed reproduction of the accelerator respectively the cavity in TraceWin.

C. **3D (CST) Field Map:** For a very realistic reproduction of the fields inside a cavity, a full 3D field map of the electric (and possibly magnetic) fields can be used, usually especially in the final phase of the design process. This can usually be exported from the electromagnetic 3D simulation program (e. g. CST Microwave Studio) and used accordingly, after a format conversion, in TraceWin. The corresponding file format is defined in [77] and shown in Listing 2.1. While the resulting simulation results can be considered the most accurate among the three methods, the simulation time required is also the largest. Moreover, the effort required for this method is by far the largest, since the 3D model of the cavity must be created (or even fully finalized for manufacturing) beforehand. This usually requires very extensive R&D activities (see e. g. [31] and [32]).

When directly comparing LORASR simulations to TraceWin Thin Gap simulations, the following has been observed: Even though the energy gain per gap is identical in both codes, it was found that the shear transformation of the bunch in the longitudinal phase space in TraceWin sometimes is too weak (compared to the LORASR calculation). The difference is that in TraceWin the full shear occurs at one point (in the center of the gap) and the bunch drifts until there with the low initial energy of the previous gap. In LORASR, on the other hand, the shear happens gradually in a 30-step process (with simultaneous gradual energy gain) over the entire effective length of the gap. This difference obviously affects mainly the edge particles of a bunch (in particular the *late* particles). It can be handled in TraceWin

the shear transformation of the bunch is often referred to as "rotation", but which, however, is geometrically not fully correct

Listing 2.1: Data format of 3D E field maps for TraceWin. [77]

```
nz zmax
nx xmin xmax
ny ymin ymax
Norm
for k=0 to nz
  for j=0 to ny
    for i=0 to nx
      Fz(k*zmax/nz, ymin+j*(ymax-ymin)/ny, xmin+i*(xmax-xmin)/nx)
      Return
```

by slightly changing the RF phase of the cavity and/or adjusting the E-field amplitude of the cavity in a small percentage range. The TraceWin simulations for HELIAC are shown in Section 4.4.1.1 (p. 56).

To sum up, all three variants of gap modeling in TraceWin have their advantages and disadvantages. In summary, the big benefit of TraceWin is the possibility to perform start-to-end simulations with feature-rich analysis methods. In this way, the entire beam dynamics behavior of an accelerator can be modeled and investigated in detail, from the ion source through all acceleration, diagnostic and transport sections to the target of the experimentalists. Therefore, after LORASR has proven its value as design code for the cavities, TraceWin is recommended in the long term for the simulation of the beam dynamics of the entire HELIAC with consideration of the limitations mentioned above.

3

SUPER-HEAVY ELEMENT RESEARCH

3.1 INTRODUCTION

While uranium is the heaviest element found in significant quantities in nature [78], the production and exploration of even heavier elements is expected to provide answers to many scientific questions [1]:

Neptunium and plutonium are heavier than uranium but have only been discovered in traces in nature [79–81].

- Where do nuclei and elements come from? Can superheavy nuclei be produced in the cosmos?
- How are superheavy nuclei and atoms made and organized? Do very long-lived superheavy nuclei exist in nature?
- What are the heaviest nuclei that can exist? Where does the periodic table of elements end?
- How can superheavy nuclei and atoms be exploited to reveal the fundamental symmetries of nature? What is the interplay between strong and electromagnetic interactions as the product of the fine-structure constant and atomic number approaches 1 ($\alpha Z \rightarrow 1$)?
- What are the chemical and physical properties of superheavy atoms?

Many properties of atomic nuclei can be explained in a macroscopic approach by the liquid drop model of the atomic nucleus. It is based on a strong attractive force between the nucleons (see Figure 3.1) and the repulsive electric force acting on the protons. According to this model, elements with atomic numbers (proton numbers) greater than $Z \approx 100$ shouldn't exist [84], because from here on the electrical repulsion outweighs the attraction of the nuclear force [85].

The liquid drop model was developed at the beginning of the 1930s by George Gamow [82], Hans Bethe and Carl Friedrich von Weizsäcker [83]

The liquid drop model cannot explain the phenomenon of the so-called magic numbers. Through precise mass measurements it was known that with the proton and neutron numbers 2, 8, 20, 28, 50 and 82 (for the neutrons also 126) the nuclei are particularly stable bonded relative to the average trend. This is due to an increased binding energy of the nuclei (see Figure 3.2). Most stable is this binding with the double magic nuclei, like ^{208}Pb with 82 protons and 126 neutrons. An explanation was only possible at the end of the 1940's with the shell model for the atomic nucleus by several scientists, most notably Maria Goeppert-Mayer [88, 89] and J. Hans D. Jensen [90]. From the 1950s, this model was used to calculate the next magic numbers resp. new "magic shell closure" beyond ^{208}Pb, and the concept of superheavy elements was introduced for such nuclei.

Mayer and Jensen were awarded the 1963 Nobel Prize in Physics for their discoveries concerning nuclear shell structure.

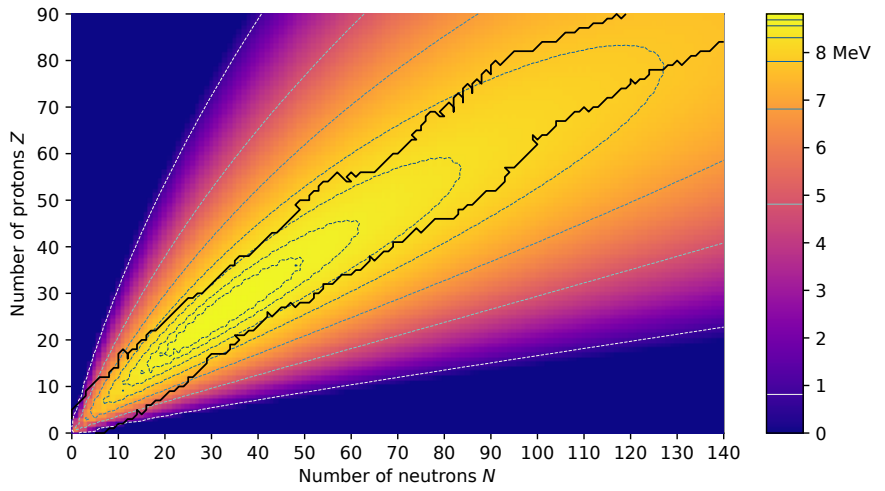

Figure 3.1: Mean binding energy per nucleon calculated with the Weizsäcker semi-empirical mass formula (SEMF) [83]. Colored dashed contour lines double in energy difference as moving away from the maximum calculated binding energy, showing the rapid instability outside of experimentally-known nuclides (inside the solid black lines). The a coefficients for the SEMF are taken from [86] and factor in data by [87].

3.2 FUSION OF SUPERHEAVY ELEMENTS

The term "superheavy" is not uniformly defined in literature. Usually it refers to transactinide chemical elements with values between $Z \geqslant 103$ [3] and $Z \geqslant 114$ [91]. All currently known superheavy nuclei are radioactive and were produced by scientists in nuclear reactions.

The most successful methods for the laboratory synthesis of heavy elements have been fusion-evaporation reactions using heavy-element targets, recoil-separation techniques, and the identification of the nuclei by generic ties to known daughter decays after implantation into position-sensitive detectors [92].

Two different experimental approaches, cold fusion [93] and hot fusion [94], were commonly used to extend the periodic table from $Z = 107$ and above. The basic principle is the same for both methods: One type of nuclei is accelerated to energies high enough to approach a target nuclei sufficiently close to overcome the repulsive Coulomb barrier[1] and enter the region of the attracting strong force. The two interacting nuclei form a composite system and evolve into a compound nucleus (CN). Now, the CN can separate and decay back again into the initial nuclei. Alternatively, it could go directly to fission channels without forming a spherical CN, which is called quasi-fission. However,

1 The Coulomb barrier between two nuclei is given as the electrostatic potential energy $U_{\text{Coulomb}} = \frac{e^2}{4\pi\epsilon_0}\frac{Z_1 Z_2}{R_1+R_2}$ (with the elementary charge e) for the atomic numbers Z and the nuclear radii R. In this context, the probability of quantum mechanical tunneling (Gamov factor) to overcome the Coulomb barrier should also be considered. [95]

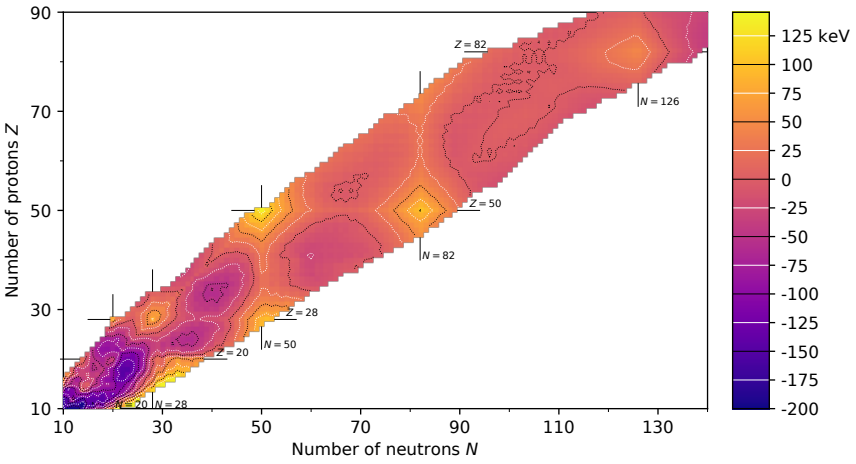

Figure 3.2: The discrepancy between experimentally-obtained binding energies by the AME2016 atomic mass evaluation [87] and those predicted by the SEMF (using the a coefficients from [86]). An increased binding energy of magic and double-magic nuclei is visible. Energy colors are trimmed to the range [−120 keV, 150 keV] for contrast reasons.

it may also happen that the CN cools down due to the evaporation of neutrons and γ rays and forms an evaporation residue (ER) in the ground state. In this case, the neutron-emission reduces the excitation energy of the CN below the fission barrier. This process can be made more likely by using projectile and/or target nuclei, which have a (double) magic number like ^{48}Ca with 20 protons and 28 neutrons or ^{208}Pb with 82 protons and 126 neutrons. By using one of these two elements, the resulting compound nuclei in fusion reactions have slightly lower excitation energies than in reactions with neighboring nuclei, resulting in a lower probability of the compound nucleus fission. The result is the synthesis of a super-heavy element, e. g. darmstadtium-110 by using Pb-208 as target and Ni-62 as projectile:

$$^{62}_{28}\mathrm{Ni} + ^{208}_{82}\mathrm{Pb} \rightarrow ^{269}_{110}\mathrm{Ds} + ^{1}_{0}\mathrm{n}.$$

cold fusion

In this so called "cold fusion" the excitation energy is relatively low and only one neutron (and γ rays) is emitted to reach the ground state of the ER. In contrast, the synthesis of super-heavy elements in "hot fusion" reactions with actinide targets and lighter projectiles the excitation energy is higher, and three to five neutrons are emitted [96]. An exemplary reaction for the hot fusion is the synthesis of the so-far heaviest known element: Oganesson-118. It was synthesized 2006 in Dubna (Russia) with californium-249 as target and calcium-48 as projectile [4]:

hot fusion

$$^{48}_{20}\mathrm{Ca} + ^{249}_{98}\mathrm{Cf} \rightarrow ^{294}_{118}\mathrm{Og} + 3^{1}_{0}\mathrm{n}.$$

Figure 3.3 shows the rapid decrease of the cross section for fusion reactions towards higher proton numbers, in particular for the cold fusion approach.

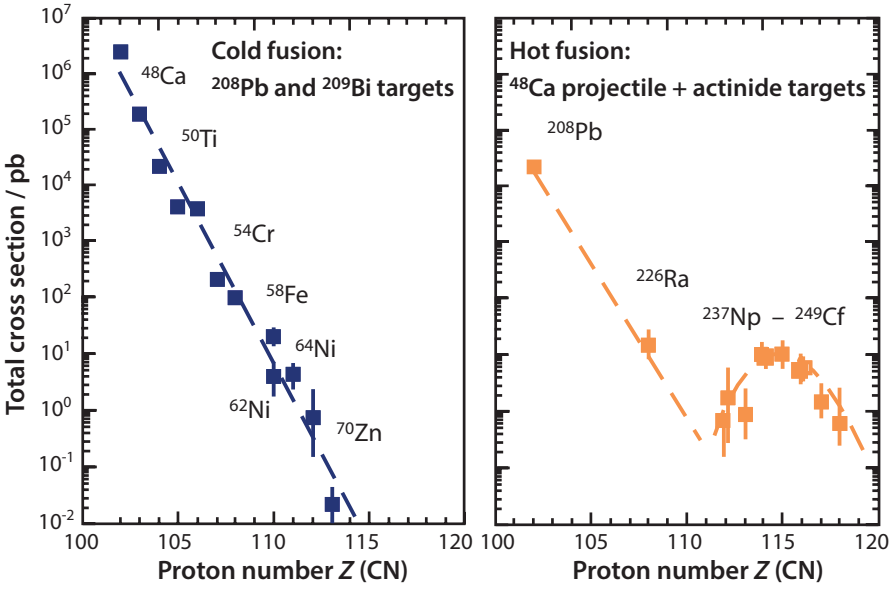

Figure 3.3: Measured cross sections for cold and hot fusion reactions depending on the proton number of the compound nucleus (CN). The plotted total cross section is the maximum value of the sum of neutron evaporation channels measured as a function of the beam energy. Data taken from [6]. The dashed curves are drawn to guide the eye.

$Z > 118$ For elements with $Z > 118$ several approaches for the synthesis are potentially possible: While calcium-48 already mentioned above is basically well suited as projectile, einsteinium ($Z = 99$) and fermium ($Z = 100$) are difficult to obtain in sufficiently large quantities for the target production. Therefore, the use of heavier projectiles for synthesis is necessary.

$Z = 119$ For the production of element 119, the approach ${}^{50}_{22}\mathrm{Ti} + {}^{249}_{97}\mathrm{Bk}$ seems to be appropriate. Among others, scientists at GSI (Darmstadt, Germany) used this reaction in 2012, but without detecting any event that could be assigned to the decay of an isotope of element 119 [6].

$Z = 120$ For element 120, there are also multiple reactions plausible:

$$^{50}\mathrm{Ti} + {}^{249}\mathrm{Cf},\ {}^{54}\mathrm{Cr} + {}^{248}\mathrm{Cm},\ {}^{58}\mathrm{Fe} + {}^{244}\mathrm{Pu} \text{ and } {}^{64}\mathrm{Ni} + {}^{238}\mathrm{U}.$$

The last three reactions all yield the same compound nucleus ${}^{302}120^*$, the first one the slightly lighter isotope ${}^{299}120^*$.

Which reaction is targeted depends on technical and physical considerations. According to S. Hofmann [85], there is the assumption that reactions with great charge asymmetry between projectile and target are more advantageous. This indicates the reaction ${}^{50}\mathrm{Ti} + {}^{249}\mathrm{Cf}$ for the synthesis of element 120, but on the other hand there are

measurements showing that neutron-rich reactions are more favorable. This, in turn, speaks in favor of the other three reactions, in which the compound nucleus $^{302}120^{*}$ has three more neutrons and is thus also closer to the predicted neutron shell $N = 184$. Nevertheless, most publications predict much lower cross sections for complete-fusion reactions with projectiles heavier than calcium-48 [97–103].

future of SHE research

To sum it up, two main measures are therefore essential for the future synthesis of superheavy elements in the region of $Z \geqslant 119$ at decreasing cross sections [104]:

1. An improvement of the experimental sensitivity. [6]
2. The further development of accelerator facilities for higher beam intensities. [92, 105, 106]

In the context of this thesis, the second measure was tackled and the beam dynamics layout for a new accelerator for the production of superheavy elements has been designed.

3.3 CHOICE OF TECHNOLOGY – SUPERCONDUCTING VERSUS NORMAL CONDUCTING CAVITIES

An important issue in the field of high-performance hadron linacs is the choice of technology in terms of superconductivity or room temperature operation (see Figure 3.4) [107]. The decision for a particular technology usually depends on several parameters which include the following in the first place:

- Beam energy W,
- beam current I,
- beam power P_{beam} and
- duty cycle D.

At the same time, the decision for one of the technologies also has many consequences for the design of the accelerator. The front end of a particle accelerator usually consists of an ion source, a low-energy beam transport line (LEBT) and a radio frequency quadrupole (RFQ). Due to the particle losses that generally occur in these elements and the danger of thermal quenching, they are usually realized with normal conducting (NC) technology. For the subsequent elements, a superconducting (SC) design can then also be considered. In addition to the previously mentioned decision criteria beam energy W, beam current I, beam power P and duty cycle D further decision factors are capital costs, operating costs (particularly in terms of electrical power), technical risk, reliability and availability.

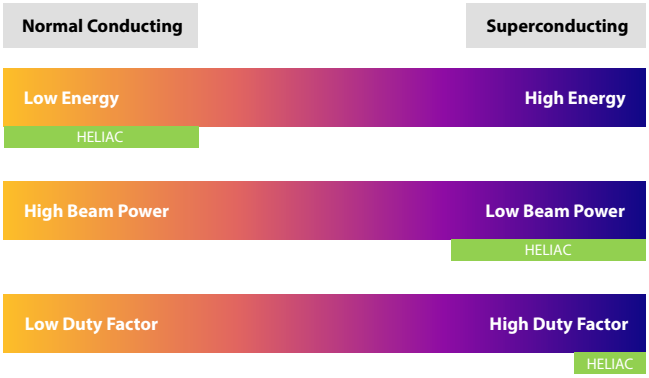

Figure 3.4: Qualitative regimes of normal conducting and superconducting cavities and the approximate classification of HELIAC. [107, modified]

The challenges of sc cavities so far (e. g. multipacting, perturbing mechanical modes/microphonics, Lorentz-force detuning, field emission) have been intensively studied and are well understood and addressed in the meantime. Based on worldwide experience with high-performance elliptical cavities, the design, handling, and surface treatment of low- and medium-β cavities has also evolved. Further performance enhancement could be achieved by nitrogen doping and Nb_3Sn coating, which have not yet been applied on a larger scale to low-β cavities. Also further exploring different surface treatments and the design and integration of cryomodules could bring new insights.

Transition energy between nc and sc part

In the coming decades, the construction of more linacs with high beam power for a wide range of particles from protons to heavy ions can be expected. Here, thanks to sc cavities for low- and medium-β ranges, the superconducting accelerator part is already increasingly starting to operate at beam energies in the order of 1 MeV/u (HELIAC: 1.39 MeV/u). Certainly, there are disadvantages when pushing down the energy transition between the nc and sc part: The beam dynamics matching is more difficult; the entire system gets more complex with a larger cryogenic plant; advanced R&D on low beta cavities/magnets especially for high average current is needed; NC cavities are easier to handle in terms of conditioning permanence as well as easy set-up and the operational flexibility is paid by a more time-consuming set-up of the entire linac. Nevertheless, the advantages often outweigh the disadvantages: The linac length is reduced due to the higher acceleration gradient; the aperture-to-beam radius could be increased; the power efficiency P_{beam}/P_{total} is larger; capital costs (short linac length) and operational costs (in terms of electricity) are reduced and sc cavities work well with high duty cycle.

As sc cavities are becoming established as the most suitable solution for low- and medium-β linac sections for CW applications, in recent years a large number of laboratories around the world have been

working in this field. As a result, the design of these resonators is becoming increasingly mature. By now, the parameters to be optimized as well as production techniques and tools are well established. In particular, QWRs, HWRs and SSRs[2] (much more rarely also double- and triple-spoke cavities) have since been widely used worldwide (Figure 3.5).

QWR, HWR, SSR

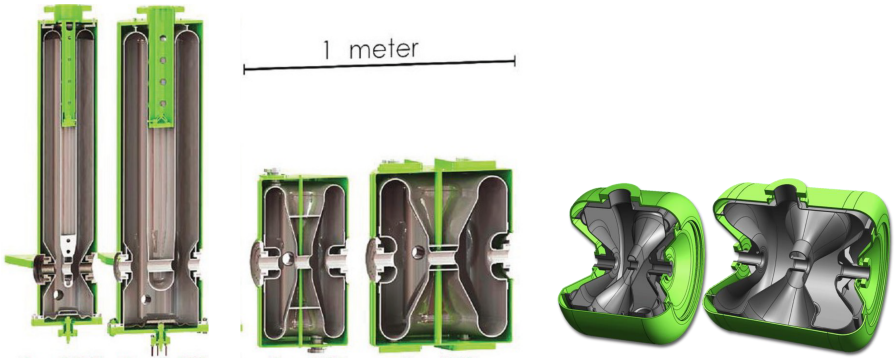

Figure 3.5: Three pairs of the most widely used superconducting cavity types in the low- and medium-β regime. *Left:* 80.5 MHz QWRs ($\beta = 0.041$ and 0.085). *Center:* 322 MHz HWRs ($\beta = 0.29$ and 0.53) [108]. *Right:* 325 MHz SSRs ($\beta = 0.22$ and 0.51) [109].

On the other hand, the approach of superconducting accelerator structures in the very-low-β range seems to be discarded in favor of modern normal-conducting CW RFQs. Table 3.1 (p. 33) provides a worldwide overview of existing and planned major superconducting ion accelerators. While the widely used QWRs, HWRs and SSRs are resonator types which offer several major advantages (they are extensively researched in many accelerator laboratories, can be manufactured relatively easily and have a high energy acceptance and flexible usage options), their efficiency in terms of energy gain per distance is a clear disadvantage compared to superconducting CH-DTL cavities, which can definitely score points here. Therefore, superconducting CH-DTLs are used as the main accelerator structures in the beam dynamics design for HELIAC (see Figure 3.6).

CH-DTL

Complex cavities such as superconducting multi-gap CH-DTL cavities are still a rarity but have the possibility to develop into a viable and reliable option due to their extremely high acceleration efficiency, already presented by previous research achievements [8] and making use of in this work. Highly comprehensive research on the mechanical design of the already built cavities CH0–CH2 can be found in [31, 32]. Based on these successful designs and tests, the design process of the additional nine CH cavities was performed in parallel with the beam dynamics investigations of this work and continues to be optimized [33]. Here, the design optimizations are targeting further improvement of the mechanical properties (both of the cylindrically symmetric

2 single-spoke resonators

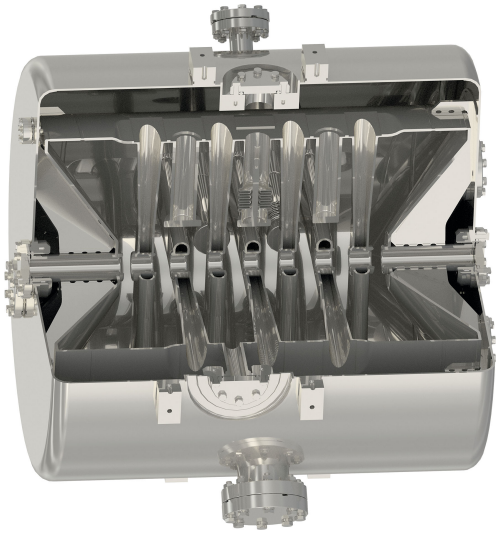

Figure 3.6: Three-quarter section rendering of the final geometry of the 216.816 MHz sc CH1/2 for HELIAC with surrounding helium shell ($\beta = 0.069$). [32]

Further research on CH-DTLs

cavity resonator and of the bellow tuners used for frequency tuning), reduction of E and B peak fields within the cavity, and reduction of production costs (e. g. by using identical parts within the nine cavities and by reducing the number of welds). The design of cavities CH3 to CH11 has been largely completed by now. For this purpose, a wide variety of simulations were performed to gain information for the future construction and operation of the cavities. These include the force acting on the bellow tuner when mechanically deformed to change the resonance frequency, the effect on the resonance frequency due to thermal shrinkage, due to evacuation of the cavity and due to pressure fluctuations within the cryomodule, the surface treatment due to Buffered Chemical Polishing (BCP), the possibility of secondary electron emission and multipacting occurring, and possible measures to handle these effects. In a next step CH3–CH5 will be built. During manufacturing, control measurements are performed, followed by a cold test to measure essential RF parameters. Furthermore, additional bellow tuners are currently being manufactured as part of the research. The purpose of this is to perform a long-term stress test on the niobium in order to determine the maximum stress on complex geometric structures such as the bellow tuners and thus ensure long and safe operation. In addition to the lifetime of the tuners and the maximum possible excursion force, the aim is also to determine possible hysteresis effects and material fatigue caused by operation. For this purpose, a tuner test bench was developed in order to test the tuners under cold conditions (liquid nitrogen).

Facility / Accel. Project	sc Cavity Type	f / MHz	max. A/z	Cavity β	$E_{\text{out, max, max. } A/z}$ (MeV/u)	I
ANL ATLAS[48, 49, 50, 110, 111]	QWR, SRR	48.5–109.25	7	0.025–0.15	12	$< 10\,\text{p}\mu\text{A}$
MSU ReA3[112]	QWR	80.5	5	0.041–0.085	12	$\sim \mu\text{A}$
MSU FRIB[112]	QWR, HWR, Ell.	80.5–644	7	0.041–0.53	400	$< 2\,\text{mA}$
INFN LNL[113, 114]	RFQ, QWR	80–160	7	0.047–0.13	10	$\ll \mu\text{A}$
RISP RAON[115]	QWR, HWR, SSR	81.25–325	3 (7)	0.047–0.51	18.5 (200)	$8.3\,\text{p}\mu\text{A}$
IUAC, New Delhi[116, 117]	QWR	97	3.4	0.05–0.08	7.2	50 pnA
TRIUMF ISAAC-II[118]	QWR	106–141	6	0.057–0.11	6.5	$\ll \mu\text{A}$
HELIAC	**CH, SSR**	216.816	6	0.059–0.121	7.3	1 mA
CERN HIE-ISOLDE[119, 120]	QWR	101.28	3 (4.5)	0.063–0.103	8 (10)	$\ll \mu\text{A}$
GANIL SPIRAL2[121, 122]	QWR	88.0525	3	0.07–0.12	15	1 mA
RIKEN RILAC[123]	QWR	73	6.8	0.078	11	$< 100\,\mu\text{A}$
SARAF[124]	HWR	176	2	0.091–0.181	20	5 mA

Table 3.1: Overview of existing and planned superconducting ion accelerators, listed by the lowest cavities' geometric β with the cavities frequencies f, maximum mass-to-charge ratio A/z, the maximum beam energy E_{out} and maximum/design/typical beam current I[3]. Different laboratories indicate their beam currents in different units. While some use the electrical beam current I (in e. g. nA, µA, mA), others use the particle current I_{part}. Some of the accelerators ($I \ll \mu A$) are post-accelerators for radioactive isotopes, which can only be produced with very low intensities. In principle, these can therefore also be regarded as "zero current machines". Ell. = Elliptical cavity, SRR = Split-ring resonator.

3 For ions of charge state Q this is composed as follows: $I = QI_{\text{part}}$. Thus, for highly stripped ions the electrical current can be much greater than the particle current. The units pnA, pµA and pmA for *particle nano-/micro-/milliamperes* have come into use to accommodate this dichotomy [125].

Part II

RESEARCH AND DESIGN

4

HELIAC BEAM DYNAMICS LAYOUT

Unless otherwise stated, the simulations presented in this chapter have been performed with LORASR, versions 2018.08.01 and 2020.01.23 (and/or the associated batch versions 2018-08-22 and 2021-04-23) using 100000 Waterbag[1]-distributed macroparticles, at a beam current of $I = 1\,\mathrm{mA}$ and with a mass-to-charge ratio of $A/z = 6$. The macroparticle density of all particle phase space portraits is logarithmically color-coded on a rectangular grid of $\geqslant 120 \cdot 120$ data points superimposed over the phase space region used. On the right and above the density plots, histograms are shown in gray to visualize the density profile for the corresponding plane.

4.1 GSI AND THE HLI

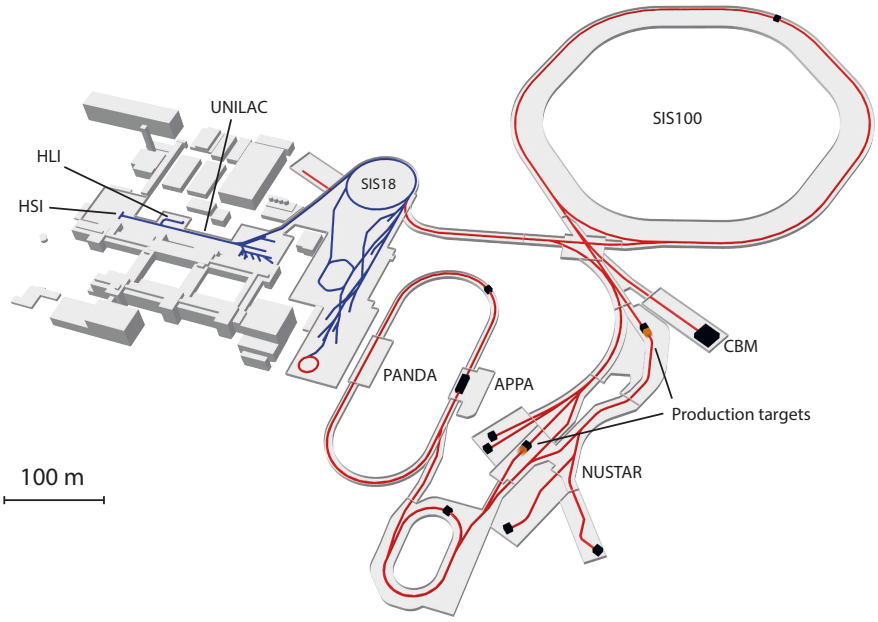

Figure 4.1: Schematic layout of GSI and FAIR. The existing GSI facilities are colored in blue. The planned FAIR facilities are shown in red. (Figure adapted from [126])

The GSI Helmholtz Centre for Heavy Ion Research (GSI) is a large-scale research facility, whose particle accelerators enable basic research with ion beams, in particular to gain new insights into the building blocks of matter. It was founded in 1969 under the German

1 A Waterbag distribution is a homogeneously particle-filled 6D hyperellipsoid, which is a common choice for beam dynamics simulations (see also Section 2.1.1).

name *Gesellschaft für Schwerionenforschung mbH*. At GSI, research in the fields of nuclear physics, atomic physics, plasma physics, materials research, biophysics and tumor therapy are conducted with accelerated ions ranging from helium (He) to uranium (U). After the foundation, construction of the 150-meter-long linear accelerator UNILAC near Darmstadt, Germany began. Since 1975, GSI has been conducting experiments with ions from helium to uranium. Since 1990, the heavy ion synchrotron SIS18 and the Experimental Storage Ring (ESR) have been in operation as extensions. In 1991, the High Charge State Injector HLI was put into operation, enabling UNILAC-operation without any stripping process at 1.4 MeV/u. This allowed the discovery of the elements 110, 111 and 112. Figure 4.1 gives a general overview of GSI with its accelerators and its experiments.

In order to be able to answer further fundamental questions about the structure of matter and the universe, one of the largest research projects worldwide, an international research facility for research with antiprotons and ions called FAIR[2] is being built at GSI. The existing accelerator facility at GSI will then serve as an injector for the FAIR accelerator facility [127, 128], whereby FAIR will provide ion beams of previously unattained intensities and energies for research. For this purpose, some of the following GSI facilities, like the proton linac pLinac [129, 130], the Universal Linear Accelerator (UNILAC) [25, 131–134], the linear heavy ion decelerator HITRAP (Heavy Ion TRAP) [135, 136], the LIGHT (Laser Ion Generation, Handling and Transport) facility for laser acceleration of protons and heavy ions [137, 138] and the Heavy Ion Synchrotron (SIS18), are upgraded or expanded.

As a further result, the availability of beam time with a high duty cycle for superheavy element research at GSI's Universal Linear Accelerator (UNILAC, see Figure 4.2) will be greatly reduced due to the duty cycle limitation for the operation of FAIR. Besides, an upgrade program of the High Charge State Injector (HLI) was already initialized comprising a new 18 GHz electron cyclotron resonance ion source (ECR), a CW capable radio frequency quadrupole (RFQ) [139] and an interdigital *H*-mode drift tube linac (IH-DTL), keeping the SHE program at GSI competitive.

It is assumed that an additional standalone superconducting CW linac (HELIAC) will best meet the requirements of the experimental program. With a significant higher beam intensity, the SHE production rate could also be increased. The upgraded HLI will then serve as the injector for HELIAC.

4.2 DESIGN EVOLUTION

Initial considerations for an upgraded and optimized linac for SHE research at GSI were discussed internationally in workshops in the early

2 Acronym for *Facility for Antiproton and Ion Research*.

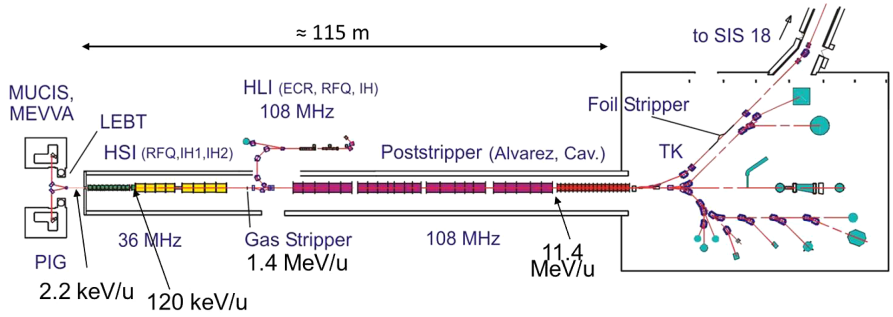

Figure 4.2: Schematic layout of the UNILAC. [140]

2000s [105, 106]. A very preliminary approach for the beam dynamics design of a corresponding superconducting linac was then studied by Minaev *et al.* and published a few years later [28]. Nevertheless, the main focus of that research work was on the analysis and theoretical description of the EQUUS beam dynamics concept, as well as the rudimentary investigation of whether this concept could in principle be considered for such an accelerator. The resulting conclusion was very optimistic about the basic applicability of this novel concept, so it was also chosen for the work done within this thesis. However, as the research focus was set on the theoretical investigation of EQUUS, many of the assumptions made for the preliminary proof-of-principle beam dynamics design were actually very simplified. As a result, while retaining the basic EQUUS concept, the beam dynamics design had to be created from scratch in this thesis.

Some of the parameters initially assumed in a deliberately simplified manner by Minaev *et al.* are [141]:

- The ratio of gap length to drift tube length within all cavities:
  It has been assumed to be $\frac{l_{\text{gap}}}{l_{\text{drifttube}}} = 1$. This is a valid first assumption, but realistically varies roughly from about $\frac{l_{\text{gap}}}{l_{\text{drifttube}}} = 0.3$ to 2 in H-mode cavities in the low- and medium-energy range (see Figure 4.3). As a result, the assumed transit time factors also differed from the current ones, which is an additional factor influencing the differences from the beam dynamics at that time.

- The voltage distribution:
  It was assumed to be constant within each cavity (see Figure 4.5 on p. 42). Furthermore, the assumed voltage distribution within the cavities with this geometry of gap and drift tubes would not be physically possible in the H_{211} mode used.

- The drift tube aperture:
  For CH0[3], a diameter of 20.5 mm was initially assumed here. In

3 The naming of the CH cavities has changed compared to the paper by Minaev *et al.* The first CH cavity in the design at that time was named "C1" (see also Figure 4.4), in the HELIAC design it is "CH0" (counting starting with the digit "0", as this cavity represents the prototype or demonstrator cavity).

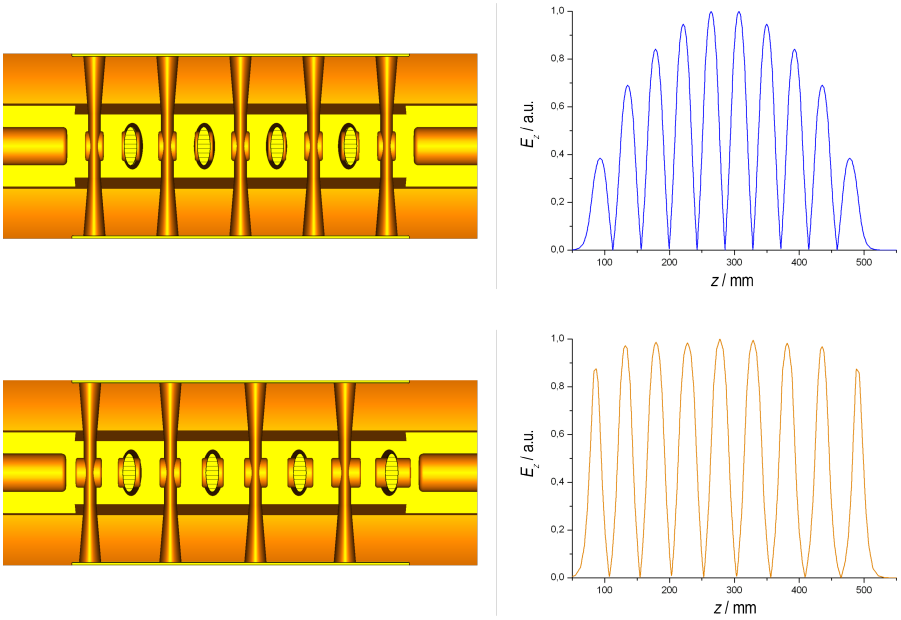

Figure 4.3: Cross-sectional views of two CH-DTL cavities *(left)* and the corresponding $E_z(z)$-field distribution on the ideal beam axis *(right)*. *Top:* $\frac{l_{\text{gap}}}{l_{\text{drifttube}}} = 1$ leading to a decreasing amplitude to the sides (quasi H_{211}-mode). *Bottom:* Variation of $\frac{l_{\text{gap}}}{l_{\text{drifttube}}}$ within the cavity to flatten the field distribution (quasi H_{210}-mode). [142, modified]

the built cavity CH0, however, this value was varied between 18 and 20 mm.

- The length of the cavities:
  Values exceeding 1 m in some cases were assumed. For the HELIAC design, however, the cavity lengths were limited. CH0 represents the longest cavity with 0.81 m. The remaining superconducting CH cavities have lengths between 0.59 and 0.73 m. This allows an easier manufacturing, preparation and handling of the cavities.

- The distance between cavities:
  This value respectively the deviations between the original assumptions of Minaev *et al.* and the values for HELIAC, which have been checked for realistic feasibility, probably represent one of the decisive differences. Two cases are to be distinguished here. On the one hand, two directly adjacent cavities:

  · While the distance between the last gap center of cavity n and the first gap center of cavity $n+1$ was assumed to be 20 cm in the former approach, this value is more than twice as large in HELIAC at over 40 cm.

  And on the other hand, two adjacent cavities with a magnetic solenoid in between:

  - In their approach, Minaev *et al.* set 60 cm as distance between the last gap center of cavity n and the first gap center of cavity $n+1$ when placing a solenoid of 30 cm effective length in between. However, $108-113$ cm have been determined to be a realistic minimum distance for the HELIAC design.

- Details about the cryostat geometry:
  Minaev *et al.* state in their paper *"the cylindrical cryostats might be about 5 m in length"* [28], but no further details were given about their exact lengths and positions. Crucial from a beam dynamics point of view is in particular the additional drift distance due to the cold-warm and warm-cold transition of two neighboring cryostats. At Minaev *et al.* (see Figure 4.4) it is most likely that such an intermediate cryomodule section could be placed between the cavities C3 and C4 (there also called transition between "fixed energy" and "variable energy" part). Nevertheless, only 90 cm are provided here between the last gap center in cryomodule n and the first gap center in cryomodule $n+1$. In the HELIAC design, however, it was found that for a realistic and buildable design this distance has to be longer than 200 cm, even though both cases only include one solenoid and some beam diagnostics in between.

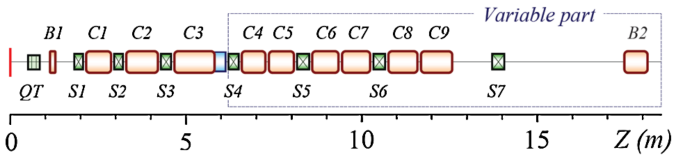

Figure 4.4: Schematic layout of the superconducting heavy ion linac by Minaev *et al.* [28].

At the beginning of this work, the beam dynamics properties of the CH0 cavity, which had already been built and which was in the final preparation phase, were investigated. Also, with regard to the two subsequent structures CH1 and CH2, different approaches for the first expansion stages of the HELIAC accelerator were studied. This focused on the evaluation of possible layouts, but at the same time the goal was to be able to use as many components of the test phase (in particular cryomodules) as possible for the entire accelerator in the future. After CH0 was tested very successfully in a separate cryomodule with two superconducting solenoids [8], the decision was made to develop a cryomodule for the commissioning of the cavities CH1 and CH2, which also contains CH0 and will be used in the future as the first cryomodule of the entire HELIAC (CM1). Parallel to this, optimizations have been made to the matching line after the HLI [143]. Based on the successful commissioning of CH0, it was decided to use higher acceleration gradients of up to $E_a = 7.1\,\mathrm{MV/m}$. At the

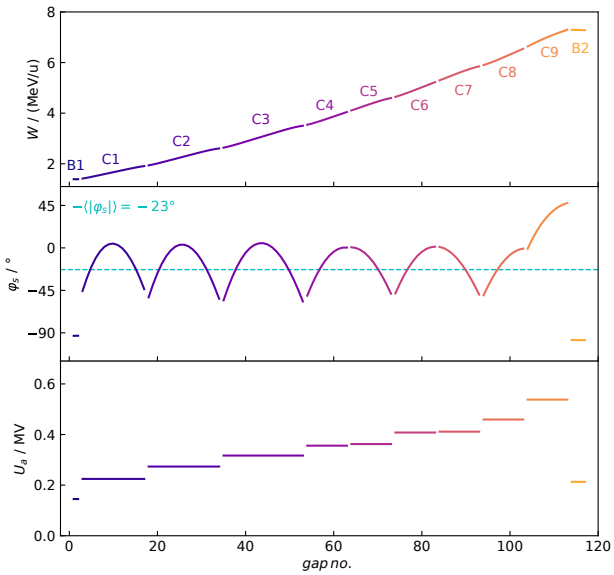

Figure 4.5: Linac approach by Minaev *et al.*; shown is the evolution of the mean bunch energy W, the reference phase φ_s and the effective voltage per gap U_a.

same time, it became apparent that the significantly higher distances between individual components compared to Minaev's preliminary approach (see also the previous listing) made the beam dynamics of the accelerator much more challenging. Thus, for additional longitudinal stability and flexibility, the use of buncher cavities was then investigated. Here the question was both whether these could also be normal conducting cavities in the intertank sections, or in the case of superconducting cavities, where these should be placed best. In the end, it was found that one superconducting buncher cavity per cryomodule is a good choice. The cryomodules themselves were then technically designed to be as long as possible to avoid frequent cold-warm transitions and associated drifts, and at the same time as short as necessary for good handling. After several iterations, trying to keep the distances between individual components as short as possible, the cryomodules in the suggested HELIAC design now have lengths of just under 5 m. The details of the beam dynamics layout of HELIAC in its various stages of expansion are presented in the following.

4.3 ADVANCED DEMONSTRATOR

After the very successful cold tests [144] and subsequent promising beam tests [8] with the CW Demonstrator Cavity (named CH0 for HELIAC) the originally intended acceleration gradient of 5.1 MV/m [28] for all the CH-cavities of this linac could be increased. As CH0 was already built at that time and CH1 and CH2 had been in the manufacturing process, it has been decided within the research for

this thesis to gradually increase the gradient with each cavity up to a maximum value of $E_a = 7.1\,\mathrm{MV/m}$ (see Figure 4.6).

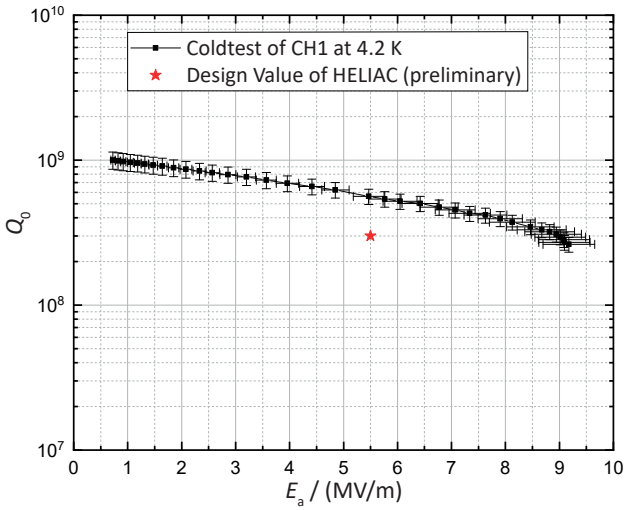

Figure 4.6: Plot of the measured quality factor Q_0 as function of the acceleration gradient E_a of CH1 [32, modified]. The figure reveals the possibility of increasing the design gradient targeted so far.

Thus, there is a compromise between very high acceleration efficiency, with nevertheless available safety buffer in case of individual performance limitations in cavities. In addition, the gradual increase of the gradient does not increase the beam velocity too far at the beginning, so that the cavities of the Advanced Demonstrator (named CM1 at the full-expansion stage of HELIAC) are not operated too high above their reference energy, which would otherwise lead to beam quality and acceleration efficiency degradation. The next milestone within this research will be the construction, commissioning and testing of the multi-cavity superconducting Advanced Demonstrator.

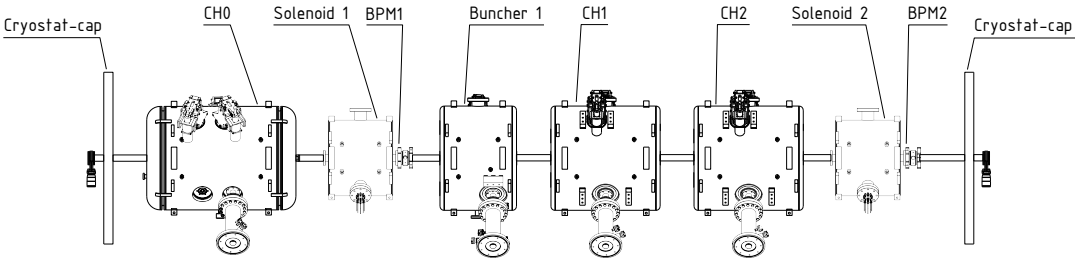

Figure 4.7: Conceptual layout scheme of the Advanced Demonstrator cryomodule CM1. Vacuum gate valves on the outer sides, CH-cavities, solenoids, a buncher cavity and two beam position monitors (BPM) for beam diagnostic purposes are depicted.

The Advanced Demonstrator includes the cryomodule CM1 equipped with demonstrator cavity CH0, two more CH cavities CH1 and CH2 [32], two solenoids and a short Buncher cavity of the single spoke type [13]. For beam diagnostic purposes two Beam Position Monitors (BPM)

are foreseen. The sequence of components inside the cryomodule is shown in Figure 4.7. The flange-to-flange length is about 4.5 m. Further details are given in Table 4.1. In the future, this cryomodule CM1 is the first in a series of four cryomodules for the entire HELIAC. So, the input beam parameters are the same in both cases and given in Table 4.4 (p. 52).

	CH0	B1	CH1	CH2
Gap number	15	2	8	8
Total length / mm	811	416	593	593
Cell length ($\beta\lambda/2$) / mm	40.8	44.1	47.7	47.7
$U_{\mathrm{a,total}}$ / MV	3.4	0.5	2.3	2.5

Table 4.1: Main parameters of the Advanced Demonstrator cavities.

4.3.1 *Choice of Transverse Focusing Structure*

As transverse focusing elements quadrupole doublets, quadrupole triplets and solenoids are basically available. As mentioned before, solenoids have been chosen for HELIAC which is regarded as common practice for low-energy superconducting linacs (see [36]). The solenoid prototype uses NbTi and Nb_3Sn as material for the coils, while the next solenoids will be made only of NbTi. By choosing solenoids, the overall length and cost of the machine can be reduced. Thus, less space is lost to the regions between the cryomodules and as a consequence of the increased packing of the cavities the longitudinal acceptance is increased. It also simplifies the operation of the linac, since only one solenoid (and not two or three quadrupole singlets) needs to be controlled per focusing unit. Quadrupoles might seem more reasonable at first, since their focal length $1/f$ is proportional to the inverse particle speed $1/v$, while for solenoids it is proportional to $1/v^2$. At higher beam velocities, quadrupoles therefore gain increasingly in efficiency compared to solenoids. Due to the aforementioned reasons and since superconducting solenoids can reach a very strong magnetic field (here up to about 9 T), solenoids are the more suitable choice for HELIAC.

Niobium–titanium (NbTi) and niobium-tin (Nb_3Sn) are metallic alloys of niobium and titanium resp. tin often used as type-II superconductor wire.

In addition, and especially advantageous for HELIAC requirements, solenoids have a higher tolerance to beam mismatch and a higher acceptance to beams with multiple charge states [145]. The solenoids for HELIAC have an effective length of $L_{\mathrm{eff}} = 298\,\mathrm{mm}$ [146] and are made of three coil-sets (see Figure 4.8): A main solenoid, two shield coils in an Helmholtz-like configuration connected in series with the main solenoid and two dipole pairs for steering the beam in horizontal and vertical direction. The required amount of steering

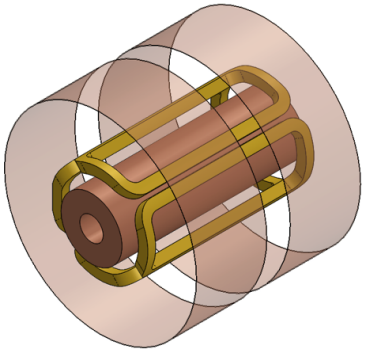

Figure 4.8: Schematic layout of the three sets of coils for the HELIAC superconducting solenoids.

potential – including a sufficient safety buffer – was estimated to a maximum deflection angle of $\theta \stackrel{!}{=} 20\,\text{mrad}\,(\approx 1.15\,^\circ)$, including a large safety margin. The resulting required magnetic fields for the dipole pairs can be calculated for small angles as follows:

$$\tan(\Delta\theta) \approx \theta \approx \frac{p_\perp}{p_\parallel} \approx \frac{p_\perp}{p}$$

With Δp as transv. momentum change, p as longit. momentum and the angle change by the field as $\Delta\theta$, we get:

$$\begin{aligned} \Delta\theta &= \frac{\Delta p}{p} && (4.1)\\ &= \frac{1}{p}\frac{\Delta p}{\Delta t}\frac{\Delta t}{\Delta z}\Delta z && (4.2)\\ &= \frac{1}{p(\frac{\Delta z}{\Delta t})}\frac{\Delta p}{\Delta t}\Delta z && (4.3) \end{aligned}$$

Δz is the distance a particle travels through the field in the time Δt, while the deflecting force is impinging on it. Here this is equal to the effective length of the solenoid L_{eff}. In differential notation:

$$\begin{aligned} \Delta\theta &= \frac{1}{p(\frac{dz}{dt})}\frac{dp}{dt}\,dz && (4.4)\\ &= \frac{1}{pv}F\,dz && (4.5) \end{aligned}$$

$$\begin{aligned} \Rightarrow \theta &= \frac{1}{pv}\int_0^{L_{\text{eff}}} F\,dz && (4.6)\\ &= \frac{1}{pv}\int_0^{L_{\text{eff}}} qvB\,dz && (4.7)\\ &= \frac{q}{p}\int_0^{L_{\text{eff}}} B\,dz && (4.8) \end{aligned}$$

$$\Rightarrow B = \frac{p\theta}{qL_{\text{eff}}} \tag{4.9}$$

$$= (B\rho)\frac{\theta}{L_{\text{eff}}} \tag{4.10}$$

The HELIAC-specific energy range extends from 1.39 MeV/u (input energy) to 7.3 MeV/u (output energy). For the desired deflection angle as a function of the beam's mass-to-charge-ratio A/z, kinetic energy W_{kin} and magnetic rigidity $B\rho$ the calculated values are given in Table 4.2. The dipole pairs are therefore designed to provide a maximum integrated field of $B \cdot L_{\text{eff}} = 0.07$ Tm to ensure that the deflection angle can be reached for $W_{\text{kin}} = 7.3$ MeV/u even at $A/z = 8.5$.

W_{kin} = **1.39** MeV/u	$A/z = 3$	6	8.5
$B\rho$ / Tm	0.50942	1.01884	1.44335
B / T	0.03419	0.06838	0.09687
$B \cdot L_{\text{eff}}$ / Tm	0.01019	0.02038	0.02887

W_{kin} = **7.3** MeV/u	$A/z = 3$	6	8.5
$B\rho$ / Tm	1.16927	2.33855	3.31294
B / T	0.07847	0.15695	0.22235
$B \cdot L_{\text{eff}}$ / Tm	0.02339	0.04677	0.06626

Table 4.2: Required magnetic values for the dipole magnets' deflection angle of 20 mrad for different beam energies and mass-to-charge ratios.

4.3.2 *Beam Dynamics Design*

In general, it can be stated that the beam dynamics design for HELIAC and thus also partially for the intermediate stages (here Advanced Demonstrator) is ambitious in several aspects. Ultimately, not only a highly efficient superconducting linac will be developed using several multi-gap CH cavities at highest acceleration gradients, which is unique worldwide so far, but the high requirements also extend to the beam to be accelerated: Here, a smooth energy variation of 3.5 to 7.3 MeV/u must be provided while achieving an energy spread of constantly below ± 3 keV/u and with full beam transmission.

For SHE experiments the beam energy spread before hitting the target should typically be in the order of $\Delta W/W \approx 10^{-3}$ [147]. As men-

tioned, for HELIAC this value was set to $\pm 3\,\mathrm{keV/u}$ ($\Delta W = 6\,\mathrm{keV/u}$), which corresponds to

$$\frac{\Delta W}{W} = \frac{6\,\mathrm{keV/u}}{3.5\,\mathrm{MeV/u}} = 1.7 \cdot 10^{-3} \tag{4.11}$$

for $W = 3.5\,\mathrm{MeV/u}$ which is the minimum energy and

energy spread

$$\frac{\Delta W}{W} = \frac{6\,\mathrm{keV/u}}{7.3\,\mathrm{MeV/u}} = 0.8 \cdot 10^{-3} \tag{4.12}$$

for $W = 7.3\,\mathrm{MeV/u}$ being the maximum energy HELIAC has to provide.

The pursued beam dynamics approach is based on a variant of EQUUS in which the sliding movement in the longitudinal phase space does not always take place within one cavity (as in CH0), but is also split between two adjacent cavities for some cavities (see Figure 4.9 for the EQUUS-split between CH1 and CH2). This allows for even greater flexibility in terms of beam acceptance and energy variability. In CH1, a negative synchronous phase of approximately $\varphi_s = -35°$ is injected with an energy deficiency and the bunch then moves counter-clockwise in the direction of $\varphi_s = 5°$. The beam is then injected into the second cavity, reaching approximately the reference energy at about $\varphi_s = 10°$ and then moves to even higher energies and negative synchronous phases around about $\varphi_s = -60°$.

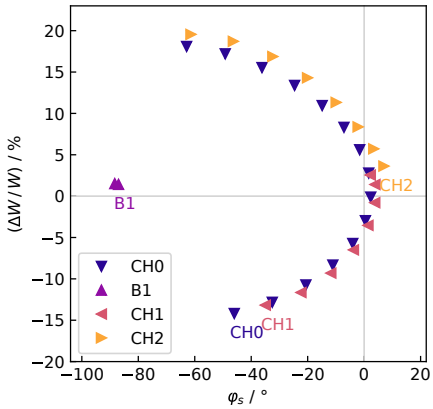

Figure 4.9: LORASR-simulated evolution of the relative mean bunch energy $\Delta W/W$ (in relation to each cavity's reference energy) and the reference phase φ_s along the cavities CH0, B1, CH1 and CH2; $W_{out} = 2.7\,\mathrm{MeV/u}$; the labels with the cavity names indicate the data point for the first gap of each cavity.

A set of beam dynamics simulations have been performed with LORASR for the design ions ($A/z = 6$), considering increased acceleration gradients compared to the initial value of $E_a = 5.1\,\mathrm{MV/m}$ in 2009 [28]. A compromise between the highest acceleration gain and the lowest degradation of the beam quality, in particular in the

$E_a = U_a/L$, with $L = n \cdot \beta\lambda/2$ is used as definition for the acceleration gradient for an n-gap cavity throughout this thesis.

longitudinal phase plane, had to be envisaged in the optimization process.

The beam dynamics simulations were performed with 10^5 Waterbag-distributed macro-particles at a beam current of 1 mA. The simulated beam envelopes and phase space portraits are shown in Figure 4.10 and Figure 4.11 respectively. Finally, with the optimized settings, CH0 is operated at $E_a = 5.75\,\mathrm{MV/m}$, CH1 at $E_a = 6.0\,\mathrm{MV/m}$, CH2 at $E_a = 6.5\,\mathrm{MV/m}$ and the buncher B1 at $E_a = 5.7\,\mathrm{MV/m}$. The resulting output beam energy is 2.7 MeV/u. The particle transmission for the beam with initial parameters defined from the measured data and from the results of previous simulations [12] is 100 %. Thus, in accordance with the specifications, no particle loss occurs.

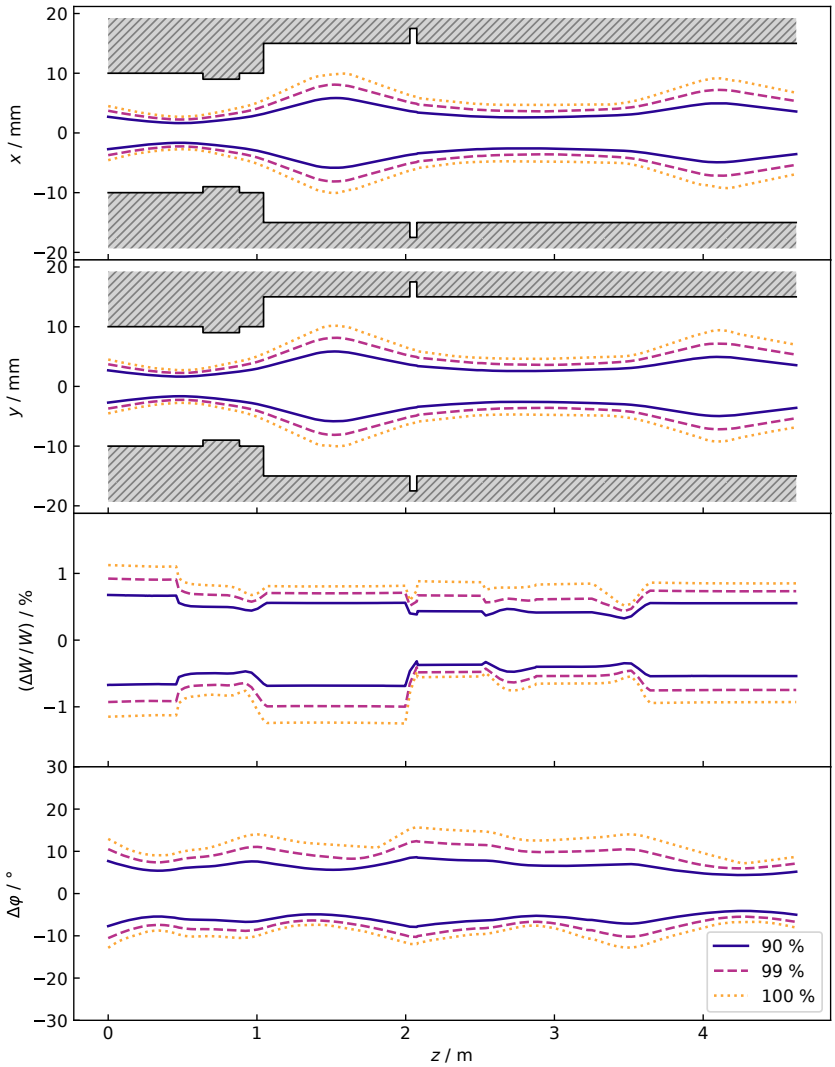

Figure 4.10: Beam envelopes simulated along the Advanced Demonstrator showing a smooth movement in all planes without beam loss. The aperture is indicated by the hatched gray areas.

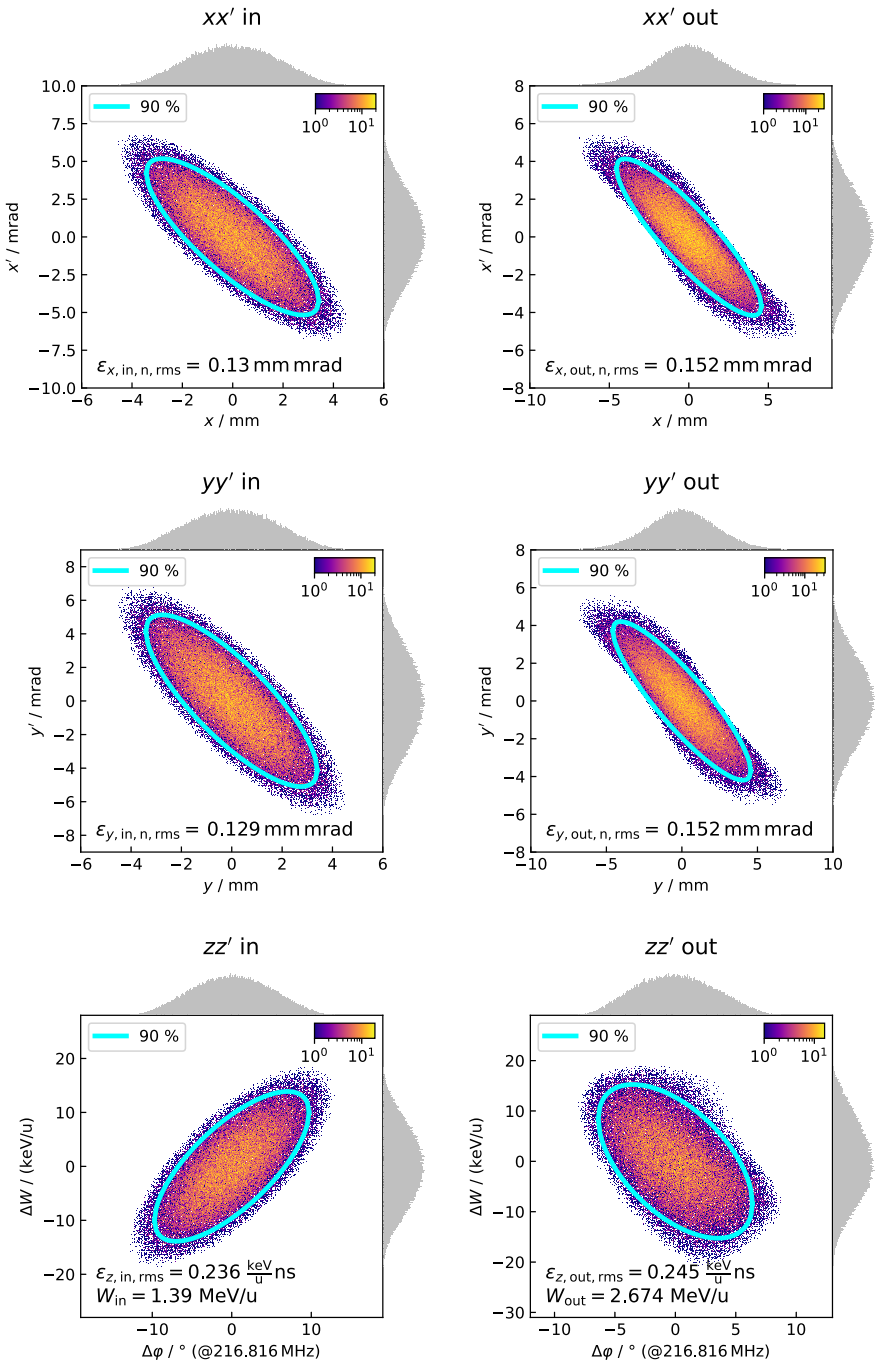

Figure 4.11: Simulated transverse and longitudinal phase space portraits at the injection (*left*) and exit (*right*) of the Advanced Demonstrator.

4.4 HELIAC

After the design of the Advanced Demonstrator yielded promising results, the design of the entire linac was started while maintaining the essential design characteristics of CM1. Main parameters for the HELIAC beam dynamics simulations are given in Table 4.3.

Simulation and Linac Parameters	
Total length	30 m
Length (superconducting part)	20 m
Number of cavities	17
Accel. gradient E_a	$\leqslant 7.1\,\mathrm{MV/m}$
Required beam transmission	100 %
Operating frequency	$n \cdot 108.408\,\mathrm{MHz}$
Beam properties	
Number of macro particles	$1 \cdot 10^5$
Particle distribution type	6D Waterbag
3D PIC grid	$64 \cdot 64 \cdot 64$
Beam current I	$\leqslant 1\,\mathrm{mA}$
Mass-to-charge ratio A/z	$\leqslant 6$
Injection energy W_{in}	$1.390\,\mathrm{MeV/u}$
Exit energy W_{out}	$3.5\,\mathrm{MeV/u} - 7.3\,\mathrm{MeV/u}$
Exit energy spread ΔW_{out}	$\pm 3\,\mathrm{keV/u}$
$\varepsilon_{\mathrm{rms}}$ (xx' and yy')	0.13 mm mrad
$\varepsilon_{\mathrm{rms}}$ (φW)	$0.236\,\mathrm{keV/u} \cdot \mathrm{ns}$
$\varepsilon_{100\%}$ (xx' and yy')	1.12 mm mrad
$\varepsilon_{100\%}$ (φW)	$2.18\,\mathrm{keV/u} \cdot \mathrm{ns}$
Solenoids	
Total length	400 mm
Effective length	298 mm
Number of solenoids	8 (2 per cryomodule)
Magnetic field	$\leqslant 6.35\,\mathrm{T}$
Beam aperture diameter	30 mm

Table 4.3: Main linac and LORASR simulation parameters of HELIAC. $n = 1$ for the final buncher cavity FB, $n = 2$ for the superconducting HELIAC-part.

4.4.1 *Full Layout with 4 Cryomodules*

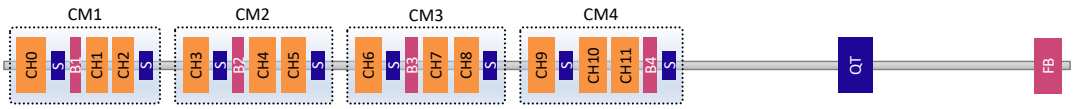

Figure 4.12: Schematic HELIAC layout with cryomodule, cavity and magnet positions. The total length is about 30 m.

From a beam dynamics point of view, a layout with as few cryomodules as possible would be preferable, since it has the fewest cold-to-warm transitions and thus minimizes the number of beam drifts. These are undesirable as they cannot be used effectively for either diagnostic or focusing purposes. In contrast, any additional drift section causes the beam to widen, which is more likely to result in beam quality degradation. At the same time, however, the maximum length of the cryomodules must be short enough so that they can still be handled (from a mechanical point of view). Therefore, the maximum permitted length of the cryomodules for HELIAC was limited to 5 meters. Therefore, after extensive investigations, the HELIAC cavity layout is as follows:

It comprises twelve superconducting CH-DTL cavities (CH0 to CH11), operated at 216.816 MHz and grouped in four cryomodules (CM1 to CM4) with a total length of about 20 m (Figure 4.12). Based on the design of the Advanced Demonstrator (Section 4.3.1), each cryomodule contains three CH-DTL cavities, one spoke-type buncher [14] and two magnetic solenoids (including a BPM downstream each solenoid). The buncher cavities in each cryomodule adjust the beam phase- and/or energy-spread, providing longitudinal beam matching at varying acceleration gradients and the corresponding varying beam energies. The buncher position in CM4 is moved to the downstream end of CM4 to increase the beam dynamics' flexibility prior to the subsequent drift in the beam transport section. The superconducting part is followed by a normal conducting part of about 10 m length. It uses a magnetic quadrupole triplet (QT) for transverse focusing and a final buncher cavity (FB) that provides the required narrow beam energy spread of ± 3 keV/u. Main parameters of the HELIAC cavities are given in Table 4.4.

The use of BPMs directly downstream all solenoids is recommended as a minimum equipment for beam diagnostics inside the cryomodules. This allows the transverse center of gravity position of the beam to be precisely measured in order to make any necessary changes to the solenoid field strength or the associated dipole correction coils. In addition, ToF[4] measurements should be performed to determine the

4 Time-of-Flight measurement, see [148] for a detailed explanation and [149, 150] for examples.

Table 4.4: Main parameters of the HELIAC cavities.

Cryo-module	Cavity	Gap no.	Length / m	$(\beta\lambda/2)$ / mm	$U_{a,total}$ / MV	E_a / (MV/m)	W_{out} / (MeV/u)
CM1	CH0	15	0.81	40.8	3.4	5.8	1.9
	B1	2	0.42	44.1	0.5	5.7	1.9
	CH1	8	0.59	47.7	2.3	6.0	2.3
	CH2	8	0.59	47.7	2.5	6.5	2.7
CM2	CH3	8	0.69	56.7	3.2	7.1	3.2
	B2	2	0.44	57.3	0.6	5.5	3.2
	CH4	8	0.72	59.6	3.4	7.1	3.8
	CH5	7	0.68	62.4	3.1	7.1	4.3
CM3	CH6	7	0.73	70.3	3.5	7.1	4.9
	B3	2	0.46	67.7	0.2	1.5	4.9
	CH7	6	0.69	73.6	3.1	7.1	5.4
	CH8	6	0.69	73.9	3.1	7.1	5.9
CM4	CH9	6	0.73	81.7	3.5	7.1	6.4
	CH10	5	0.67	83.6	3.0	7.1	6.9
	CH11	5	0.67	83.9	2.5	6.0	7.3
	B4	2	0.59	78.1	0.4	2.3	7.3
	FB	2	0.45	156.2	0.4	1.3	7.3

beam energy and adjust the RF phases of the cavities. The latter is probably one of the biggest challenges in operating the HELIAC, due to the limited options for placing and using beam diagnostic elements. In the inter-cryomodule region, the minimum equipment for beam diagnostics involves the measurement of the beam current by means of a beam transformer and phase probes for the longitudinal phase space.

Figure 4.13 shows the simulated beam envelopes along the entire HELIAC. They are well-defined without any particle beam loss. Since the design of the beam dynamics focuses on a maximum energy gain at the shortest distance, the transverse envelopes propagate without a constant periodicity, in contrast to conventional beam dynamics designs where this periodicity often becomes visible. However, the requirement of a maximum cryomodule length of 5 m with the resulting inevitable long drift distances between adjacent cryomodules (in addition to the drifts that also noticeably occur between the cavities within the cryomodule) is a significant challenge here. Therefore, classical design approaches that primarily focus on the longitudinal and

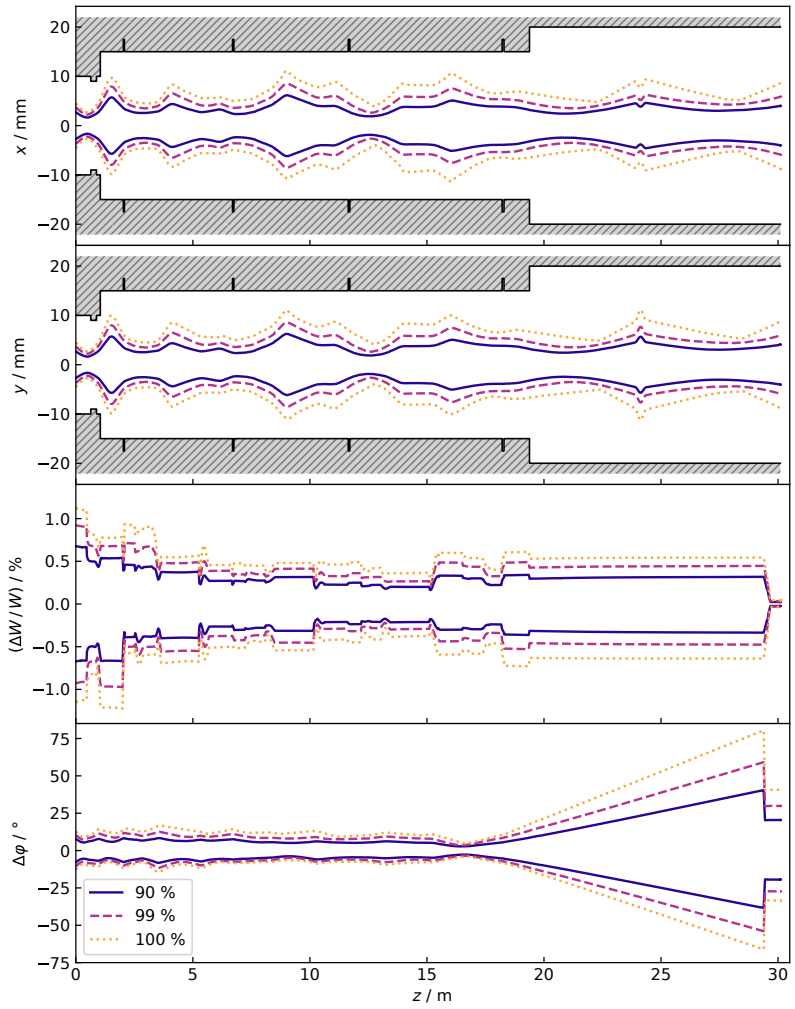

Figure 4.13: Simulated beam envelopes along the entire HELIAC. The phase jump at the end of the beam line corresponds to the halved operating frequency of the buncher FB.

transverse phase advance of the design could not be fully applied for this accelerator design.

Nevertheless, the simulated beam can clearly be reliably transported to the required maximum energy of 7.3 MeV/u for mass-to-charge-ratios of up to 6. The characteristic counterclockwise crescent-shaped EQUUS motion for all CH cavities is shown in Figure 4.14. It can also be seen from the plot that the superconducting buncher cavities B3 and B4, as well as the normal-conducting buncher FB are designed for a lower reference energy and geometric β, respectively ($\Delta W/W$ is $\gg 0\,\%$ here). This was intentionally chosen to achieve high energy acceptance and a good working point for the entire required energy range from 3.5 to 7.3 MeV/u.

The evolution of the reference phase from the first to the last acceleration gap of the HELIAC design is shown in Figure 4.15. It can be seen how the phase slip gradually decreases with each CH cavity

and approaches the mean value of $-\langle|\varphi_s|\rangle = -21°$. "Outliers" in this phase progression are, as intended, exclusively the buncher cavities.

Figure 4.16 depicts the simulated transverse and longitudinal phase space portraits at injection and exit of the HELIAC. The required output energy of $W_{\text{out}} = 7.3\,\text{MeV/u}$ is reached with an energy spread well inside the range of $\pm 3\,\text{keV/u}$. The rms-emittance growth is moderate with increases of $+10\,\%$ (xx'), $+11\,\%$ (yy') and $+14\,\%$ (zz').

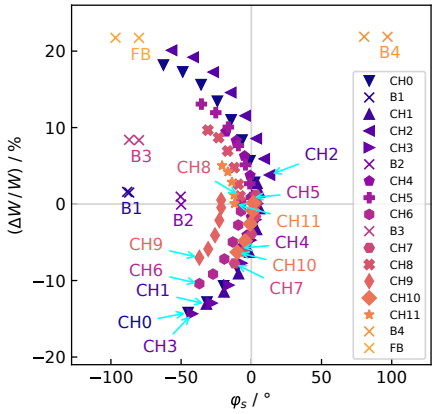

Figure 4.14: Bunch center motion plot for HELIAC showing the reference phase φ_s of each gap and the deviation from the reference energy of each cavity.

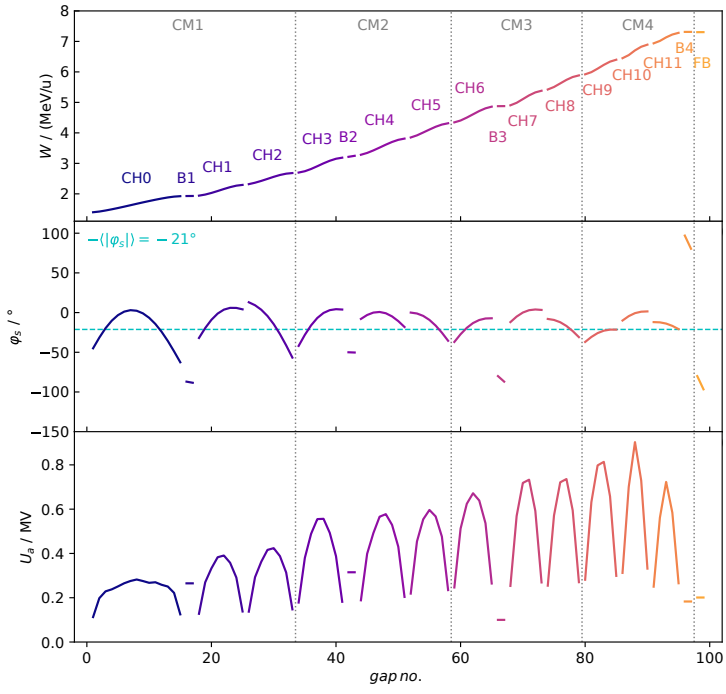

Figure 4.15: Evolution of the mean bunch energy W, the reference phase φ_s and the effective voltage per gap U_a along the HELIAC.

While initial design approaches for HELIAC were carried out manually and repeatedly adapted in coordination with the scientists at GSI due to frequently changing boundary conditions (among other things due to new component lengths for mechanical reasons), optimization routines were used in the further stages. A previously selected multidimensional parameter space (e. g. ranges of RF phases and field amplitudes of the cavities, positions of the buncher cavities inside the CMs and solenoid field strengths) was systematically simulated, partly also by using computational methods such as particle swarm

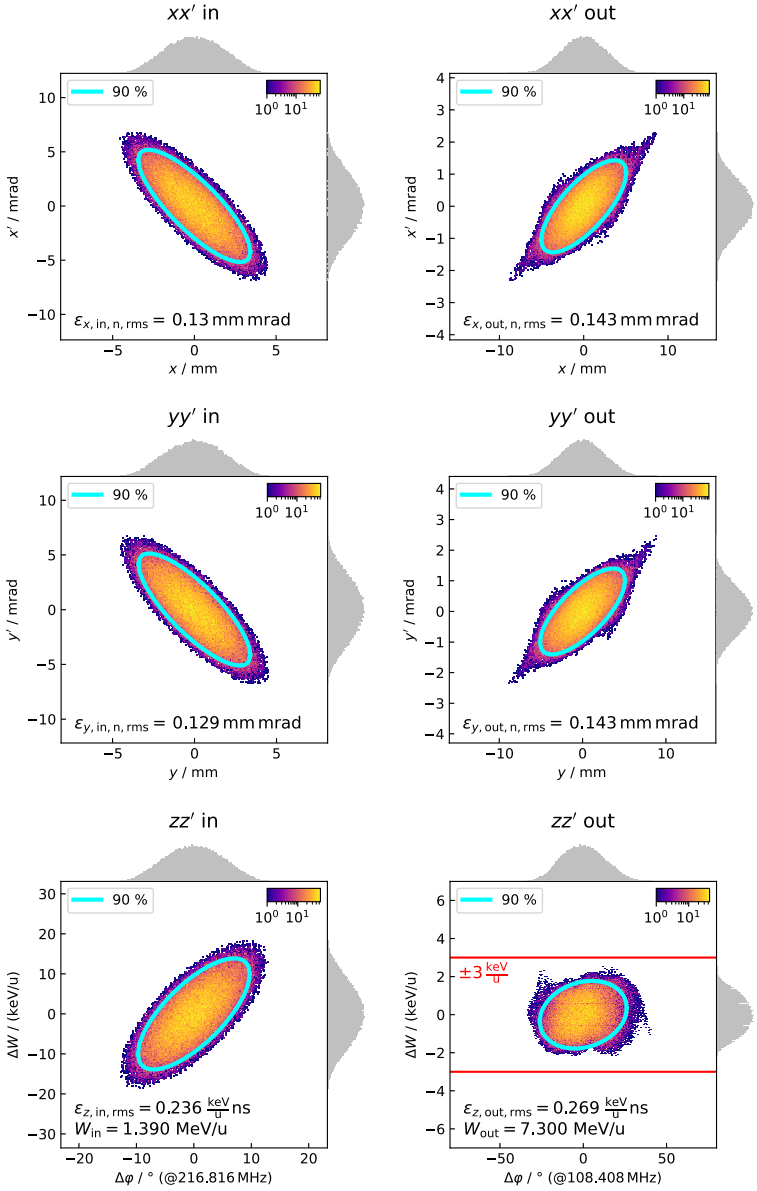

Figure 4.16: Simulated transverse and longitudinal phase space portraits at injection and exit of the HELIAC. The required output energy of $W_{\text{out}} = 7.3\,\text{MeV/u}$ is reached with an energy spread well inside the range of $\pm 3\,\text{keV/u}$ *(bottom right)*.

optimization [151, 152]. For the optimization cost function Λ, depending on the use case and design status, a multi-parameter approach was used:

$$\begin{aligned}\Lambda = {} & \Delta\epsilon_{x,\mathrm{rms}}{}^{\lambda_1} \cdot \Delta\epsilon_{y,\mathrm{rms}}{}^{\lambda_2} \cdot \Delta\epsilon_{z,\mathrm{rms}}{}^{\lambda_3} \cdot \Delta\epsilon_{x,100\%}{}^{\lambda_4} \cdot \Delta\epsilon_{y,100\%}{}^{\lambda_5} \cdot \Delta\epsilon_{z,100\%}{}^{\lambda_6} \\ & \cdot T^{-\lambda_7} \cdot \mu_{\Delta x}{}^{\lambda_8} \cdot \mu_{\Delta y}{}^{\lambda_9} \cdot \mu_{\Delta\varphi}{}^{\lambda_{10}} \cdot \sigma_{\Delta x}{}^{\lambda_{11}} \cdot \sigma_{\Delta y}{}^{\lambda_{12}} \cdot \sigma_{\Delta\varphi}{}^{\lambda_{13}} \\ & \cdot x_{\max}{}^{\lambda_{14}} \cdot y_{\max}{}^{\lambda_{15}} \cdot \varphi_{\max}{}^{\lambda_{16}} \cdot \Delta\varphi_{\mathrm{out}}{}^{\lambda_{17}} \cdot \Delta W_{\mathrm{out}}{}^{\lambda_{18}}.\end{aligned} \tag{4.13}$$

The main variation parameters were the rms emittance growth in all planes $\Delta\epsilon_{x/y/z,\mathrm{rms}}$, the 100 % emittance growth in all planes $\epsilon_{x/y/z,100\%}$, the beam transmission T, the mean transverse beam widths $\mu_{\Delta x/y}$ and phase width $\mu_{\Delta\varphi}$, and their standard deviations $\sigma_{\Delta x/y/\varphi}$, the maximum transverse envelope amplitudes ($x_{\max}/y_{\max}$) and longitudinal envelope amplitude $\varphi_{\max}$, as well as the phase width $\Delta\varphi_{\mathrm{out}}$ and energy width ΔW_{out} at the HELIAC exit downstream the FB. By means of variable weighting factors λ_{1-18}, the cost function could be flexibly adjusted in this semi-supervised optimization approach and thus, e. g. , an unintended convergence to local side optima has been prevented.

In addition, input distributions with larger emittance were used in the design process to provide a safety buffer from the beginning, especially for the error tolerance studies.

For other mass-to-charge ratios $A/z < 6$ the basic procedure to find the optimum accelerator settings is as follows: Both the E-field of the cavities and the strength of the magnets can first be reduced linearly by the factor ${}^{A_{new}}/_{Z_{new}} \cdot {}^{1}/_{6}$, with ${}^{A_{new}}/_{Z_{new}}$ being the mass-to-charge ratio of the new particle type. Now, however, it should be noted that a lower mass-to-charge ratio leads to stronger space charge effects at constant beam current. The beam thus widens more transversely and longitudinally. The magnetic field strengths and RF phases of the cavities must therefore be slightly readjusted to compensate for this.

4.4.1.1 *Porting the Design to TraceWin*

As stated in Section 2.5.2 a particularly valuable feature of TraceWin is the possibility to perform start-to-end-simulations for an entire accelerator, from the output of the ion source up to the final beam target respectively experiment. In the future, when the RF designs of all HELIAC cavities are finalized, the use of 3D field maps for precise simulation of the electric field distribution within the cavities is recommended for a high simulation accuracy.

In a first step, it has been investigated for the HELIAC design to what extent a Thin Gap approximation already provides sufficiently accurate results, i. e. comparable with LORASR, despite the strong simplification of the gap geometry (see Section 2.5.2). Advantages of using a Thin Gap approximation are a significantly shorter simulation

```
;DRIFT    LGTH.     APRT.RADIUS
DRIFT     470.5     10
DRIFT     4.4975    10
;GAP      VOLTAGE   PHASE  APRT.RADIUS  PH. MODE
CH0: GAP  113827    -45    10           3
DRIFT     4.4975    10
DRIFT     28.7      10
DRIFT     6.6175    10
GAP       199959.8  180    10           1
DRIFT     6.6175    10
DRIFT     26        10
DRIFT     8.2       10
GAP       231118.3  0      10           1
DRIFT     8.2       10
DRIFT     23.1      10
DRIFT     9.52      10
GAP       240279    180    10           1
DRIFT     9.52      10
DRIFT     21        10
DRIFT     10.295    10
GAP       253742.3  0      10           1
DRIFT     10.295    10
```

```
GRUN  […]
      DRIFT     GAP NO.  NFREQ.  NSTRUCT.  PHI START  SYNCHR.EN.  PH.SHIFT
      47.49975  15       2       3         -45        9.7668      0.0       CH zero
```

```
VOLT
      0.113827   ,  1  ,  1  CH zero
      0.1999598  ,  1  ,  1
      0.2311183  ,  1  ,  1
      0.240279   ,  1  ,  1
      0.2537423  ,  1  ,  1
```

```
FIST
      TUBE LGTH.  GAP LGTH.  IN. DIAM.
      47.05       0.8995     2          CH zero
      2.87        1.3235     2
      2.6         1.64       2
      2.31        1.904      2
      2.1         2.059      2
```

Figure 4.17: Comparison of input files for TraceWin with Thin Gap approximation *(left)* and LORASR *(right)*, here at the excerpt example of the definition of the first 5 gaps and the corresponding electrical voltages of CH0.

time (compared to the use of field maps) and more flexibility when performing error studies. In LORASR, the real drift tube geometry consisting of drift tube lengths and gap lengths is taken into account, whereas the acceleration gaps in TraceWin – when using the Thin Gap approximation – have no longitudinal physical dimension (see Figure 4.17), so that the entire bunch transformation in the gap is performed at a single time (and not stepwise as in LORASR). As can be seen from Figure 4.18 and Figure 4.19 the TraceWin-simulated beam envelopes are in very good agreement to the ones simulated with LORASR (Figure 4.13 on p. 53).

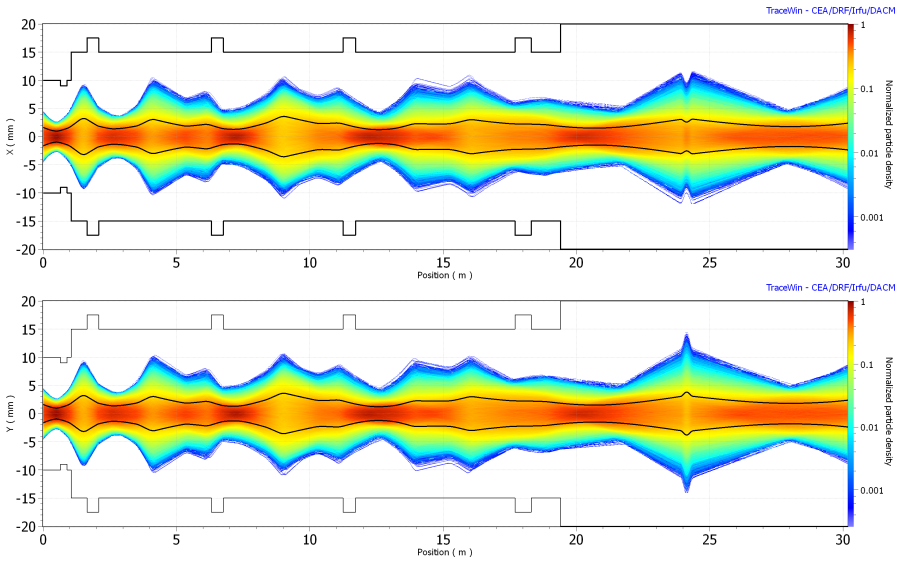

Figure 4.18: TraceWin-simulated transverse beam density along the entire HELIAC. The black curves show the rms-width.

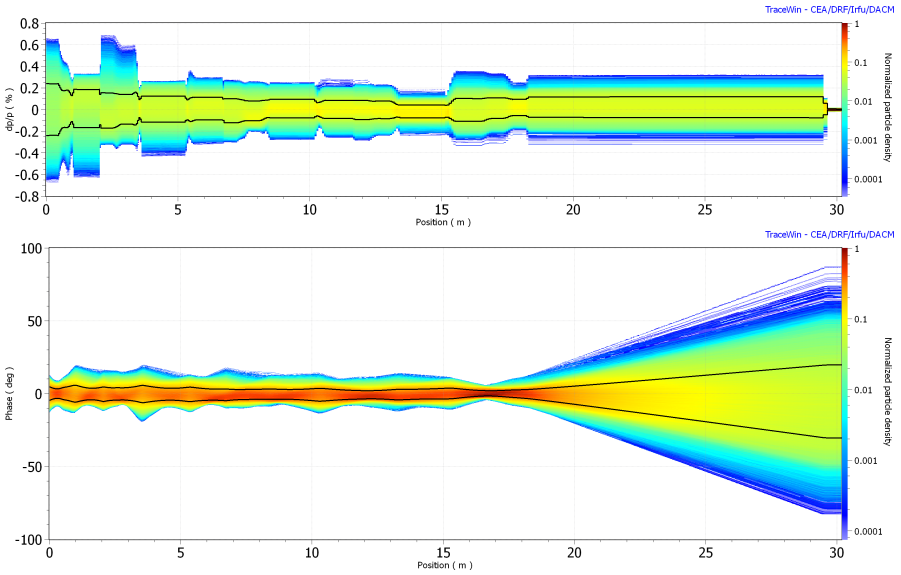

Figure 4.19: TraceWin-simulated longitudinal beam density along the entire HELIAC. The black curves show the rms-width.

The same holds true for the phase space density plots at the HELIAC exit:

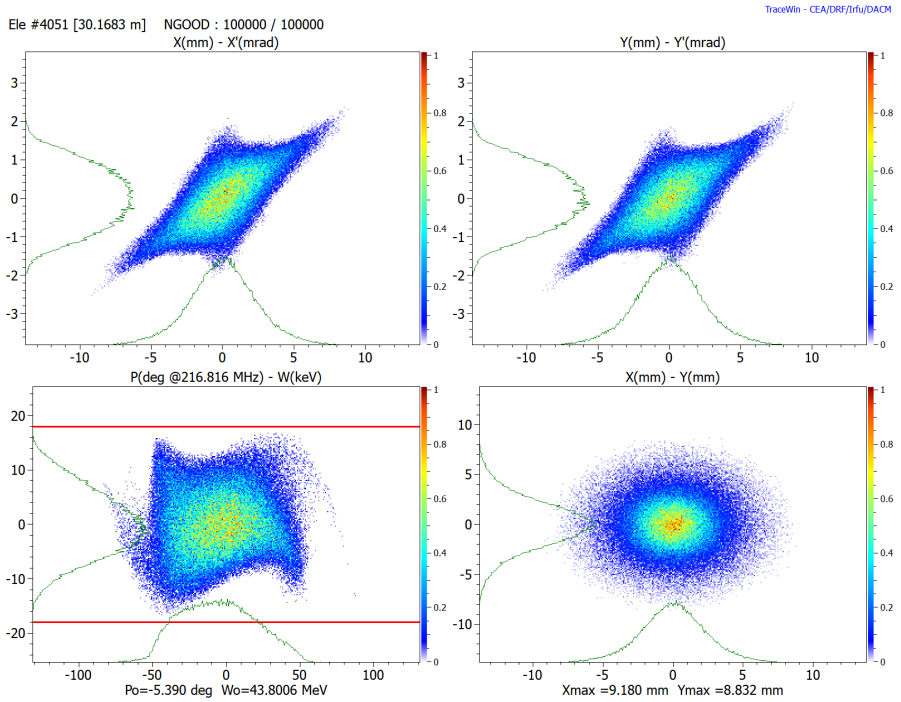

Figure 4.20: TraceWin-simulated transverse *(top)* and longitudinal *(bottom left)* phase space portraits as well as transverse beam profile *(bottom right)* at the HELIAC exit. The required output energy of $W_{\text{out}} = 7.3\,\text{MeV/u}$ ($= 43.8\,\text{MeV}$ at $A/z = 6$ assuming $z = 1$) is reached with an energy spread well inside the range of $\pm 3\,\text{keV/u}$ resp. $\pm 18\,\text{keV}$ *(bottom left, red horizontal lines)*.

As it is in LORASR, the rms-emittance growth in TraceWin is moderate with increases of +18 % (xx' and yy') and +9 % (zz'). The deviations between the two codes are therefore within the expected range, especially due to the previously mentioned deviations caused by the Thin Gap approximation. Overall, the good agreement of the LORASR simulations with the TraceWin simulations is a pleasing result, both as a confirmation of the simulation results as such, and as an outlook for a future use of TraceWin for start-to-end calculations of the entire HELIAC beam dynamics. Especially the enormously extensive features for automatic parameter optimizations, 3D field maps, error studies and correction strategies during operation can be a valuable tool for future work.

4.4.2 *Position of the Final Buncher FB*

Several positions of the final room-temperature 108.408 MHz buncher (FB) are generally conceivable. The number of possible positions is additionally increased if not only the full expansion stage with all 4 cryomodules but also the intermediate expansion stages with two and three cryomodules are taken into account assuming an already a fixed position of the buncher for all these stages.

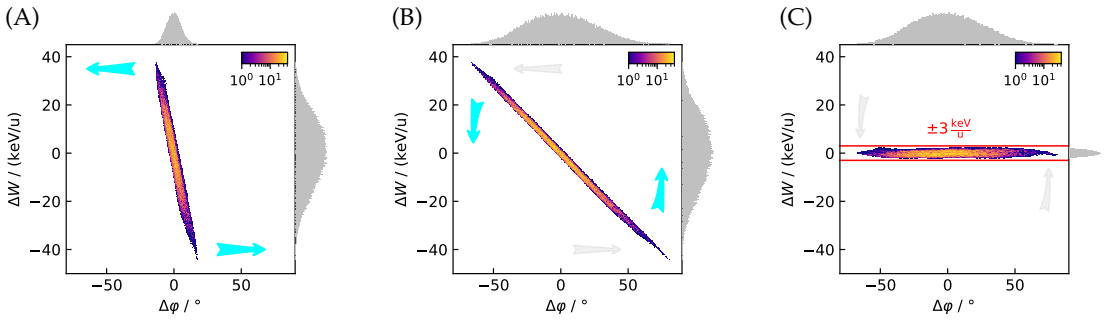

Figure 4.21: Simulated longitudinal phase space in units of 216.816 MHz at three key locations of the HELIAC design: (A) at the exit of the last CM; (B) at the injection into the FB; (C) downstream of the FB. The ultimate goal is to achieve the required energy spread of ±3 keV/u.

The general principle of the operation of the FB is depicted in Figure 4.21 at $W = 7.3$ MeV/u and described in the following:

A. At the exit of the last CM, the beam is longitudinally slightly divergent. During the subsequent beam transport over several meters, the beam drifts and the phase width thus increases *(cyan arrows)*.

B. After the drift, at the injection into the FB, the beam's phase width has reached ≈ ±80 (at 216.816 MHz). At 108.408 MHz, this corresponds to a phase width of ≈ ±40°. The approximately

linear part of the sinusoidal RF wave is now used in the final buncher to perform a shear transformation of the bunch in the longitudinal phase space. Particles with negative phase difference to the bunch center are decelerated and those with positive phase difference are accelerated *(cyan arrows)*.

c. After the transformation in the final buncher the energy spread of the particle bunch is now drastically reduced and fits into the required narrow range of $\pm 3\,\mathrm{keV/u}$ *(red horizontal lines)*.

The maximum distance between the output flange of the last CM of the superconducting part and the FB depends in particular on the longitudinal phase space distribution at the output of this CM. Depending on the phase width, energy spread and position of the beam in the phase space, the longitudinal expansion of the beam up to the position of the FB is determined. For the highest possible energy sharpness, it is advantageous if the approximately linear part of the RF curve of the FB is used to transform the beam in phase space. The phase width (with respect to 216.816 MHz) should therefore ideally not exceed the range of $\pm 120°$ at the input of the FB. This then corresponds to $\pm 60°$ at 108.408 MHz. Figure 4.22 shows the deviation of the effective voltage of this phase range from a linear curve. Considering the output energies of 3.5, 5.4 and 7.3 MeV/u for this accelerator and different initial energy widths $\Delta W/W$, Figure 4.23 presents the evolution of the phase width depending on the distance between the superconducting accelerator section and the final buncher.

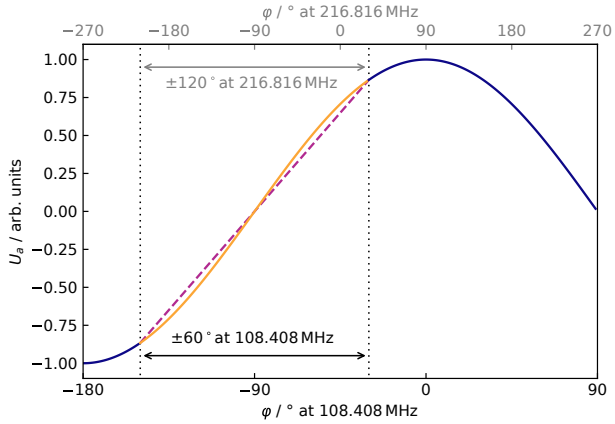

Figure 4.22: Time-dependency of the effective voltage U_a at 108.408 MHz. In the range from $-150°$ to $-30°$ the RF-amplitude *(orange)* increases approximately linear *(dashed purple line)*. According to an RF-frequency of 216.816 MHz this range equals a phase spread of $\pm 120°$ *(gray scale at the top)*.

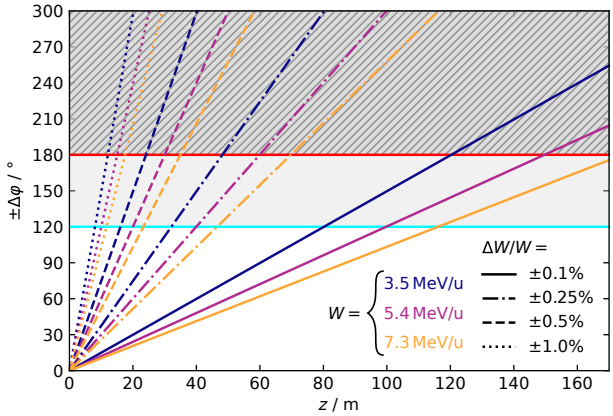

Figure 4.23: Additional phase spread $\Delta\varphi$ (in relation to 216.816 MHz) due to an initial energy spread $\Delta W/W$ for a drifting beam with energy W as function of the drift length z. A phase spread of less than $\pm 120°$ is desirable to achieve the desired energy width of ± 3 keV/u by means of a phase-energy-transformation through the final buncher. In the case of a longitudinally converging beam at the beginning, its initial phase width and movement must be considered accordingly before using this plot.

Space charge is not considered here but plays only a minor role anyway. However, this plot can be used for an initial estimate of the dimensions of the beam transport path from the superconducting part of the accelerator to the final buncher on the way to the experimental stations.

4.4.3 *Error Studies*

Error studies play a major role in the development of beam dynamics for linear accelerators. They ensure that not only ideal assumptions are made for the development of the design, but also that typically occurring deviations from parameters during production, adjustment and operation of the accelerator are taken into account. One of the objectives could be to determine "safe values" in order to define tolerance ranges in which values may lie without a significant reduction in beam quality or occurring beam losses. However, the tolerance region could also indicate the range of values within which parameters may lie in order to still be able to correct them assuming a certain diagnostic sensitivity and accuracy of diagnostic elements such as BPMs. Typical parameters of a linac design that may be subject to errors are listed in Table 4.5. The influence on the beam dynamics is very different for these types of errors. Moreover, these error types should not only be considered independently of each other, since they are partially coupled with each other so their influence may consequently increase or decrease together while effects add up or compensate each other.

In LORASR, the error nos. 1, 3 and 5–7 can be simulated [153, 154] and can generally be regarded as the most critical ones.

#	ELEMENT	ERROR TYPE
1	Magnet	transversal displacement (x/y)
2		longitudinal displacement (z)
3		rotation (yaw ϕ_x, pitch ϕ_y, roll ϕ_z)
4		strength ($^{dB}/_{B_0}$)
5	Cavity	single gap field ($^{dU}/_{U_{\text{gap}}}$)
6		cavity field ($^{dU}/_{U_{\text{cavity}}}$)
7		cavity RF phase ($d\varphi$)
8		transversal displacement (x/y)
9		longitudinal displacement (z)
10		rotation (yaw ϕ_x, pitch ϕ_y, roll ϕ_z)

Table 4.5: Overview of some typically occurring error types.

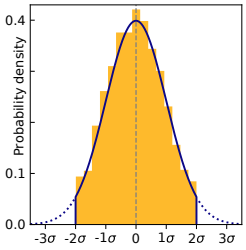

Exemplary Gaussian error distribution for 2000 *runs truncated at* $\pm 2\sigma$.

Therefore, in this study Gaussian distributed errors of the respective types are generated for many runs (typically in the order of a few 10^2 to several 10^3) and truncated at the $\pm 2\sigma$-width. Then the probability distribution of the additional rms-emittance growth for both transversal and the longitudinal plane as well as as the common maximum envelopes resulting by overlapping all runs and the positions along the beam line where beam losses are likely to happen can be plotted. This gives a good indication of the sensitivity of the beam dynamics design to the aforementioned deviations.

The error studies performed for HELIAC are presented in the following. For this purpose, 10^3 LORASR simulations were performed with 10^4 macroparticles randomly selected from the reference particle distribution of 10^5 macroparticles. In this process, all the erroneous variables were generated in a Gaussian distribution (truncated at 2σ) and imposed on the 10^3 LORASR simulations. In a final step, all error types were combined and examined together. For reasons of symmetry in the superconducting part of the linac, the transverse envelope plots are shown below for the $x(z)$-plane only.

4.4.3.1 *Errors Concerning the Cavities*

The errors related to the cavity can be divided into two groups: On the one hand, those that are primarily *static* and arise e. g. due to deviations between the assumed distribution of the total voltage of a cavity and the individual gaps. And on the other hand, those mainly caused by deviations during operation, e. g. by a not ideally adjusted phase or also generally phase and amplitude fluctuations of the LLRF system.

gap voltage variation

For the individual gap voltage variations the overall contribution to the HELIAC errors can be estimated to be small as the accuracy of RF simulations of cavities has improved significantly over the past decade due to the vast increase in computing power.

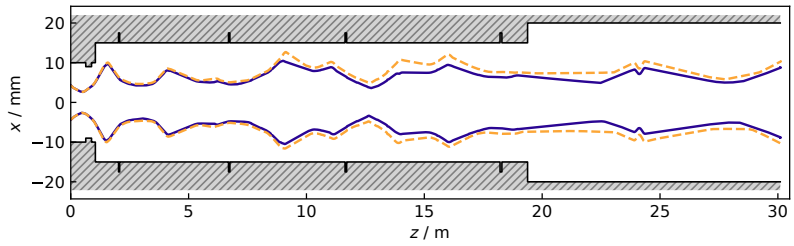

Figure 4.24: Plot of the common maximum beam envelope in x from 1000 error runs for error #5 with $2\sigma = 5\,\%$ (*dashed orange line*; nominal run 100% envelope in *dark blue*).

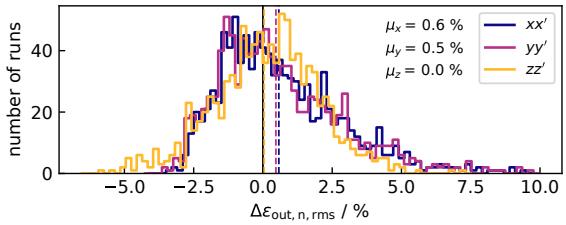

Figure 4.25: Probability distribution of the additional rms emittance growth from 1000 error runs for error #5 (gap field variation) with $2\sigma = 5\,\%$.

Moreover, even for large deviations of up to $\pm 5\%$, Figure 4.24 and Figure 4.25 still show no particle beam loss, only moderate envelope growth, and on average only a minimal increase in rms emittance growth.

cavity voltage variation

If, on the other hand, the power level of the cavities and thus their total voltages are varied, a transverse envelope broadening is already evident (here at deviations of maximum $\pm 1.5\%$, see Figure 4.26). Furthermore, there is on average a significant increase in the additional

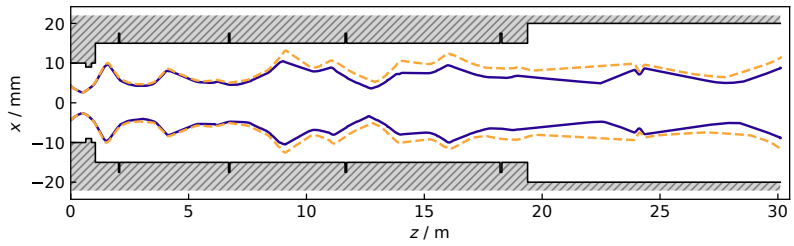

Figure 4.26: Plot of the common maximum beam envelope in x from 1000 error runs for error #6 with $2\sigma = 1.5\,\%$ (*dashed orange line*; nominal run 100% envelope in *dark blue*).

transverse rms emittance growth (Figure 4.27), with a moderately negative longitudinal rms emittance reduction. This demonstrates the strong coupling of the transverse and longitudinal planes in this design due to the fairly high aperture fill ratio (→ RF defocusing) and high acceleration gradient E_a. Nevertheless, no beam loss occurs at this error magnitude.

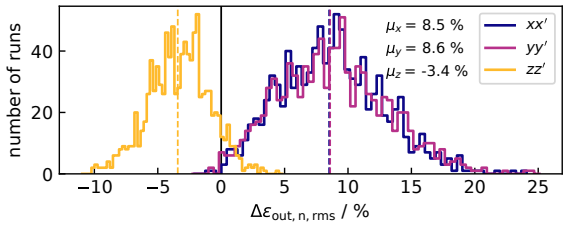

Figure 4.27: Probability distribution of the additional rms emittance growth from 1000 error runs for error #6 (cavity voltage variation) with $2\sigma = 1.5\,\%$.

cavity phase variation

The RF phase of each cavity of this design is likely the main parameter for variation during the setup of beam operation. Figure 4.28 and Figure 4.29 indicate a high stability even for RF phase errors of up to $\pm 2^\circ$. So the average additional transverse rms emittance growth remains below 1% and the average additional longitudinal rms emittance growth remains below 2%.

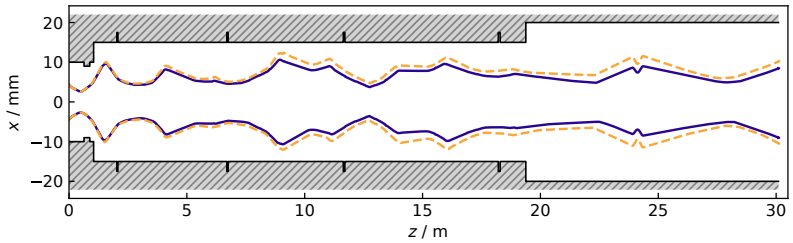

Figure 4.28: Plot of the common maximum beam envelope in x from 1000 error runs for error #7 (RF phase variation) with $2\sigma = 2^\circ$ (*dashed orange line*; nominal run 100% envelope in *dark blue*).

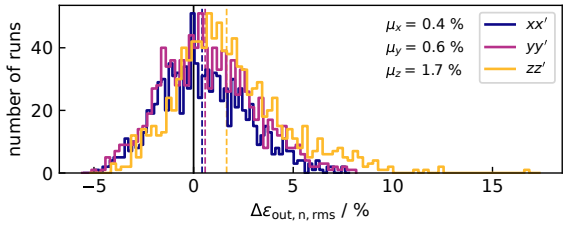

Figure 4.29: Probability distribution of the additional rms emittance growth from 1000 error runs for error #7 (RF phase variation) with $2\sigma = 2^\circ$.

4.4.3.2 *Errors Concerning the Magnets*

The magnet-related errors simulated with LORASR are the transversal displacement (error #1) and rotation of the solenoid and the entire quadrupole triplet around all axes, more specific yaw ϕ_x, pitch ϕ_y and roll ϕ_z (error #3). It should be noted here that each HELIAC solenoid is equipped with two dipole pairs for steering the beam in horizontal and vertical direction, to be able to compensate these errors.

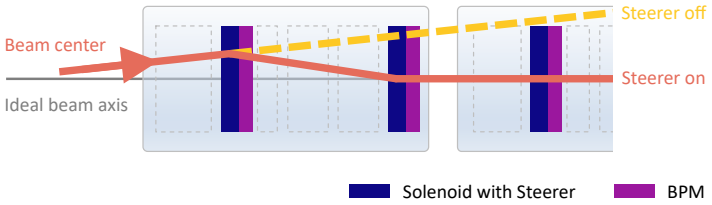

Figure 4.30: Steering correction scheme exemplified for the first solenoids in CM1 and CM2 with a beam transversely deviating from the ideal beam axis, which is detected by the BPMs.

The amplitude and risk of these errors is thus significantly reduced. Nevertheless, the influence of possible deviations will be analyzed in the following and a general steering correction strategy is presented. Figure 4.30 shows a beam transversely deviating from the ideal beam axis, first detected by the BPM on the left. The xy-steering magnets of the first solenoid are therefore set to a deflection which leads to a minimum deviation from the ideal beam axis at the second BPM. The second steerer is then used to set the beam parallel to the beam axis which can be verified by the third BPM. This is then performed both iteratively and for the other steerer-BPM combinations along the HELIAC.

Figure 4.31 illustrates exemplarily which deviations with respect to rotation (yaw and pitch) would be acceptable at solenoid 1 in order to obtain no beam losses up to the center of solenoid 2. Here it becomes clear that already at a rotation of more than 0.5 mrad[5] beam losses would occur already at the second solenoid. For the whole HELIAC (**without** steering correction) this limit is even lower, as will be shown in the following.

To evaluate how the beam evolves without any steering correction Figure 4.32 and Figure 4.33 show the corresponding beam envelopes and additional rms-emittance growth for error #3 (magnet rotation) with an error amplitude up to $2\sigma = 0.35$ mrad. For this value no particle beam losses occur in any of the 1000 simulation runs. The transversal common maximum envelope is nevertheless visibly enlarged. In case of no steering correction, a further increase of the error amplitude would thus lead to transverse particle beam losses here. At the same time, the additional rms emittance growth is shown to

magnet rotation

5 corresponding to a maximum transverse offset of the respective ends to the ideal beam axis of just ±100 µm for a solenoid length (flange-to-flange) of 40 cm.

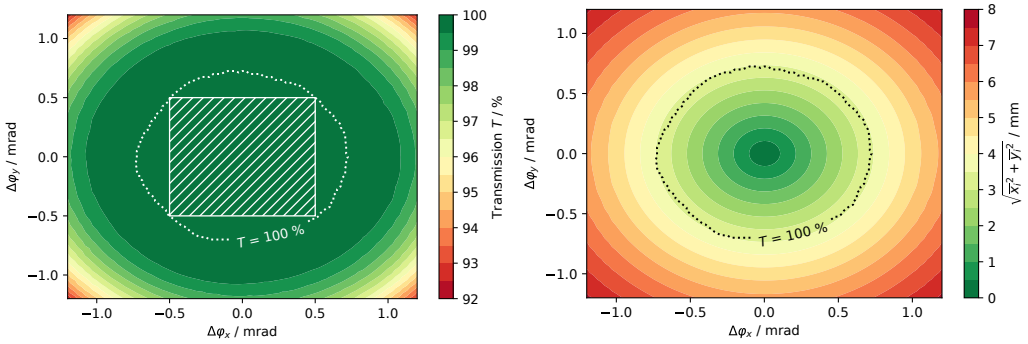

Figure 4.31: Beam transmission T at the center of the second solenoid in CM1 while varying yaw and pitch of the first solenoid *(left)*. For $\Delta\varphi_{x/y} < 0.5\,\text{mrad}$ no beam loss occurs ($T = 100\,\%$). This corresponds to a deviation of the beam center $\sqrt{\overline{x_i}^2 + \overline{y_i}^2}$ from the ideal beam axis of less than 3.5 mm *(right)*.

be small. Its mean value $\mu_{x/y/z}$ is less than 1 % in all three subphase spaces, showing the general stability of the design against this type of error.

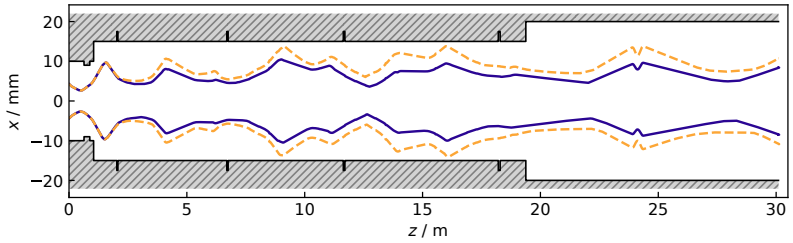

Figure 4.32: Plot of the common maximum beam envelope in x from 1000 error runs for error #3 (magnet rotation) with $2\sigma = 0.35\,\text{mrad}$ (*dashed orange line*; nominal run 100% envelope in *dark blue*).

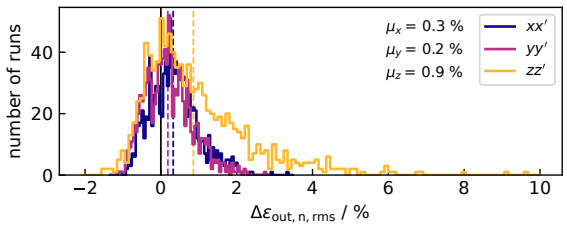

Figure 4.33: Probability distribution of the additional rms emittance growth from 1000 error runs for error #3 (magnet rotation) with $2\sigma = 0.35\,\text{mrad}$.

transverse magnet displacement

The sensitivity of the HELIAC beam dynamics design to transverse displacement of the magnets (error #1) is depicted in Figure 4.34 and Figure 4.35 for an error amplitude up to $2\sigma = 0.2\,\text{mm}$. As for the magnet rotation, the transverse displacement shows a visible enlargement of the envelopes without a significant rms-emittance

growth. Nevertheless, it can be said, since both the assumed maximum error of rotation and displacement are very small values, which are difficult to safely meet within a superconducting cryomodule, that the need for steerer magnets is clearly shown here and their use is thus strongly recommended.

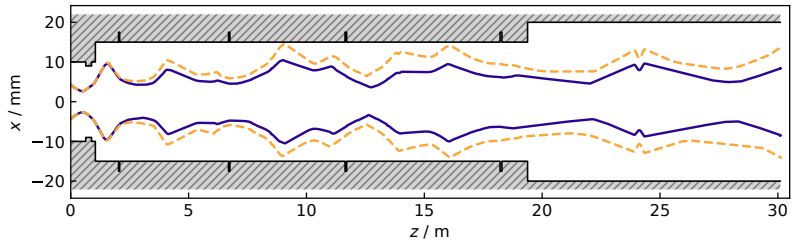

Figure 4.34: Plot of the common maximum beam envelope in x from 1000 error runs for error #1 (transverse magnet displacement) with $2\sigma = 0.2\,\text{mm}$ *(dashed orange line*; nominal run 100% envelope in *dark blue*).

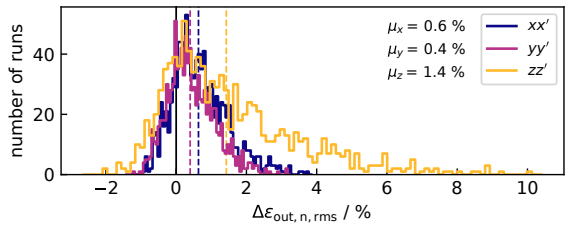

Figure 4.35: Probability distribution of the additional rms emittance growth from 1000 error runs for error #1 (transverse magnet displacement) with $2\sigma = 0.2\,\text{mm}$.

4.4.3.3 *Combined Errors*

Since the aforementioned error types realistically do not occur individually but together, it is recommended to combine these error types. This also allows a better estimation of their possible coupling. In this section, the error types will be combined and studied together with the following amplitude values (2σ) in 5000 Gaussian distributed error runs:

- magnet transversal displacement: $\pm 0.1\,\text{mm}$,
- magnet rotation: $\pm 0.1\,\text{mrad}$,
- cavity single gap voltage error: $\pm 2\,\%$,
- cavity total voltage error: $\pm 0.5\,\%$,
- cavity RF phase error: $\pm 1^\circ$.

Since errors in the solenoid magnets can be compensated by the steerer pairs present in each solenoid (see Section 4.3.1) the resulting magnet error amplitudes were estimated to relatively small values of ± 0.1 mm and ± 0.1 mrad for this study. For illustration: ± 0.1 mrad rotation corresponds to a maximum transverse offset of the respective ends to the ideal beam axis of just ± 20 µm for a solenoid length (flange-to-flange) of 40 cm. Technically, this value cannot be safely achieved in practice, which is why the correction coils are needed here in any case.

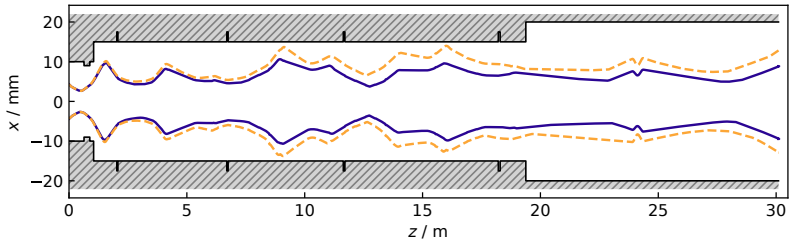

Figure 4.36: Plot of the common maximum beam envelope in x from 5000 error runs for combined errors *(dashed orange line*; nominal run 100 % envelope in *dark blue*). No beam loss occurs.

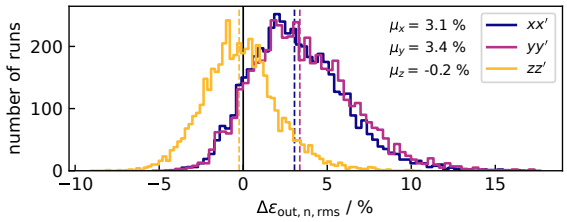

Figure 4.37: Probability distribution of the additional rms emittance growth from 5000 error runs for combined errors.

From Figure 4.37 it can be seen, that the average additional rms-emittance growth both in longitudinal (μ_z) and transversal (μ_x and μ_y) planes is low. Especially longitudinally, this indicates a good optimization and the high stability of the HELIAC design. Nevertheless, it becomes clear from Figure 4.36 that the enormously high efficiency in longitudinal acceleration, leads to a coupling with the transverse plane and additionally leaves only a limited transverse margin. It is therefore of high importance that during operation and also during the upcoming upgrades of the upstream accelerator structures (in particular RFQ and IH of the HLI) attention is paid to a compact beam with low emittance for injection into the HELIAC. For now, these studies have thus demonstrated sufficient stability of the HELIAC beam dynamics design against typically occurring errors and error amplitudes. For future investigations, it is recommended to use the even more comprehensive possibilities for error tolerance investigations of TraceWin to extend the previous results.

4.5 ENERGY-VARIABILITY

One of the challenges in the synthesis of superheavy elements is to set the energy of the primary beam (often referred to as the "projectile") hitting the target correctly. It must be large enough to exceed the Coulomb threshold of the target nucleus, but small enough so that the resulting compound nucleus remains below the fission threshold (see Section 3.2). Therefore, precise control of both the beam energy W and its energy spread $\Delta W/W$ is important. However, due to the inherent coupling of the longitudinal and the transverse phase space (see for example Section 2.2.2), this always necessarily includes an observation and, if necessary, correction of the transverse beam behavior by adjusting the solenoid field strengths. In conclusion, however, it is also preferable to set the desired beam energy using as few parameters as possible, since each additional parameter that needs to be varied makes the operation of the linac more complex and tends to make it more error-prone.

4.5.1 *Principle of Energy Variation*

Basically, energy variation at the beam exit can be achieved in two ways. Either by decelerating the beam, for example by introducing a mechanical element into the beam transport line and subsequent interaction with the incident beam. This is usually done, for example, in accelerators used in medicine for tumor irradiation [155]. The other variant is based on varying the strength of the applied electric field within the particle accelerator to lower the acceleration. This can be achieved by varying the RF phase/amplitude. This second approach to energy variation is applied in HELIAC. Figure 4.38 shows the simulated influence of a varied RF phase of one cavity. Here using the Advanced Demonstrator with its last cavity CH2 as an example. It can be seen, that the beam energy W_{out} can be reasonably and evenly varied in a range of 2.45 MeV/u to 2.7 MeV/u by *only* varying the phase $\varphi_{\text{CH2,initial}}$ from $-50°$ to $25°$ without any beam transmission degradation at the exit flange of CM1. Even though a smooth energy variation is generally possible with EQUUS just by variation of one cavities' RF phase it is obvious that for the entire HELIAC accelerator, adjusting phase *and* voltage of one cavity as well as varied buncher cavity/solenoid settings are essential to ensure high beam quality with low emittance growth and no beam losses over a large energy range.

4.5.2 *Increased Output Energy of CM1 for Different Mass-to-Charge-Ratios*

As stated in [12], the acceleration gradients in CM1, chosen below the achievable value of $E_a = 7.1\,\text{MV/m}$ for the CH cavities downstream CH2, are intended to avoid a too large beam energy gain and particle

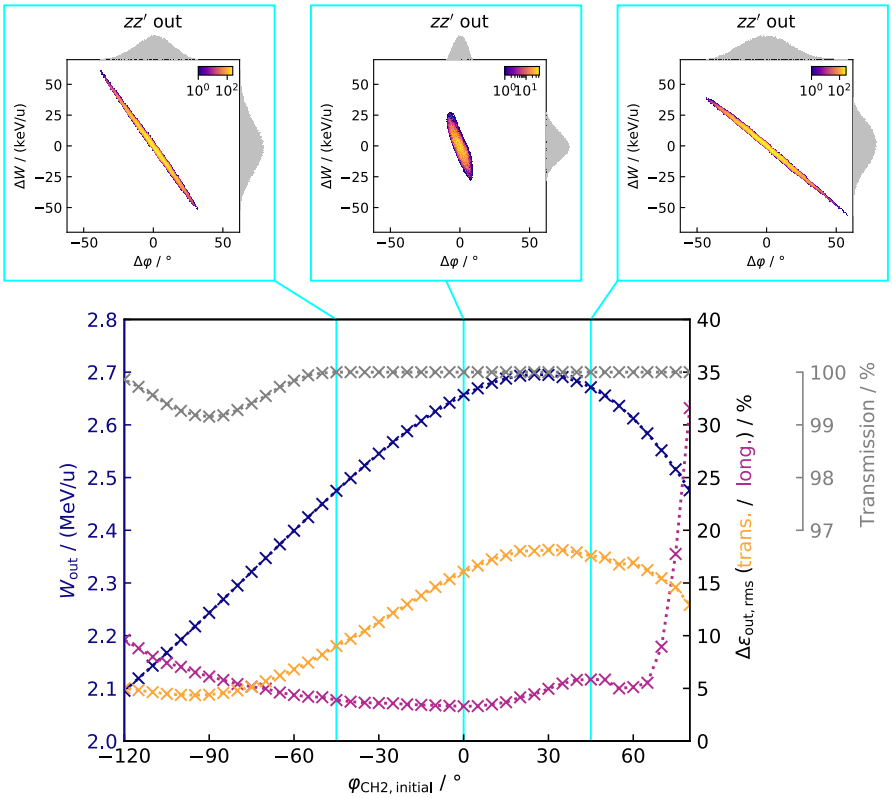

Figure 4.38: Simulated exit energy W_{out}, transverse and longitudinal emittance growth $\Delta\epsilon_{out,rms}$ and beam transmission as function of the initial reference phase of the bunch in the first gap of CH2 $\varphi_{CH2,initial}$ with CM1 only.

velocity at CH2 (originally designed for a reference relativistic β of 6.9 % of c). But even with the reduced acceleration gradients given in Table 4.4 (p. 52) the output energy at CH2 is about 20 % higher than the geometrical reference value. The simulated evolution of the mean bunch energy and reference phase along the four cavities of the Advanced Demonstrator is depicted in Figure 4.9 (p. 47). In particular, the optimized settings (RF voltage and RF phase) for all cavities lead to a progression of the reference phase along the CH2 cavity from $+7°$ at the first gap to $-61°$ at the last one.

Injecting the beam with an even higher velocity in CH2 leads to a larger shift of φ_s in each gap, possibly resulting in the longitudinal overfocusing of the beam, nonlinear deformations of the beam shape in the longitudinal phase space, a higher transverse emittance growth and even beam loss due to the increased radial RF defocusing at very negative φ_s in the last gaps. These effects could be observed clearly during beam dynamics simulations when light ions were used and acceleration gradients were pushed too high.

Nevertheless, in addition to the general beam dynamics design, HELIAC also allows acceleration of lighter ions and even protons. A corresponding set of beam dynamics simulations is shown in the fol-

lowing as an example for ions with a mass-to-charge ratio of $A/z = 3$. Apart from this value, the initial main beam parameters used at the HLI output were the same as for the design ions. The simulated phase space portraits are shown in Figure 4.39. By exhausting the maximum possible energy gain, the resulting beam energy with optimized machine settings (RF voltage and RF phase) can simply reach up to 3.3 MeV/u without particle losses but with expected compromises in beam quality.

While the Advanced Demonstrator accelerates an $A/z = 6$ beam from 1.4 MeV/u to 2.7 MeV/u, the output energy for $A/z = 3$ can therefore be increased up to 3.3 MeV/u. As such energy exceeds the reference energy (based on the geometrical beta) of the last cavity CH2 by about 50 %, this approach fully exploits the advantages of the broad energy acceptance of the EQUUS beam dynamics concept to the limit. Although, in full accordance with the discourse above, such a high energy gain, reached for the ions with $A/z = 3$, leads to a significant degradation of the beam quality, especially in the longitudinal phase plane. Therefore, this is not suitable for all applications.

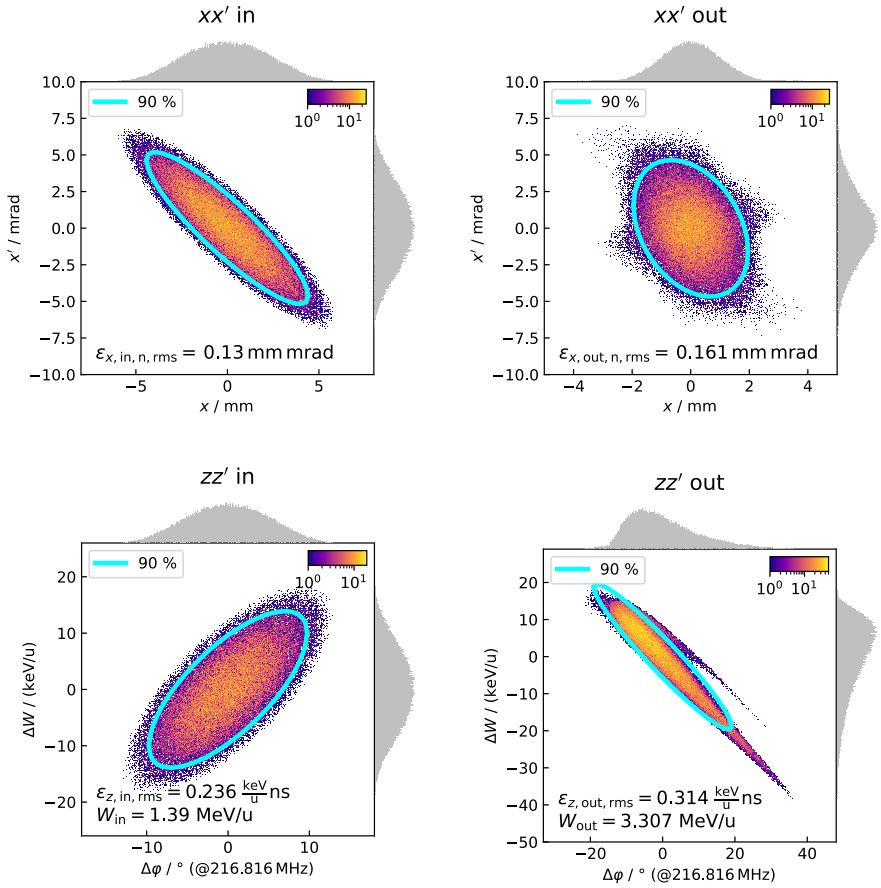

Figure 4.39: Simulated transverse and longitudinal phase space portraits for $A/z = 3$ with a ramped up output energy $W_{out} = 3.3$ MeV/u. Injection on the *left*, Accelerator output on the *right*.

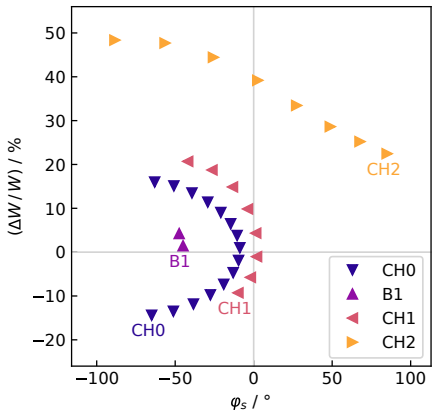

Figure 4.40: Simulated evolution of the relative mean bunch energy $\Delta W/W$ and the reference phase φ_s along cavities CH0, B1, CH1 and CH2; $A/z = 3$, ramped up output energy $W_{out} = 3.3\,\mathrm{MeV/u}$; the labels with the cavity names indicate the first gap of each cavity.

The evolution of the relative mean bunch energy and reference phase along the cavities of the Advanced Demonstrator, simulated for ions with $A/z = 3$, is shown in Figure 4.40. The considered settings (RF voltage and RF phase) for all four cavities lead to an evolution of the reference phase along the CH2 cavity from $+90°$ at the first gap to $-90°$ at the last one.

Due to the 20 % higher particle velocity at the CH2 entrance, as well as due to the resulting phase shift from gap to gap, the entire acceleration range from $\varphi_s = +90°$ to $-90°$ is exhausted resulting in a final beam energy of 3.3 MeV/u. Further increase of the input particle velocity at CH2 entrance would even lead to deceleration in some outer gaps, while acceleration in the central gaps, with reference phase close to $0°$, reaches already its maximum. Therefore, these machine settings represent the upper threshold for effective and stable beam acceleration. These extreme beam dynamic settings are therefore not unreservedly recommended in this drastic form for regular use, but nevertheless demonstrate the enormous potential of EQUUS beam dynamics and can certainly be used for special beam requirements. The total energy gain of the beam in the Advanced Demonstrator for ions with a mass-to-charge ratio $A/z = 3$ can be increased in this way up to 50 % compared to the cavity reference value. The accelerating gaps in the cavities CH0, CH1 and B1 are mainly operated in a negative range of the reference phase, ensuring longitudinal beam focusing. The operation of the first CH2 gaps with a strongly positive reference phase lead to a degradation of the beam quality, in particular in the longitudinal phase plane. Nevertheless, the rms emittance growths are sufficiently low, especially given these extreme settings: 32 % for the transverse xx' and yy' phase planes and 47 % for the longitudinal zz' one. The particle transmission remains entirely at 100 %. Therefore,

it can be summarized that the beam dynamics layout of the Advanced Demonstrator provides efficient acceleration in a wide range of beam energies and keeps the beam quality consistently within acceptable limits.

4.5.3 3.5 *to* 7.3 MeV/u

Classical energy-variable accelerators are synchrotrons, cyclotrons and independent-cavity ion linacs consisting of an array of short cavities, each with a broad velocity acceptance profile and with independent settings for the phases and amplitudes. As for the latter, according to Wangler (2008) *"such a linac is capable of flexible operation, including energy variability, **which is not available in long multicell ion linacs**, whose transit-time-factor velocity profiles are very narrow, requiring operation only for a unique velocity profile."* [29, chap. 6.9, emphasis added]

HELIAC and its beam dynamics concept EQUUS were therefore specifically designed to provide the required energy variability **and** to combine it with the advantages of efficient multigap structures. By reducing the RF power until it is completely switched off starting at the last CH cavity and then incrementally also for the CH cavities upstream, the output energy of the linac can be reduced smoothly. By varying the RF phase at the same time, the beam quality can be largely maintained. In the case of a switched-off cavity, the resonance frequency should be detuned by using the available mechanical tuners [33, 156, 157] to avoid unwanted excitation of the cavity by the beam. This could otherwise in turn interfere with the beam.

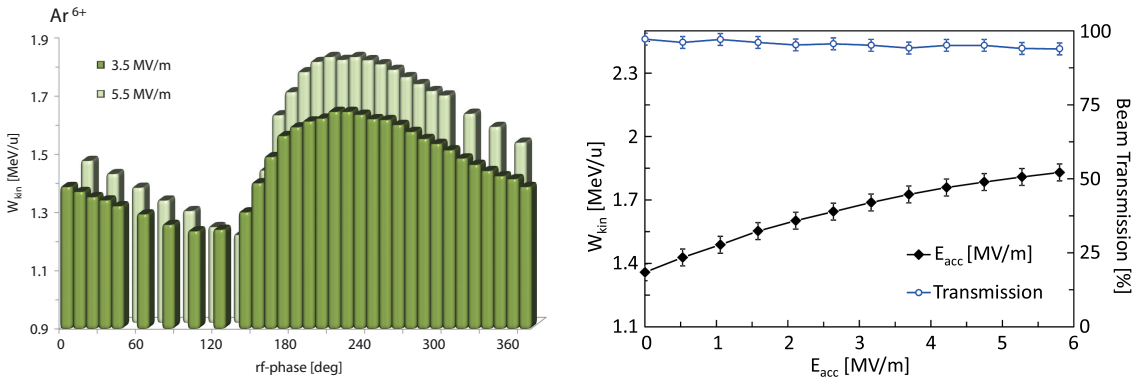

Figure 4.41: First heavy ion beam tests with CH0. Phase scan of Ar^{6+}-beam energy for 3.5 and 5.5 MV/m *(left)*. Amplitude scan at an RF phase of 210° *(right)*. [8]

Figure 4.41 shows two plots of the first heavy ion beam tests with CH0 with an Ar^{6+} beam ($A/z = 6.7$). The figure depicts a fully measured 360° phase scan for two different acceleration gradients E_a. It can be seen, that around an RF phase of 210° the output energy W_{kin} reaches its maximum. By changing the RF phase, the output energy can be varied well. It also emerges that within a wide range

Note: Here, the value of the RF phase refers to that of the power supply, not the synchronous phase within the cavity.

of acceleration gradients the beam energy can be varied smoothly. By adjusting the focusing strengths of the magnets used, no beam transmission degradation has been observed for the full range of RF amplitudes. [8]

For the entire HELIAC layout, the following can be seen from the simulations: Figure 4.42 and Figure 4.43 show the influence on the beam downstream HELIAC's final buncher FB when *only* the total voltage or the RF phase of CH11 is varied. This confirms that smooth energy variation is generally possible just by varying RF phase *or* amplitude of a cavity, which has also been demonstrated during creation of this thesis by the aforementioned beam tests with CH0.

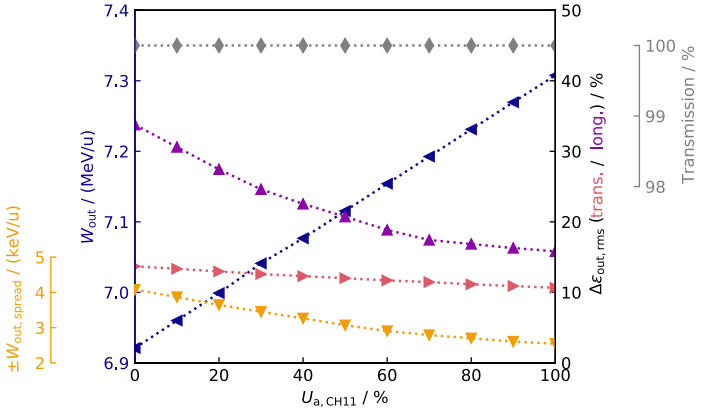

Figure 4.42: Effect of different reduced effective cavity voltages of CH11 on the final beam energy, energy spread, transverse and longitudinal emittance growth as well as beam transmission.

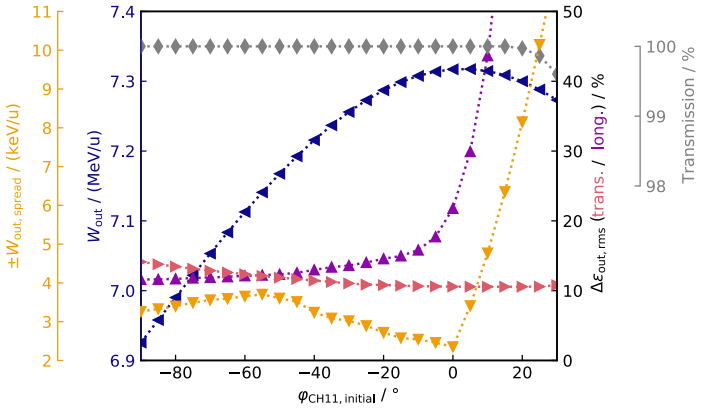

Figure 4.43: Effect of varying initial cavity phases of CH11 on the final beam energy, energy spread, transverse and longitudinal emittance growth as well as beam transmission.

Nevertheless, it is obvious that for the entire HELIAC accelerator, adjusting phase *and* voltage of one cavity as well as readjusting the buncher cavity/solenoid nearby is useful to ensure a high beam

quality with low emittance growth over the entire energy range. By following this approach, Figure 4.44 depicts the longitudinal phase space distribution for various energies in the required energy range from 3.5 to 7.3 MeV/u. For a full set of cavity and magnet settings (as function of all required beam output energies, mass-to-charge ratios and beam currents) simulations with a supervised automatic optimization approach are recommended to support the accelerator operators. Modern approaches via methods such as particle swarm optimization or genetic/evolutionary algorithms are recommended here due to their high efficiency. For other mass-to-charge ratios $A/z < 6$ the basic procedure is to scale the magnetic flux density and cavity voltages to a ratio of $A/z \cdot 1/6$. Depending on the beam current and therefore transverse beam trajectory the solenoid fields may then need to be slightly readjusted. The accelerator operators should then have an appropriate set of parameters for all modes of accelerator operation. In this context, automatic optimization routines are a useful tool, as mentioned before.

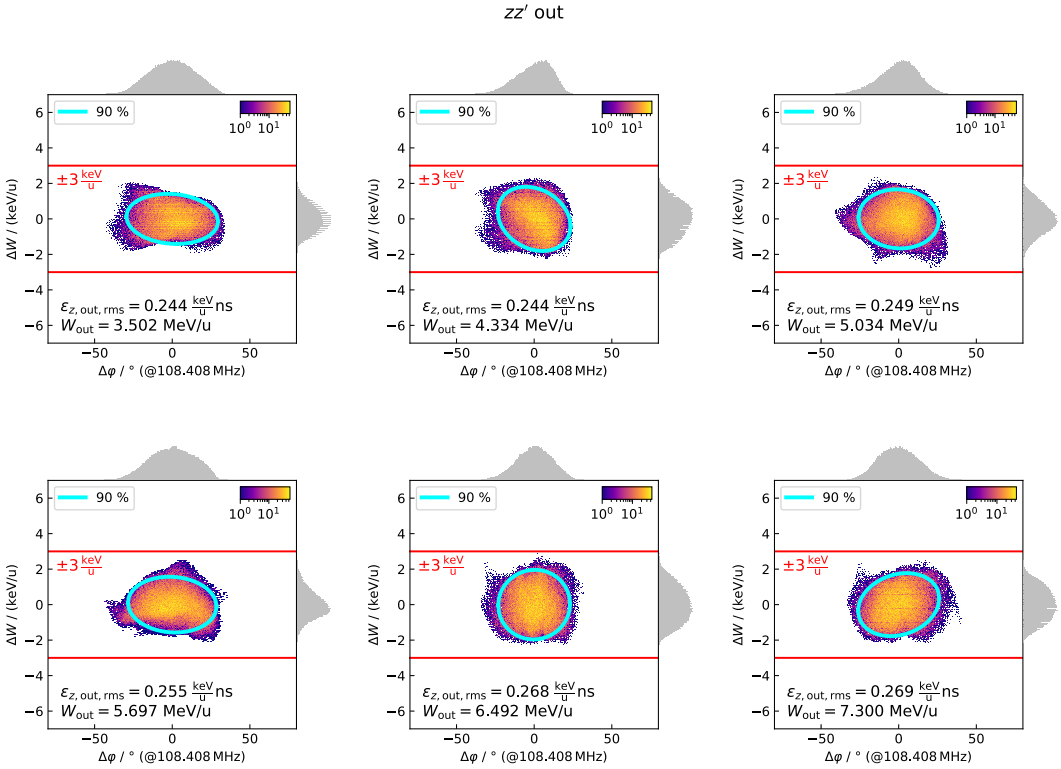

Figure 4.44: Particle density in the longitudinal phase space given for various energies in the required energy range from 3.5 to 7.3 MeV/u.

5

CONCLUSION AND OUTLOOK

This dissertation describes the development of the beam dynamics design of a novel superconducting linear accelerator. It features a main operating frequency of 216.816 MHz for the acceleration of ions with a mass-to-charge ratio of up to 6 at high duty cycles up to CW operation at the GSI Helmholtz Centre for Heavy Ion Research in Darmstadt, Germany. The focus of this work was the beam dynamics design of the accelerator section downstream the high charge injector (HLI) from an energy of 1.39 MeV/u up to the maximum output energy of 7.3 MeV/u, which corresponds to about 12.4 % speed of light. A key feature of this linac, which is designed for a maximum beam current of 1 mA is the use of the EQUUS (Equidistant Multigap Structure) beam dynamics concept. This leads to an adjustable output energy between 3.5 and 7.3 MeV/u with a required narrow energy width of at most ± 3 keV/u over the entire output energy range.

Fundamental to the remarkable advances in the study of superheavy elements in the last decades have been continuous advancements and technical innovations. On the one hand, in the field of experimental sensitivity and detection of nuclear reaction products and, on the other hand, in the field of accelerator technology.

For the acceleration of the projectile beam, the UNILAC (*Universal Linear Accelerator*), which was put into operation in 1975, has been used at GSI until 1990. From 1991, the new 1.4 MeV/u-injector allowed a significant improvement in beam quality and intensity for SHE-production. As part of the reconstruction and expansion of the research infrastructure at GSI for the future FAIR facility, a dedicated new particle accelerator, HELIAC (*Helmholtz Linear Accelerator*), is now under development to address the special beam parameter requirements for the synthesis of new superheavy elements. Typically, production rates of superheavy elements with effective cross sections in the picobarn range are very low. Therefore, a high duty cycle up to CW operation is a key feature of HELIAC. Thus, the required beam time for the desired nuclear reactions can be significantly reduced.

First considerations for a dedicated linac for research on SHE at GSI were discussed internationally in workshops in the early 2000s. 2009 Minaev *et al.* published a first preliminary draft for the beam dynamics design of a corresponding linac. This should be superconducting to enable high acceleration gradients combined with a high duty cycle.

Nevertheless, the main focus of that research work was on the analysis and theoretical description of the EQUUS beam dynamics concept, as well as the rudimentary investigation of whether this concept could in principle be considered for such an accelerator. The resulting conclusion was very optimistic about the basic applicability of this novel concept, so it was also chosen for the work done within this thesis. However, as the research focus was set on the theoretical investigation of EQUUS, many of the assumptions made for the preliminary proof-of-principle beam dynamics design were actually very simplified. As a result, while retaining the basic EQUUS concept, the beam dynamics design had to be created from scratch in this thesis. Subsequently, in the past decade, the research and development of superconducting accelerator cavities has provided many insights. Thus, several prototypes for superconducting CH-DTLs have been successfully developed and tested at IAP. In this context, worldwide top values for acceleration efficiency in the low- and medium-energy range were established several times. Further developments were made in particular with respect to the resonator geometry with emphasis on a compact design, effective frequency tuning, cavity preparation and in the design of power couplers for beam operation. Thus, ultimately, the preliminary work of Minaev *et al.* and the newly created knowledge of design, fabrication, and operation of superconducting drift-tube cavities laid the foundation for this work and thus the development of the HELIAC linear accelerator.

The GSI superconducting injector HLI serves as the injector for HELIAC. This is currently being upgraded to meet future requirements and will receive a new ECR ion source, CW-capable RFQ, and IH-DTL with an RF operating frequency of 108.408 MHz. HELIAC consists of a superconducting and a normal conducting part. Acceleration takes place in the superconducting part after a frequency jump to 216.816 MHz in four cryomodules, each about 5 m long. These contain three CH cavities, one single-spoke type buncher cavity, two solenoid magnets for transverse beam focusing, and two beam position monitors each.

The next section is an approximately 10 m long normal conducting part which is primarily used for beam transport and terminates with a final buncher cavity. This is operated at a halved frequency of 108.408 MHz to benefit from the quasi-linear part of the RF edge extended by the frequency halving. This creates greater flexibility in transforming the beam in longitudinal phase space for the required narrow energy width.

In 2016, F. Dziuba *et al.* successfully performed cold tests on a 15-gap CH structure developed at IAP, followed 2018 by the world's first beam operation of a multi-gap superconducting drift tube cavity using

the same cavity by W. Barth *et al.* at GSI, making this CH structure the first of 12 CH cavities to be used for HELIAC.

A key feature of this accelerator design is the variability of the exit energy from 3.5 to 7.3 MeV/u with a low energy spread of at most ± 3 keV/u over the entire energy range. This is a direct implication of the experimental boundary conditions for superheavy element fusion to be able to slide precisely over the Coulomb threshold with the projectile beam. Typically, the energy variation along the acceleration path is realized by using many short cavities with as few acceleration gaps as possible. Thus, the energy acceptance of each cavity is relatively large, many RF amplitudes and phases can be individually controlled, and the beam dynamics design is straightforward. Acceleration efficiency, on the other hand, is low for this method because a large number of cavities is also accompanied by many drift sections where the beam is not accelerated.

For the beam dynamics design of HELIAC, the advantages of conventional linac concepts were combined with the high acceleration gradient of superconducting CH-DTLs. The design and simulation of the beam dynamics was performed with the simulation code LORASR, which is under continuous development at IAP. The frequency jump to 216.816 MHz in the superconducting section and the use of CH cavities with 5 (CH10 and CH11) to 15 (CH0) gaps at a maximum acceleration gradient of 7.1 MV/m enable an acceleration efficiency with superconducting drift tube structures that is unique in the world so far. At the same time, with compact CH cavity lengths of 59–81 cm, a good handling for both fabrication and operation is enabled. With the sliding motion of the synchronous phase within each CH cavity, the used EQUUS beam dynamics concept leads to longitudinal beam stability in all energy ranges of the accelerator. The rms emittance growth is moderate in all three planes at $+10\,\%$ (xx'), $+11\,\%$ (yy') and $+14\,\%$ (zz'). The modular design of the HELIAC with 4 cryomodules basically allows the accelerator to be put into operation starting with the first cryomodule, the so-called Advanced Demonstrator. In this thesis, the associated beam dynamics have been investigated. In the next stage, with only the first two cryomodules of HELIAC, the lower limit of the energy range to be provided by HELIAC (3.5 MeV/u) can already be exceeded, so that the use in regular beam operation at GSI is already conceivable from here on.

By means of error studies, the stability of the HELIAC beam dynamics design against possible alignment errors of the magnetic focusing elements and RF cavities as well as errors of the electric field amplitudes and phases have been investigated and critical parameters were determined. An additional steering concept via dipole correction coils at the solenoid magnets allows a transverse beam control as well as diagnosis by means of two BPMs per cryomodule. Thus, in the end,

sufficient stability against expected deviations was shown when considering single as well as combined defect types. By means of a second simulation code (TraceWin), the entire HELIAC beam dynamics was also reproduced and basically confirmed in all essential points.

In parallel to the research on the beam dynamics design of HELIAC, the Java-based computer program LINAC-Multitool was developed as a tool to automate and simplify R&D routine tasks in accelerator physics. For example, bead-pull measurements as an important step in the factory acceptance of manufactured cavities, can now be efficiently evaluated via a graphical user interface. The design process with the beam dynamics code LORASR is also now much more convenient thanks to a comprehensive expansion of the plot functionalities via the LINAC-Multitool.

Possible remaining research topics following the extensive design work in this thesis can be summarized as follows:

- The new 1.4 MeV/u injector (HLI upgrade) at GSI is currently under development. Its high beam quality is essential for reliable operation of the HELIAC. Therefore, in the course of future R&D work, the beam dynamics acceptance of the HELIAC, also depending on the requirements of the subsequent beam transport sections, should be determined and reflected in the design of the injector.
- Setting the desired RF phase for each cavity is challenging due to the limited beam diagnostic elements available. Detailed strategies should therefore be elaborated for this purpose.
- A complete set of cavity and magnet settings (as function of all required beam output energies, mass-to-charge ratios and beam currents) will be needed for all modes of beam operation. Modern methods such as particle swarm optimization or genetic/evolutionary algorithms are recommended here for creating this parameter set due to their high efficiency.
- The various possibilities for beam transport from the HELIAC to the experiments also offer an interesting field of research. Here, in particular, with regard to the preservation of the beam quality or also the potential use of components for emittance reduction such as beam scrapers or dipole magnet chicanes.

With the completion of this thesis in summer 2021, the CH1 and CH2 cavities have already been built and are in the final preparation and cold test phase. In parallel, the development of the cavities CH3–11 was also started. The success of this beam dynamics design ultimately depends in particular on the performance of the cavities. Reliably achieving the high acceleration gradients in the CH cavities is the

most important key to this ambitious project. Given the great progress in this research area in the last decade, this is certainly a challenging but achievable accelerator project. In this respect, the development of an efficient superconducting linear accelerator with variable output energy and high duty cycle described in this thesis is also of interest for the design of future comparable ion beam accelerator facilities.

Part III

APPENDIX

A

LINAC-MULTITOOL

A.1 INTRODUCTION

Within the research for this thesis a Java-based computer program was developed [158] together with D. Bade [159] and J. Corbet [160]. Further temporary development support was provided from September to December 2019 by I. Skudnova from Saint Petersburg State University, Faculty of Applied Mathematics and Control Processes. The main objective of the LINAC-Multitool was on one hand the production of a tool to automate routine tasks within the framework of our R&D work on particle accelerators and thus make them simpler and more efficient. On the other hand, the goal was to create additional extensive plotting functionalities for frequently used programs (here especially LORASR). Currently, the software is in the beta stage, i.e. most of the features planned so far have been implemented including the GUI, most of them already functional. Several bugs are already known and can be fixed in a timely manner. A preliminary version of the user manual exists. Nevertheless, the program is already functional with limitations and can be used productively. It has also been used frequently in the context of this doctoral thesis and further ongoing accelerator projects at IAP.

Software Architecture

Three main requirements were decisive during the development of the LINAC-Multitool and in choosing an appropriate platform (i.e. programming language)

- Ease of use,
- good maintainability and
- available expandability.

In conclusion the LINAC-Multitool was developed as a Java-based program with graphical user interface (GUI) based on the toolkit JavaFX[1]. Due to the Java-inherent platform independence, it can be run on all common operating systems (Windows, MacOS and Linux). JFreeChart[2] is used as plotting framework respectively chart library.

The features of the LINAC-Multitool can be divided into four parts:

1 https://openjfx.io/
2 http://jfree.org/jfreechart/

- LORASR Toolbox
- Bead Pull Measurement Analysis
- Particle Distribution Toolbox
- CST Field Map Converter

A.2 LORASR

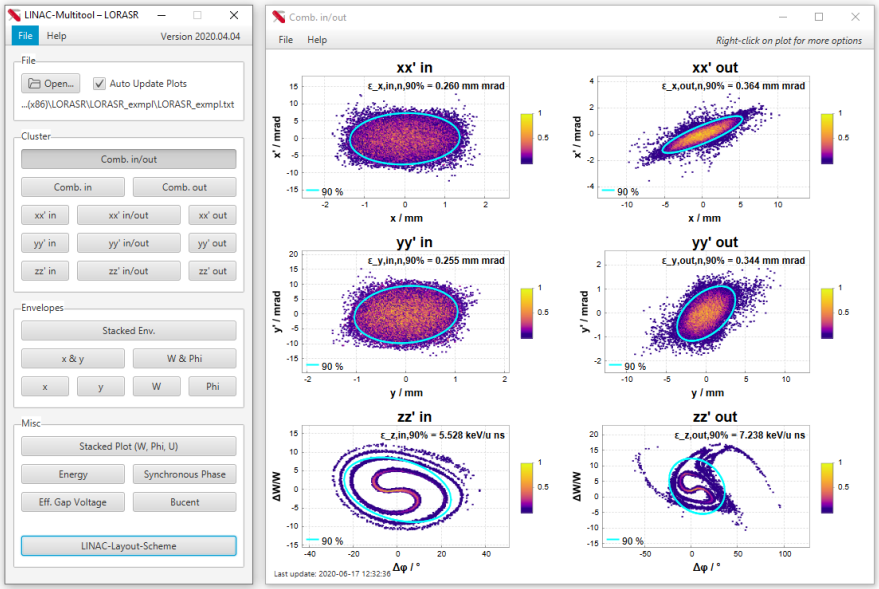

Figure A.1: LINAC-Multitool's visualization of LORASR input and output particle distributions.

An introductory overview of LORASR is given in chapter 2.5.1. As its first code version was already developed in the late 80s, the possibilities for graphical user interactions were and are still not very wide-ranging. Nevertheless, the code has been significantly improved in the past decades with a better gap field representation, a PIC space charge routine, error study tools and more [161] so it is still an important and powerful design tool (see p. 20). For optimization of the workflow in daily routines, the LINAC-Multitool offers users not only many of the plotting functionalities as already given by LORASR, but extends it by features like export of vector graphics, color-coded density plots of phase space distributions (Figure A.1), a schematic of the designed linac layout geometry, stacked plots and additional plots like energy, synchronous phase and gap voltage as function of the z-position or gap index (Figure A.2 and Figure A.3). All this in a modern and user-friendly graphical user interface, which in contrast to LORASR, for example, also allows interactive operation like zooming in and out of plots.

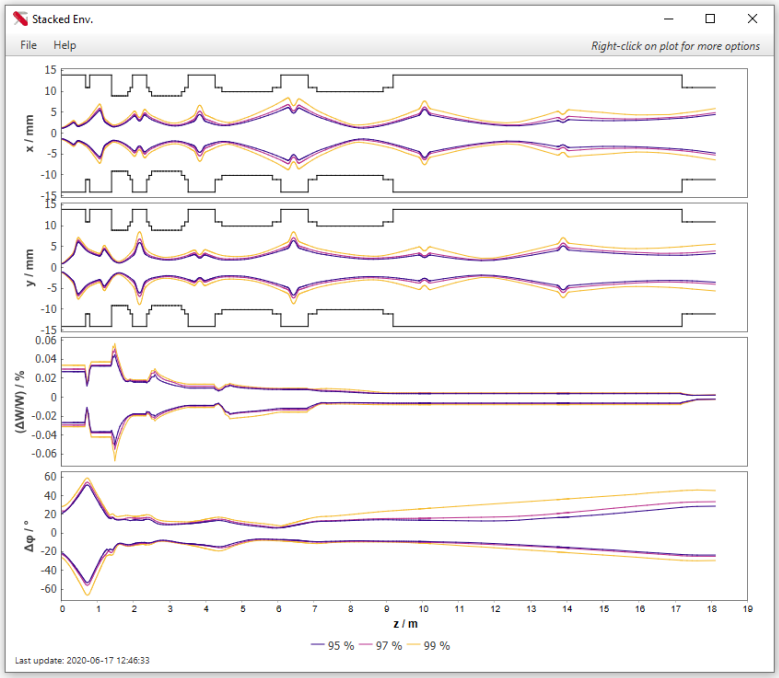

Figure A.2: LINAC-Multitool's visualization of LORASR beam envelopes.

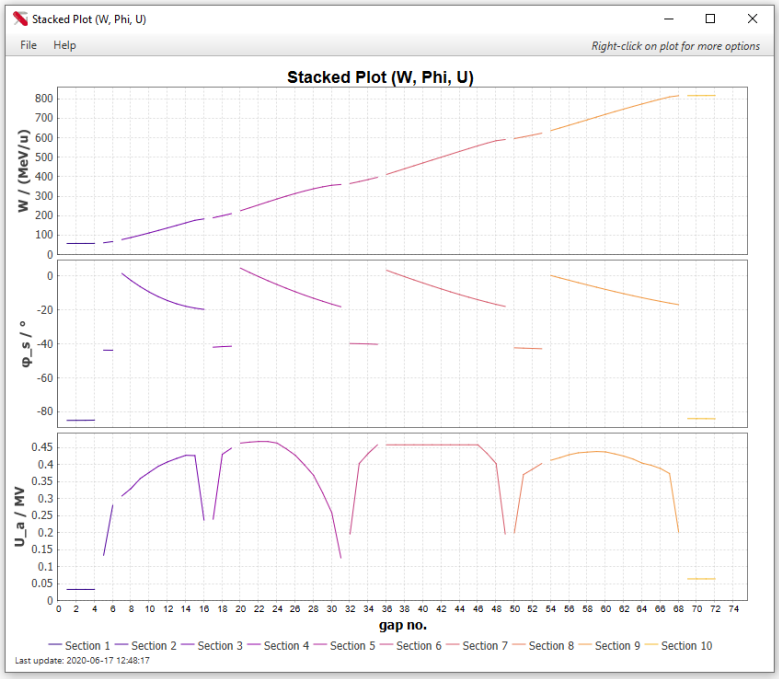

Figure A.3: LINAC-Multitool's visualization of a LORASR simulation with energy gain, synchronous phase and effective voltage per accelerating gap.

A.3 BEAD PULL MEASUREMENT

A bead-pull measurement is often performed after cavity manufacturing to check geometric and RF characteristics by placing a small dielectric or metallic bead inside the cavity. By pulling it with an electrically non-conducting wire (e. g. made of polyamide resp. nylon) through the cavity, one can measure the electromagnetic fields distribution along this path on resonance inside. To speed up the analysis of bead-pull measurements, data processing steps can be performed manually and automatically with the LINAC-Multitool (Figure A.4). These involve among others:

- Trimming/flipping/shifting/rescaling of the dataset,
- smoothing the measurement by a simple and weighted moving average with adjustable window size,
- classification of noise at the start and end of a measurement as well as baseline correction with multiple support points that can be set automatically and manually,
- plotting the absolute value of the relative E-field distribution $|E(z)|$ (obtained by the measured phase shift $\Delta\varphi_{S21}$),
- identification of individual gaps and calculation of the relative voltage distribution inside the cavity,
- comparison between multiple measurements and/or imported simulation data,
- extensive data and graphic visualization and export functionalities to pixel- (jpg, png) and vector-graphics (pdf, svg).

A.4 FIELDMAPS

This subprogram is to improve the simulation accuracy in TraceWin by a reasonably realistic assumption of the electromagnetic fields inside a cavity. These data, gained by simulations of CST EM STUDIO or CST MICROWAVE STUDIO [162], can be used in TraceWin as 3D field maps $E(x, y, z)$ (see pp. 22 ff.) after data format conversion with the LINAC-Multitool. Furthermore, the conversion of the LORASR-generated $E_z(z)$ file for the use in TraceWin could be a possible feature in the future.

A.5 PARTICLE DISTRIBUTIONS

For the conversion of particle distribution files for different simulation codes (LORASR, TraceWin, PARMTEQ(M)) this subprogram can be used (Figure A.5).

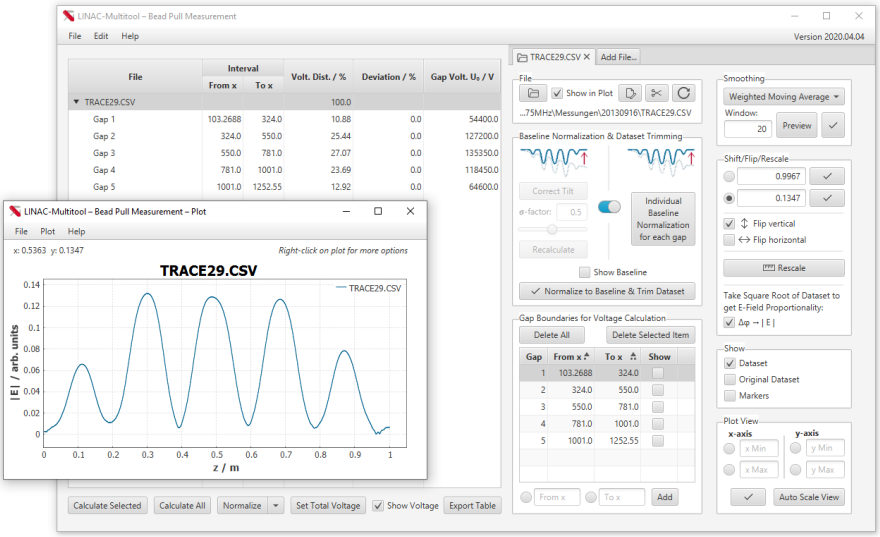

Figure A.4: Screenshot of an exemplary bead pull measurement evaluation of a 5-gap DTL-cavity with the LINAC-Multitool.

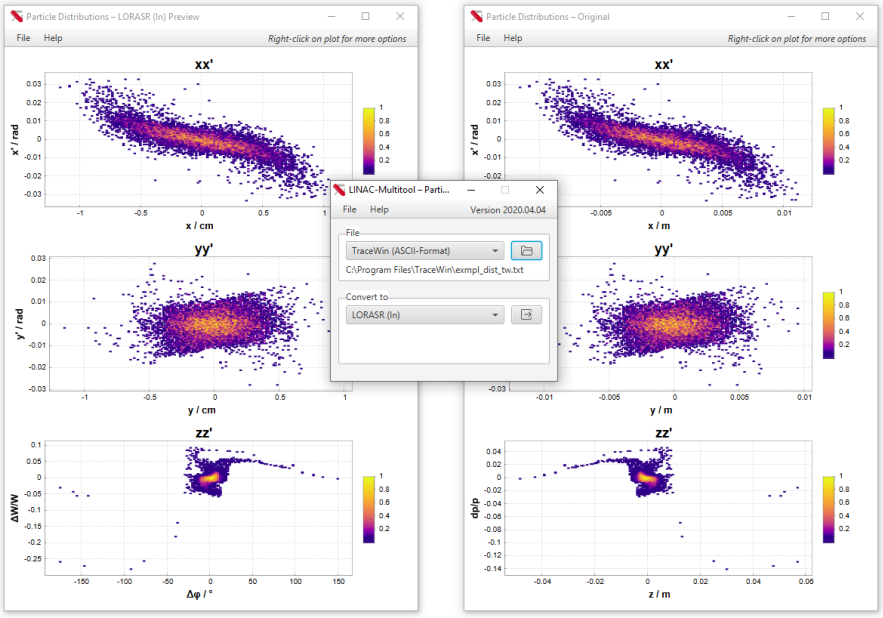

Figure A.5: Screenshot of an exemplary converted particle distribution, with the visualized original dataset in a TraceWin-format (*left*) and the converted one for LORASR (*right*).

BIBLIOGRAPHY

[1] S. A. Giuliani, Z. Matheson, W. Nazarewicz, E. Olsen, P.-G. Reinhard, J. Sadhukhan, B. Schuetrumpf, N. Schunck, and P. Schwerdtfeger. "Colloquium: Superheavy elements: Oganesson and beyond." In: *Rev. Mod. Phys.* 91 (1 Jan. 2019), p. 011001. DOI: 10.1103/RevModPhys.91.011001. URL: https://link.aps.org/doi/10.1103/RevModPhys.91.011001 (cit. on pp. 1, 25).

[2] J. Khuyagbaatar et al. "Search for elements 119 and 120." In: *Phys. Rev. C* 102 (6 2020), p. 064602. DOI: 10.1103/PhysRevC.102.064602. URL: https://link.aps.org/doi/10.1103/PhysRevC.102.064602 (cit. on p. 1).

[3] H. Kragh. "The search for superheavy elements: Historical and philosophical perspectives." In: (Aug. 14, 2017). arXiv: 1708.04064v1 [physics.hist-ph] (cit. on pp. 1, 26).

[4] Yu. Ts. Oganessian et al. "Synthesis of the isotopes of elements 118 and 116 in the ^{249}Cf and ^{245}Cm $+^{48}$ Ca fusion reactions." In: *Phys. Rev. C* 74 (4 2006), p. 044602. DOI: 10.1103/PhysRevC.74.044602. URL: https://link.aps.org/doi/10.1103/PhysRevC.74.044602 (cit. on pp. 1, 27).

[5] M. Block et al. "Direct mass measurements above uranium bridge the gap to the island of stability." In: *Nature* 463.7282 (2010), pp. 785–788. DOI: 10.1038/nature08774 (cit. on p. 1).

[6] J. H. Hamilton, S. Hofmann, and Yu. Ts. Oganessian. "Search for superheavy nuclei." In: *Annual Review of Nuclear and Particle Science* 63 (2013), pp. 383–405. DOI: 10.1146/annurev-nucl-102912-144535 (cit. on pp. 1, 28, 29).

[7] J. Khuyagbaatar et al. "^{48}Ca $+$ ^{249}Bk Fusion Reaction Leading to Element $Z = 117$: Long-Lived α-Decaying ^{270}Db and Discovery of ^{266}Lr." In: *Physical Review Letters* 112.17 (2014). DOI: 10.1103/physrevlett.112.172501 (cit. on p. 1).

[8] W. Barth et al. "First heavy ion beam tests with a superconducting multigap CH cavity." In: *Physical Review Accelerators and Beams* 21.2 (2018). DOI: 10.1103/physrevaccelbeams.21.020102 (cit. on pp. 1, 2, 31, 41, 42, 73, 74).

[9] W. Barth et al. "Superconducting CH-cavity heavy ion beam testing at GSI." In: *J. Phys. Conf. Ser.* 1067.5 (2018), p. 052007. ISSN: 1742-6588. DOI: 10.1088/1742-6596/1067/5/052007 (cit. on p. 1).

[10] S. Yaramyshev et al. "Advanced Approach for Beam Matching along the Multi-Cavity SC CW Linac at GSI." In: *Journal of Physics: Conference Series* 1067 (2018), p. 052005. DOI: 10.1088/1742-6596/1067/5/052005 (cit. on p. 1).

[11] H. Podlech, U. Ratzinger, H. Klein, C. Commenda, H. Liebermann, and A. Sauer. "Superconducting CH structure." In: *Physical Review Special Topics - Accelerators and Beams* 10.8 (2007). DOI: 10.1103/physrevstab.10.080101 (cit. on p. 1).

[12] M. Schwarz et al. "Reference beam dynamics layout for the SC CW heavy ion HELIAC at GSI." In: *Nucl. Instruments Methods Phys. Res. Sect. A Accel. Spectrometers, Detect. Assoc. Equip.* 951.October 2019 (2020), p. 163044. ISSN: 01689002. DOI: 10.1016/j.nima.2019.163044. URL: https://linkinghub.elsevier.com/retrieve/pii/S0168900219314019 (cit. on pp. 1, 48, 69).

[13] M. Gusarova, W. A. Barth, S. Yaramyshev, M. Miski-Oglu, M. Basten, and M. Busch. "Design of the two-gap superconducting re-buncher." In: *Journal of Physics: Conference Series* 1067 (2018), p. 082005. DOI: 10.1088/1742-6596/1067/8/082005 (cit. on pp. 1, 43).

[14] K. Taletskiy, M. Gusarova, W. A. Barth, M. Basten, M. Busch, M. Miski-Oglu, and S. Yaramyshev. "Comparative Study of Low Beta Multi-Gap Superconducting Bunchers." In: *Journal of Physics: Conference Series* 1067 (2018), p. 082006. DOI: 10.1088/1742-6596/1067/8/082006 (cit. on pp. 1, 51).

[15] S. M. Polozov and A. D. Fertman. "High-energy proton beam accelerators for subcritical nuclear reactors." In: *Atomic Energy* 113.3 (2013), pp. 192–200. DOI: 10.1007/s10512-012-9616-4 (cit. on p. 1).

[16] N. Solyak, E. Gianfelice-Wendt, I. G. Gonin, S. Kazakov, V. A. Lebedev, S. Nagaitsev, J.-F. Ostiguy, N. Perunov, G. V. Romanov, and V. P. Yakovlev. "The Concept Design of the CW Linac of the Project X." In: *Proc. 1st Int. Part. Accel. Conf. (IPAC 2010)*. 2010, pp. 654–656 (cit. on p. 1).

[17] A. E. Aksent'ev et al. "Modeling of Proton Beam Dynamics in an Accelerator-Driver at 600–1000 MeV and Investigation of the Electrodynamic Characteristics of Accelerating Cavities." In: *Atomic Energy* 117.5 (2015), pp. 347–356. DOI: 10.1007/s10512-015-9932-6 (cit. on p. 1).

[18] P. N. Ostroumov. "Advances in CW Ion Linacs." In: *Proc. 6th Int. Part. Accel. Conf. (IPAC 2015)*. 2015, pp. 4085–4090. ISBN: 9783954501687. DOI: 10.18429/JACoW-IPAC2015-FRXB3 (cit. on p. 2).

[19] Z.-J. Wang et al. "Beam commissioning for a superconducting proton linac." In: *Physical Review Accelerators and Beams* 19.12 (2016). DOI: 10.1103/physrevaccelbeams.19.120101 (cit. on p. 2).

[20] L. V. Grigorenko et al. "Scientific program of DERICA – prospective accelerator and storage ring facility for radioactive ion beam research." In: *Physics-Uspekhi* 62.7 (2019), pp. 675–690. DOI: 10.3367/ufne.2018.07.038387 (cit. on p. 2).

[21] I. Mardor et al. "The Soreq Applied Research Accelerator Facility (SARAF): Overview, research programs and future plans." In: *The European Physical Journal A* 54.5 (2018). DOI: 10.1140/epja/i2018-12526-2 (cit. on p. 2).

[22] R. E. Laxdal, K. Fong, M. Laverty, A. Mitra, R. Poirier, I. Sekachev, and V. Zvyagintsev. "Recent progress in the superconducting RF Program at TRIUMF/ISAC." In: *Physica C: Superconductivity* 441.1-2 (2006), pp. 13–20. DOI: 10.1016/j.physc.2006.03.096 (cit. on p. 2).

[23] D. Gonnella et al. "Industrialization of the nitrogen-doping preparation for SRF cavities for LCLS-II." In: *Nuclear Instruments and Methods in Physics Research Section A: Accelerators, Spectrometers, Detectors and Associated Equipment* 883 (2018), pp. 143–150. DOI: 10.1016/j.nima.2017.11.047 (cit. on p. 2).

[24] R. Laxdal. "An Overview of Recent Developments in SRF Technology." en-us. In: *Proceedings of the 29th Linear Accelerator Conf.* LINAC2018 (2018). DOI: 10.18429/JACOW-LINAC2018-MO1A02 (cit. on p. 2).

[25] U. Ratzinger and R. Tiede. "Status of the HIIF RF linac study based on H-mode cavities." In: *Nuclear Instruments and Methods in Physics Research Section A: Accelerators, Spectrometers, Detectors and Associated Equipment* 415.1-2 (1998), pp. 229–235. DOI: 10.1016/s0168-9002(98)00389-1 (cit. on pp. 2, 38).

[26] U. Ratzinger. *H-type linac structures*. CAS - CERN Accelerator School : Radio Frequency Engineering, Seeheim, Germany, 8 - 16 May 2000 Nr. 12. CERN, 2000. ISBN: 9789290832843. URL: http://dx.doi.org/10.5170/CERN-2005-003.351 (cit. on pp. 2, 21).

[27] M. Busch, M. Basten, T. Conrad, P. Müller, H. Podlech, M. Schwarz, W. A. Barth, F. D. Dziuba, and M. Miski-Oglu. "Overview on SC CH-Cavity Development." In: *Proc. 10th Int. Particle Accelerator Conf. (IPAC'19)* (Melbourne, Australia). JACoW Publishing, pp. 2822–2825. DOI: 10.18429/JACoW-IPAC2019-WEPRB012. URL: http://accelconf.web.cern.ch/ipac2019/papers/WEPRB012.pdf (cit. on p. 2).

[28] S. Minaev, U. Ratzinger, H. Podlech, M. Busch, and W. Barth. "Superconducting, energy variable heavy ion linac with constant β, multicell cavities of CH-type." In: *Physical Review Special Topics - Accelerators and Beams* 12.12 (2009). DOI: 10.1103/physrevstab.12.120101 (cit. on pp. 2, 17, 39, 41, 42, 47).

[29] T. P. Wangler. *RF Linear Accelerators*. 2nd Edition. WILEY-VCH Verlag GmbH & Co. KGaA, Weinheim, Germany, 2008 (cit. on pp. 5, 7, 8, 10, 73).

[30] Martin Reiser. *Theory and design of charged particle beams*. Second, Updated and Expanded Edition. Germany: Wiley-VCH, 2008. ISBN: 978-3-527-40741-5. DOI: 10.1002/9783527622047 (cit. on pp. 5, 7, 9).

[31] F. Dziuba. "Entwicklung und Test einer supraleitenden 217 MHz CH-Kavität für das Demonstrator-Projekt an der GSI." PhD thesis. Goethe University Frankfurt, Germany, 2016 (cit. on pp. 5, 23, 31).

[32] M. Basten. "Entwicklung und Inbetriebnahme zweier supraleitender 217 MHz CH-Strukturen für das HELIAC-Projekt." PhD thesis. Johann Wolfgang Goethe-Universität, 2019. URL: https://nbn-resolving.org/urn:nbn:de:hebis:30:3-517672 (cit. on pp. 5, 23, 31, 32, 43).

[33] T. Conrad et al. "Cavity Designs for the CH3 to CH11 of the Superconducting Heavy Ion Accelerator HELIAC." In: *Proc. 19th Int. Conf. RF Superconductivity (SRF'19), Dresden, Germany*. 2019, pp. 396–398. DOI: 10.18429/JACoW-SRF2019-TUP005 (cit. on pp. 5, 31, 73).

[34] T. Conrad. *PhD thesis*. to be published. IAP, Goethe University Frankfurt, Germany (cit. on p. 5).

[35] I. M. Kapchinskij and V. V. Vladimirskij. *Limitations of Proton Beam Current in a Strong Focusing Linear Accelerator Associated with the Beam Space Charge*. Proceeding of the conference on High Energy Accelerators and Instrumentation, CERN, 1959 (cit. on p. 7).

[36] M. A. Fraser. "Beam Dynamics Studies of the ISOLDE Postaccelerator for the High Intensity and Energy Upgrade." PhD thesis. School of Physics, Astronomy, Faculty of Engineering, and Physical Sciences, University of Manchester, 2011 (cit. on pp. 8, 44).

[37] J. H. Hähnel. "Development of an IH-type linac for the acceleration of high current heavy ion beams." PhD thesis. IAP, Goethe University Frankfurt, Germany, 2017. URL: http://nbn-resolving.de/urn:nbn:de:hebis:30:3-439833 (cit. on pp. 10, 14, 16).

[38] W. Herr. "Proceedings of the CAS - CERN Accelerator School: Advanced Accelerator Physics Course, Trondheim, Norway, 18-29 Aug 2013." In: (Jan. 27, 2016). DOI: 10.5170/CERN-2014-009. arXiv: 1601.07311v1 [physics.acc-ph] (cit. on p. 10).

[39] I. Hofmann. "Performance of solenoids versus quadrupoles in focusing and energy selection of laser accelerated protons." In: *Phys. Rev. ST Accel. Beams* 16 (4 2013), p. 041302. DOI: 10.1103/PhysRevSTAB.16.041302. URL: https://link.aps.org/doi/10.1103/PhysRevSTAB.16.041302 (cit. on p. 11).

[40] U. Ratzinger, H. Hähnel, R. Tiede, J. Kaiser, and A. Almomani. "Combined zero degree structure beam dynamics and applications." In: *Phys. Rev. Accel. Beams* 22.11 (2019), p. 114801. DOI: 10.1103/PhysRevAccelBeams.22.114801 (cit. on pp. 16, 17, 20, 21).

[41] R. Tiede, U. Ratzinger, H. Podlech, C. Zhang, and G. Clemente. *KONUS Beam Dynamics Designs using H-Mode Cavities*. Proceedings of Hadron Beam 2008, Nashville, Tennessee, USA, WGB11, 2008 (cit. on pp. 16, 21).

[42] M. Otani, T. Mibe, M. Yoshida, K. Hasegawa, Y. Kondo, N. Hayashizaki, Y. Iwashita, Y. Iwata, R. Kitamura, and N. Saito. "Interdigital *H*-mode drift-tube linac design with alternative phase focusing for muon linac." In: *Phys. Rev. Accel. Beams* 19 (4 2016), p. 040101. DOI: 10.1103/PhysRevAccelBeams.19.040101. URL: https://link.aps.org/doi/10.1103/PhysRevAccelBeams.19.040101 (cit. on p. 16).

[43] S. Minaev, U. Ratzinger, and B. Schlitt. "APF or KONUS Drift Tube Structures for Medical Synchrotron Injectors - A Comparison." In: *Proc. 18th Particle Accelerator Conf. (PAC'99), New York, NY, USA*. 1999, pp. 3555–3557 (cit. on p. 16).

[44] K. Yamamoto, T. Hattori, M. Okamura, and S. Yamada. "The Study of APF-IH Linac." In: *Proc. 9th European Particle Accelerator Conf. (EPAC'04), Lucerne, Switzerland*. 2004, pp. 2679–2681 (cit. on p. 16).

[45] R. von Hahn, M. Grieser, D. Habs, E. Jaeschke, C.-M. Kleffner, J. Liebmann, S. Papureanu, R. Repnow, D. Schwalm, and M. Stampfer. "Development of seven-gap resonators for the Heidelberg high current injector." In: *Nuclear Instruments and Methods in Physics Research Section A: Accelerators, Spectrometers, Detectors and Associated Equipment* 328.1 (1993), pp. 270–274. ISSN: 0168-9002. DOI: 10.1016/0168-9002(93)90639-Y. URL: https://www.sciencedirect.com/science/article/pii/016890029390639Y (cit. on p. 17).

[46] H. Podlech, M. Grieser, R. v. Hahn, S. Papureanu, R. Repnow, and D. Schwalm. "The 7-gap-resonator–accelerator for the REX-ISOLDE-experiment at CERN." In: *Nuclear Instruments and Methods in Physics Research Section B: Beam Interactions with Materials and Atoms* 139.1 (1998), pp. 447–450. ISSN: 0168-583X. DOI: 10.1016/S0168-583X(97)00986-5. URL: https://www.sciencedirect.com/science/article/pii/S0168583X97009865 (cit. on p. 17).

[47] H. Podlech. "Entwicklung des 7-Spaltresonator-Beschleunigers für das REX-ISOLDE-Projekt am CERN." PhD thesis. Ruprecht-Karls-Universität Heidelberg, 1999 (cit. on p. 17).

[48] K. W. Shepard and G. P. Zinkann. "A Superconducting Accelerating Structure for Particle Velocities from 0.12- to 0.23-C." In: *IEEE Transactions on Nuclear Science* 30 (4 1983), pp. 3339–3341. ISSN: 1558-1578. DOI: 10.1109/TNS.1983.4336650 (cit. on pp. 17, 33).

[49] L. M. Bollinger. "Superconducting Linear Accelerators for Heavy Ions." In: *Annual Review of Nuclear and Particle Science* 36.1 (1986), pp. 475–503. DOI: 10.1146/annurev.ns.36.120186.002355 (cit. on pp. 17, 33).

[50] L. M. Bollinger, R. C. Pardo, K. W. Shepard, J. M. Bogaty, B. E. Clifft, F. H. Munson, and G. Zinkann. "First operational experience with the positive-ion injector of ATLAS." In: *Nuclear Instruments and Methods in Physics Research Section A: Accelerators, Spectrometers, Detectors and Associated Equipment* 328.1 (1993), pp. 221–230. ISSN: 0168-9002. DOI: https://doi.org/10.1016/0168-9002(93)90631-Q (cit. on pp. 17, 33).

[51] R. W. Hockney and J. W. Eastwood. *Computer Simulation Using Particles*. Taylor & Francis, 1988. ISBN: 9781439822050 (cit. on p. 19).

[52] J.A. Holmes, S. Cousineau, A. Shishlo, and R. Potts. *Space Charge Models for Particle Tracking on Long Time Scales*. Proceedings of PAC2013, Pasadena, USA, WEODB2, 2013 (cit. on p. 19).

[53] Yu. N. Grigoryev, V. A. Vshivkov, and M. P. Fedoruk. *Numerical "Particle-in-Cell" Methods: Theory and Applications*. De Gruyter, Feb. 13, 2012. 252 pp. ISBN: 9783110916706 (cit. on p. 20).

[54] N. Pichoff, M. Lagniel, and S. Nath. *Simulation Results with an Alternate 3D Space Charge Routing, PICNIC*. Proceedings of LINAC98, Chicago, Illinois, USA, MO4042, 1998 (cit. on p. 20).

[55] U. Ratzinger. *Effiziente Hochfrequenz-Linearbeschleuniger für leichte und schwere Ionen*. Habilitation Thesis. Goethe University Frankfurt, Germany, 1998 (cit. on pp. 20, 22).

[56] R. Tiede. "Simulationswerkzeuge für die Berechnung hochintensiver Ionenbeschleuniger." PhD thesis. IAP, Goethe University Frankfurt, Germany, 2009 (cit. on pp. 20, 21).

[57] U. Ratzinger. *The New High Current Ion Accelerator at GSI and Perspectives for Linac Design Based on H-Mode Cavities*. Proceedings of EPAC 2000, Vienna, Austria, TUZF204, 2000 (cit. on p. 21).

[58] R. Tiede, G. Clemente, H. Podlech, U. Ratzinger, and A. Sauer. "LORASR Code Development." In: *Proc. 10th Europ. Particle Accelerator Conf. (EPAC 2006)*. 2006, pp. 886–888. ISBN: 9783954501472 (cit. on p. 21).

[59] C. Kitegi, U. Ratzinger, and S. Minaev. *The IH Cavity for HITRAP*. Proceedings of LINAC 2004, Lübeck, MOP10, 2004 (cit. on p. 21).

[60] L. Groening et al. *Status of the FAIR 70 MeV Proton Linac*. Proceedings of LINAC2012, Tel Aviv, Israel, THPB034, 2012 (cit. on p. 21).

[61] M. A. Fraser, M. Pasini, R. M. Jones, and D. Voulot. *Beam Dynamics Investigation of the 101.28 MHz IH Structure as Injector for the HIE-ISOLDE SC Linac*. arXiv:1006.0183. 2010. eprint: 1006.0183 (cit. on p. 21).

[62] H. Bongers. "Entwicklung der 7-Spalt-Struktur für den Münchner Spaltfragmentbeschleuniger MAFF." PhD thesis. Ludwig Maximilian University of Munich, Germany, 2003. URL: http://nbn-resolving.de/urn:nbn:de:bvb:19-13855 (cit. on p. 21).

[63] Y. R. Lu, S. Minaev, U. Ratzinger, B. Schlitt, and R. Tiede. *The Compact 20 MV IH-DTL fo the Heidelberg Therapy Facility*. Proceedings of LINAC 2004, Lübeck, MOP11, 2004 (cit. on p. 21).

[64] T. Strodl. *Design and Beam Dynamics Simulation for the Ion-Injector of the Austrian Hadron Therapy Accelerator*. Proceedings of EPAC 2006, Edinburgh, Scotland, WEPCH157, 2006 (cit. on p. 21).

[65] D. Raparia, J. Alessi, A. Kponou, A. Pikin, J. Ritter, S. Minaev, U. Ratzinger, A. Schempp, and R. Tiede. *End-to-End Simulations for the EBIS Preinjector*. Proceedings of PAC07, Albuquerque, New Mexico, USA, TUPAS102, 2007 (cit. on p. 21).

[66] D. Noll, L. P. Chau, M. Droba, O. Meusel, H. Podlech, U. Ratzinger, and C. Wiesner. *Beam Dynamics of the FRANZ Bunch Compressor using realistic Fields with a Focus on the Rebuncher Cavities*. Proceedings of IPAC2011, San Sebastián, Spain, MOPS030, 2011 (cit. on p. 21).

[67] M. Schwarz. "Numerische Simulationen zur Strahldynamik eines CH-Driftröhrenbeschleunigers." MA thesis. IAP, Goethe University Frankfurt, Germany, 2014, p. 87 (cit. on p. 21).

[68] S. Alzubaidi et al. "The Frankfurt neutron source FRANZ." In: *Eur. Phys. J. Plus* 131.5 (2016), p. 124. ISSN: 21905444. DOI: 10.1140/epjp/i2016-16124-5. URL: http://link.springer.com/10.1140/epjp/i2016-16124-5 (cit. on p. 21).

[69] X. H. Zhang, Y. J. Yuan, and J. W. Xia. *One Design of Heavy Ion Linac Injector for CSRm*. Proceedings of LINAC2012, Tel Aviv, Israel, TUPB043, 2012 (cit. on p. 21).

[70] A.V. Butenko et al. *Development of the NICE Injection Facility*. Proceedings of IPAC2013, Shanghai, China, THPWO069, 2013 (cit. on p. 21).

[71] B. Koubek et al. "The New Light Ion Injector for NICA." en-us. In: *Proceedings of the 29th Linear Accelerator Conf.* LINAC2018 (2018), China. DOI: 10.18429/JACOW-LINAC2018-TUPO017 (cit. on p. 21).

[72] D. Mäder. "Die CH-Sektion des 17 MeV Injektors für MYRRHA." PhD thesis. IAP, Goethe University Frankfurt, Germany, 2015. URL: http://nbn-resolving.de/urn/resolver.pl?urn:nbn:de:hebis:30:3-372055 (cit. on p. 21).

[73] N. Petry. "Error-studies zum 17MeV Injektor für das MYRRHA-Projekt." In: (2014). bachelor thesis (cit. on p. 21).

[74] D. Uriot, R. Duperrier, and N. Pichoff. *TraceWin*. last requested on July 21st, 2021. CEA, DSM/Irfu/SACM/LEDA, Saclay, France. 2021. URL: http://irfu.cea.fr/Sacm/logiciels/index3.php (cit. on p. 22).

[75] C. Zhang, H. Klein, D. Mäder, H. Podlech, U. Ratzinger, A. Schempp, R. Tiede, and M. Vossberg. "Front-End Linac Design and Beam Dynamics Simulations for MYRRHA." In: paper THPB005. Proc. 26th Linear Accelerator Conf. (LINAC'12), Tel Aviv, Israel, Sept. 2012, pp. 849–851 (cit. on p. 22).

[76] H. Hähnel, C. M. Kleffner, U. Ratzinger, M. Syha, and R. Tiede. "End to End Simulations and Error Studies of the FAIR Proton Linac." In: *Proc. 10th Int. Particle Accelerator Conf. (IPAC'19)* (Melbourne, Australia). JACoW Publishing, pp. 885–888. DOI: 10.18429/JACoW-IPAC2019-MOPTS019. URL: http://accelconf.web.cern.ch/ipac2019/papers/MOPTS019.pdf (cit. on p. 22).

[77] D. Uriot and N. Pichoff. *TraceWin manual*. Université Paris-Saclay, CEA, Département des Accélérateurs, de la Cryogénie et du Magnétisme, 91191, Gif-sur-Yvette, France, Mar. 18, 2021 (cit. on pp. 23, 24).

[78] C. E. Düllmann. "Production and study of chemical properties of superheavy elements." In: *Radiochimica Acta* 107.7 (2019), pp. 587–602. DOI: 10.1515/ract-2019-0012 (cit. on p. 25).

[79] C. A. Levine and G. T. Seaborg. "The occurrence of plutonium in nature." In: *Journal of the American Chemical Society* 73.7 (1951), pp. 3278–3283 (cit. on p. 25).

[80] D. C. Hoffman, F. O. Lawrence, J. L. Mewherter, and F. M. Rourke. "Detection of plutonium-244 in nature." In: *Nature* 234.5325 (1971), pp. 132–134. DOI: 10.1038/234132a0 (cit. on p. 25).

[81] C. J. E. Riedel. *Anorganische Chemie*. Walter de Gruyter, 2011. ISBN: 9783110225662 (cit. on p. 25).

[82] G. Gamow. "Mass defect curve and nuclear constitution." In: *Proc. R. Soc. Lond. A* 126 (1930), pp. 632–644. ISSN: 0950-1207. DOI: 10.1098/rspa.1930.0032 (cit. on p. 25).

[83] C. F. v. Weizsäcker. "Zur Theorie der Kernmassen." In: *Zeitschrift für Physik* 96 (1935), pp. 431–458. ISSN: 1434-6001. DOI: 10.1007/bf01337700 (cit. on pp. 25, 26).

[84] N. Bohr and J. A. Wheeler. "The Mechanism of Nuclear Fission." In: *Phys. Rev.* 56 (5 1939), pp. 426–450. DOI: 10.1103/PhysRev.56.426 (cit. on p. 25).

[85] S. Hofmann. "Baukasten für Superschwergewichte: Synthese und Physik superschwerer Elemente." In: *Physik in unserer Zeit* 43.1 (2012), pp. 30–39 (cit. on pp. 25, 28).

[86] M. y. Ruse. https://github.com/yunruse/binding-energy. 2020 (cit. on pp. 26, 27).

[87] M. Wang, G. Audi, F. G. Kondev, W. J. Huang, S. Naimi, and X. Xu. "The AME2016 atomic mass evaluation (II). Tables, graphs and references." In: 41 (2017), p. 030003. ISSN: 1674-1137. DOI: 10.1088/1674-1137/41/3/030003 (cit. on pp. 26, 27).

[88] M. G. Mayer. "On Closed Shells in Nuclei. II." In: *Phys. Rev.* 75 (12 1949), pp. 1969–1970. DOI: 10.1103/PhysRev.75.1969 (cit. on p. 25).

[89] M. G. Mayer. "Nuclear Configurations in the Spin-Orbit Coupling Model. I. Empirical Evidence." In: *Phys. Rev.* 78 (1 1950), pp. 16–21. DOI: 10.1103/PhysRev.78.16 (cit. on p. 25).

[90] O. Haxel, J. H. D. Jensen, and H. E. Suess. "On the "Magic Numbers" in Nuclear Structure." In: *Phys. Rev.* 75 (11 1949), pp. 1766–1766. DOI: 10.1103/PhysRev.75.1766.2 (cit. on p. 25).

[91] B. H. Nordstrom. "The Elements Beyond Uranium (Seaborg, Glenn T.; Loveland, Walter D.)" In: *Journal of Chemical Education* 69.1 (1992), A34. DOI: 10.1021/ed069pA34. eprint: https://doi.org/10.1021/ed069pA34 (cit. on p. 26).

[92] S. Hofmann and G. Münzenberg. "The discovery of the heaviest elements." In: *Reviews of Modern Physics* 72.3 (), pp. 733–767. ISSN: 0034-6861. DOI: 10.1103/revmodphys.72.733 (cit. on pp. 26, 29).

[93] S. Hofmann. "Synthesis of superheavy elements by cold fusion." In: *Radiochimica Acta* 99.7-8 (2011), pp. 405–428. ISSN: 0033-8230. DOI: 10.1524/ract.2011.1854 (cit. on p. 26).

[94] Yu. Ts. Oganessian. "Synthesis of the heaviest elements in48Ca-induced reactions." In: *Radiochimica Acta* 99.7-8 (2011), pp. 429–439. ISSN: 0033-8230. DOI: 10.1524/ract.2011.1860 (cit. on p. 26).

[95] J.-H. Yoon and C.-Y. Wong. "Relativistic modification of the Gamow factor." In: *Phys. Rev. C* 61 (4 2000), p. 044905. DOI: 10.1103/PhysRevC.61.044905. URL: https://link.aps.org/doi/10.1103/PhysRevC.61.044905 (cit. on p. 26).

[96] S. Hofmann. "Super-heavy nuclei." In: *J. Phys. G: Nucl. Part. Phys.* 42 (2015), p. 114001. ISSN: 0954-3899. DOI: 10.1088/0954-3899/42/11/114001 (cit. on p. 27).

[97] V. Zagrebaev and W. Greiner. "Synthesis of superheavy nuclei: A search for new production reactions." In: *Physical Review C* 78.3 (2008), p. 034610 (cit. on p. 29).

[98] A. K. Nasirov, G. Mandaglio, G. Giardina, A. Sobiczewski, and A. I. Muminov. "Effects of the entrance channel and fission barrier in the synthesis of superheavy element $Z = 120$." In: *Phys. Rev. C* 84 (4 2011), p. 044612. DOI: 10.1103/PhysRevC.84.044612. URL: https://link.aps.org/doi/10.1103/PhysRevC.84.044612 (cit. on p. 29).

[99] A. N. Kuzmina, G. G. Adamian, N. V. Antonenko, and W. Scheid. "Influence of proton shell closure on production and identification of new superheavy nuclei." In: *Phys. Rev. C* 85 (1 2012), p. 014319. DOI: 10.1103/PhysRevC.85.014319. URL: https://link.aps.org/doi/10.1103/PhysRevC.85.014319 (cit. on p. 29).

[100] K. Siwek-Wilczyńska, T. Cap, M. Kowal, A. Sobiczewski, and J. Wilczyński. "Predictions of the fusion-by-diffusion model for the synthesis cross sections of Z=114–120 elements based on macroscopic-microscopic fission barriers." In: *Phys. Rev. C* 86 (1 2012), p. 014611. DOI: 10.1103/PhysRevC.86.014611. URL: https://link.aps.org/doi/10.1103/PhysRevC.86.014611 (cit. on p. 29).

[101] J. Zhang, C. Wang, and Z. Ren. "Calculation of evaporation residue cross sections for the synthesis of superheavy nuclei in hot fusion reactions." In: *Nuclear Physics A* 909 (2013), pp. 36–49. ISSN: 0375-9474. DOI: 10.1016/j.nuclphysa.2013.04.010.

URL: http://www.sciencedirect.com/science/article/pii/S0375947413004958 (cit. on p. 29).

[102] Zu-Hua Liu and Jing-Dong Bao. "Possibility to produce element 120 in the ^{54}Cr+^{248}Cm hot fusion reaction." In: *Phys. Rev. C* 87 (3 2013), p. 034616. DOI: 10.1103/PhysRevC.87.034616. URL: https://link.aps.org/doi/10.1103/PhysRevC.87.034616 (cit. on p. 29).

[103] Yu. Ts. Oganessian and V. K. Utyonkov. "Super-heavy element research." In: 78 (2015), p. 036301. ISSN: 0034-4885. DOI: 10.1088/0034-4885/78/3/036301 (cit. on p. 29).

[104] G. G. Adamian, N. V. Antonenko, A. Diaz-Torres, and S. Heinz. "How to extend the chart of nuclides?" In: *Eur. Phys. J. A* 56.2 (2020), p. 47. DOI: 10.1140/epja/s10050-020-00046-7 (cit. on p. 29).

[105] W. Barth. "Present and future beams for SHE research at GSI." In: *3rd Workshop on Recoil Separator for Superheavy Element Chemistry, GSI, Darmstadt, Germany*. Aug. 27, 2004. URL: https://www-win.gsi.de/tasca/workshops/tasca04/Contributions/5.1_Barth2.pdf (visited on 04/30/2021) (cit. on pp. 29, 39).

[106] U. Ratzinger. "Steps towards an Optimized Linac for SHE Production at GSI." In: *Workshop on The Future of Superheavy Element Research, GSI Darmstadt, Germany*. Feb. 17, 2004. URL: https://www-win.gsi.de/future-she/contributions/contributions/Ratzinger.pdf (visited on 04/30/2021) (cit. on pp. 29, 39).

[107] Holger Podlech. "Superconducting versus normal conducting cavities." In: *CERN Yellow Report CERN-2013-001, pp.151-170* (Mar. 26, 2013). DOI: 10.5170/CERN-2013-001.151. arXiv: 1303.6552 [physics.acc-ph] (cit. on pp. 29, 30).

[108] Y. Zhang, P. Chu, and Z. Q. He. "Phase and Amplitude Tuning Algorithms for the FRIB Superconducting Cavities." In: *Proc. 6th Int. Particle Accelerator Conf. (IPAC'15), Richmond, VA, USA*. 2015, pp. 1207–1210. DOI: 10.18429/JACoW-IPAC2015-MOPWI025 (cit. on p. 31).

[109] L. Ristori et al. "Development and Performance of 325 MHz Single Spoke Resonators for Project X." In: *Proc. 16th Int. Conf. RF Superconductivity (SRF'13), Paris, France* (Sept. 2013). paper FRIOB02, pp. 1187–1192 (cit. on p. 31).

[110] P. N. Ostroumov et al. "R&D Towards CW Ion Linacs at ANL." In: *Proc. 26th Linear Accelerator Conf. (LINAC'12), Tel Aviv, Israel*. 2012, pp. 461–463 (cit. on p. 33).

[111] R. Janssens. "The ATLAS facility." In: *Scholarpedia* 5.9 (2010). revision #91866, p. 9731. DOI: 10.4249/scholarpedia.9731 (cit. on p. 33).

[112] J. Wei et al. "The FRIB Project – Accelerator Challenges and Progress." In: *Proc. 12th Int. Conf. on Heavy Ion Accelerator Technology (HIAT'12), Chicago, IL, USA*. 2012, pp. 8–19 (cit. on p. 33).

[113] E. Fagotti et al. "Operational Experience in PIAVE-ALPI Complex." In: *Proc. 11th Int. Conf. on Heavy Ion Accelerator Technology (HIAT'09), Venice, Italy*. 2009, pp. 208–212 (cit. on p. 33).

[114] G. Bisoffi et al. "Hardware Commissioning of the Refurbished ALPI Linac at INFN-LNL to Serve as SPES Exotic Beam Accelerator." In: *Journal of Physics: Conference Series* 1350 (2019), p. 012091. DOI: 10.1088/1742-6596/1350/1/012091. URL: https://doi.org/10.1088%2F1742-6596%2F1350%2F1%2F012091 (cit. on p. 33).

[115] S. C. Jeong. "Progress of the RAON Heavy Ion Accelerator Project in Korea." In: *Proc. of International Particle Accelerator Conference (IPAC'16), Busan, Korea, May 8-13, 2016* (Busan, Korea). International Particle Accelerator Conference 7. Geneva, Switzerland: JACoW, 2016, pp. 4261–4265. ISBN: 978-3-95450-147-2. DOI: 10.18429/JACoW-IPAC2016-FRYAA01. URL: http://jacow.org/ipac2016/papers/fryaa01.pdf (cit. on p. 33).

[116] A. Roy. "Superconducting Linac and Associated Developments at IUAC Delhi." In: *Proc. 26th Linear Accelerator Conf. (LINAC'12), Tel Aviv, Israel*. 2012, pp. 763–767 (cit. on p. 33).

[117] S. Gosh et al. "Developmental and Operational Aspects of Nb QWR Based Heavy Ion LINAC System at IUAC Delhi." In: *Proc. 27th Linear Accelerator Conf. (LINAC'14) Geneva, Switzerland*. 2014, pp. 640–642 (cit. on p. 33).

[118] Z. Y. Yao et al. "Operating Experience on Cavity Performance of ISAC-II Superconducting Heavy Ion Linac." In: *Proc. of International Conference on RF Superconductivity (SRF'17), Lanzhou, China, July 17-21, 2017* (Lanzhou, China). International Conference on RF Superconductivity 18. Geneva, Switzerland: JACoW, 2018, pp. 527–530. ISBN: 978-3-95450-191-5. DOI: 10.18429/JACoW-SRF2017-TUPB064. URL: http://jacow.org/srf2017/papers/tupb064.pdf (cit. on p. 33).

[119] M. L. Lozano, N. Bidault, E. Fadakis, M. A. Fraser, E. Matli, and J. A. Rodriguez. "Characterization of the Beam Energy Spread at the REX/HIE-ISOLDE Linac." In: *Proc. 9th International Particle Accelerator Conference (IPAC'18), Vancouver, BC, Canada, April 29-May 4, 2018* (Vancouver, BC, Canada). International Particle Accelerator Conference 9. Geneva, Switzerland: JACoW Publishing, 2018, pp. 787–789. ISBN: 978-3-95450-184-7. DOI: 10.18429/JACoW-IPAC2018-TUPAF042. URL: http://jacow.org/ipac2018/papers/tupaf042.pdf (cit. on p. 33).

[120] A. Sublet et al. "Status of HIE-ISOLDE SC Linac Upgrade." In: *Proc. 6th International Particle Accelerator Conference (IPAC'15), Richmond, VA, USA, May 3-8, 2015* (Richmond, VA, USA). International Particle Accelerator Conference 6. Geneva, Switzerland: JACoW, 2015, pp. 3151–3154. ISBN: 978-3-95450-168-7. DOI: 10.18429/JACoW-IPAC2015-WEPHA021. URL: http://jacow.org/ipac2015/papers/wepha021.pdf (cit. on p. 33).

[121] C. Marchand, P. Bosland, G. Devanz, O. Piquet, P.-E. Bernaudin, R. Ferdinand, Y. Gomez, D. Longuevergne, and G. Olry. "Performances of Spiral2 Low and High Beta Cryomodules." In: *Proc. 17th Int. Conf. RF Superconductivity (SRF'15), Whistler, Canada*. 2015, pp. 967–972 (cit. on p. 33).

[122] P. Dolegieviez, R. Ferdinand, X. Ledoux, H. Savajols, and F. Varenne. "Status of the SPIRAL2 Project." In: *Proc. 10th International Particle Accelerator Conference (IPAC'19), Melbourne, Australia, 19-24 May 2019* (Melbourne, Australia). International Particle Accelerator Conference 10. Geneva, Switzerland: JACoW Publishing, 2019, pp. 844–847. ISBN: 978-3-95450-208-0. DOI: 10.18429/JACoW-IPAC2019-MOPTS005. URL: http://jacow.org/ipac2019/papers/mopts005.pdf (cit. on p. 33).

[123] N. Sakamoto et al. "Development of Superconducting Quarter-Wave Resonator and Cryomodule for Low-Beta Ion Accelerators at RIKEN Radioactive Isotope Beam Factory." In: *Proc. SRF'19* (Dresden, Germany). International Conference on RF Superconductivity 19. JACoW Publishing, Geneva, Switzerland, 2019, pp. 750–757. ISBN: 978-3-95450-211-0. DOI: 10.18429/JACoW-SRF2019-WETEB1. URL: http://jacow.org/srf2019/papers/weteb1.pdf (cit. on p. 33).

[124] N. Pichoff et al. "The SARAF-LINAC Project 2019 Status." In: *Proc. 10th International Particle Accelerator Conference (IPAC'19), Melbourne, Australia, 19-24 May 2019* (Melbourne, Australia). International Particle Accelerator Conference 10. Geneva, Switzerland: JACoW Publishing, 2019, pp. 4352–4355. ISBN: 978-3-95450-208-0. DOI: 10.18429/JACoW-IPAC2019-THPTS116. URL: http://jacow.org/ipac2019/papers/thpts116.pdf (cit. on p. 33).

[125] Ian G. Brown et al. *The physics and technology of ion sources*. Ed. by Ian G. Brown. 2nd. John Wiley & Sons, 2004. ISBN: 3-527-40410-4 (cit. on p. 33).

[126] I. Peter. *FAIR - Das Universum im Labor*. FAIR – Facility for Antiproton and Ion Research in Europe GmbH; Planckstraße 1, 64291 Darmstadt, July 2020. URL: https://www.gsi.de/fileadmin/oeffentlichkeitsarbeit/Broschueren/FAIR_Broschuere_20200702_web.pdf (cit. on p. 37).

[127] W. Barth, W. Bayer, L. Dahl, L. Groening, S. Richter, and S. Yaramyshev. "Upgrade program of the high current heavy ion UNILAC as an injector for FAIR." In: *Nuclear Instruments and Methods in Physics Research Section A: Accelerators, Spectrometers, Detectors and Associated Equipment* 577.1-2 (2007), pp. 211–214. DOI: 10.1016/j.nima.2007.02.054 (cit. on p. 38).

[128] W. Barth et al. "High brilliance uranium beams for the GSI FAIR." In: *Physical Review Accelerators and Beams* 20.5 (2017). DOI: 10.1103/physrevaccelbeams.20.050101 (cit. on p. 38).

[129] U. Ratzinger. "The 70 MeV p-Injector Design for FAIR." In: *AIP Conference Proceedings*. AIP, 2005. DOI: 10.1063/1.1949539 (cit. on p. 38).

[130] C. M. Kleffner et al. "Status of the FAIR pLinac." In: *Proc. 8th Int. Part. Accel. Conf. (IPAC 2017)*. 2017, pp. 2208–2210. ISBN: 9783954501823 (cit. on p. 38).

[131] W. Barth, A. Adonin, S. Appel, P. Gerhard, M. Heilmann, F. Heymach, R. Hollinger, W. Vinzenz, H. Vormann, and S. Yaramyshev. "Heavy ion linac as a high current proton beam injector." In: *Physical Review Special Topics - Accelerators and Beams* 18.5 (2015). DOI: 10.1103/physrevstab.18.050102 (cit. on p. 38).

[132] A. A. Adonin and R. Hollinger. "Beam brilliance investigation of high current ion beams at GSI heavy ion accelerator facility." In: *Review of Scientific Instruments* 85.2 (2014), 02A727. DOI: 10.1063/1.4833931 (cit. on p. 38).

[133] U. Ratzinger. "Commissioning of the new GSI high current linac and HIF related RF linac aspects." In: *Nuclear Instruments and Methods in Physics Research Section A: Accelerators, Spectrometers, Detectors and Associated Equipment* 464.1-3 (2001), pp. 636–645. DOI: 10.1016/s0168-9002(01)00155-3 (cit. on p. 38).

[134] L. Groening et al. "Benchmarking of measurement and simulation of transverse rms-emittance growth." In: *Physical Review Special Topics - Accelerators and Beams* 11.9 (2008). DOI: 10.1103/physrevstab.11.094201 (cit. on p. 38).

[135] F. Herfurth et al. "HITRAP – Heavy, highly charged Ions at Rest: Status and experimental Opportunities." In: *Journal of Physics: Conference Series* 388.14 (2012), p. 142009. DOI: 10.1088/1742-6596/388/14/142009 (cit. on p. 38).

[136] F Herfurth et al. "The HITRAP facility for slow highly charged ions." In: *Physica Scripta* T166 (2015), p. 014065. DOI: 10.1088/0031-8949/2015/t166/014065 (cit. on p. 38).

[137] I. Hofmann, J. Meyer ter Vehn, X. Yan, A. Orzhekhovskaya, and S. Yaramyshev. "Collection and focusing of laser accelerated ion beams for therapy applications." In: *Physical Review Special Topics - Accelerators and Beams* 14.3 (2011). DOI: 10.1103/physrevstab.14.031304 (cit. on p. 38).

[138] S. Busold et al. "Shaping laser accelerated ions for future applications – The LIGHT collaboration." In: *Nuclear Instruments and Methods in Physics Research Section A: Accelerators, Spectrometers, Detectors and Associated Equipment* 740 (2014), pp. 94–98. DOI: 10.1016/j.nima.2013.10.025 (cit. on p. 38).

[139] Daniel Koser. "Development of a 108MHz 4-Rod CW RFQ-Design for High Duty Cycle Accelerationof Heavy Ion Beams at the GSI-HLI." PhD thesis. IAP, Goethe University Frankfurt, Germany, 2020 (cit. on p. 38).

[140] L. Groening et al. "Upgrade of the UNILAC for FAIR." In: *Proc. 13th Int. Conf. on Heavy Ion Accelerator Technology (HIAT'15)*. Sept. 2015, pp. 139–143 (cit. on p. 39).

[141] R. Tiede. *LORASR input file "CW.txt" of the CW-Linac design by S. Minaev*. personal communication. Oct. 7, 2014 (cit. on p. 39).

[142] M. Busch. "Modellmessungen und Simulationsrechnungen zur Optimierung der supraleitenden CH-Struktur." Diploma thesis. IAP, Goethe University Frankfurt, Germany, 2009 (cit. on p. 40).

[143] S. Lauber et al. "Reconstruction of the longitudinal phase portrait for the SC CW heavy ion HELIAC at GSI." In: *J. Phys. Conf. Ser.* 1350 (2019), p. 012073. ISSN: 1742-6588. DOI: 10.1088/1742-6596/1350/1/012073. URL: https://iopscience.iop.org/article/10.1088/1742-6596/1350/1/012073 (cit. on p. 41).

[144] F. Dziuba et al. "First cold tests of the superconducting CW demonstrator at GSI." In: *25th Russ. Part. Accel. Conf. RuPAC 2016*. 2016, pp. 83–85. ISBN: 9783954501816 (cit. on p. 42).

[145] M. Pasini and R. E. Laxdal. *ISAC-II: Beam Studies with Multicharge Beams*. Design Note TRI-DN-01-08. 4004 Wesbrook Mall, Vancouver, B.C. V6T 2A3, Canada: TRIUMF, Apr. 2001 (cit. on p. 44).

[146] M. Heilmann et al. "Further upgrade measures at new GSI CW-linac demonstrator setup." In: *Proc. 7th Int. Part. Accel. Conf. (IPAC 2016)*. 2016, pp. 892–895. ISBN: 9783954501472 (cit. on p. 44).

[147] G. Gulbekian. "Efficient Production of Intensive Beams of Rare Isotopes." In: *Workshop on The Future of Superheavy Element Research, GSI Darmstadt, Germany*. Feb. 17, 2004. URL: https://www-win.gsi.de/future-she/contributions/contributions/Gulbekian.pdf (visited on 04/30/2021) (cit. on p. 46).

[148] P. Strehl. *Beam instrumentation and diagnostics*. Particle Acceleration and Detection. Berlin: Springer, 2006. ISBN: 978-3-540-26401-9, 978-3-540-26404-0. DOI: 10.1007/3-540-26404-3 (cit. on p. 51).

[149] P. N. Ostroumov, S. Cogan, K. Fukushima, S. Lidia, T. Maruta, A. S. Plastun, J. Wei, J. Wong, T. Yoshimoto, and Q. Zhao. "Heavy ion beam acceleration in the first three cryomodules at the Facility for Rare Isotope Beams at Michigan State University." In: *Phys. Rev. Accel. Beams* 22 (4 2019), p. 040101. DOI: 10.1103/PhysRevAccelBeams.22.040101. URL: https://link.aps.org/doi/10.1103/PhysRevAccelBeams.22.040101 (cit. on p. 51).

[150] M. Bozzolan. "BPM Time of Flight Measurements for Setting-up the RF Cavities of the CERN Linac4." In: *Proc. 29th Linear Accelerator Conference (LINAC'18), Beijing, China, 16-21 September 2018* (Beijing, China). Linear Accelerator Conference 29. Geneva, Switzerland: JACoW Publishing, 2019, pp. 879–881. ISBN: 978-3-95450-194-6. DOI: 10.18429/JACoW-LINAC2018-THPO084. URL: http://jacow.org/linac2018/papers/thpo084.pdf (cit. on p. 51).

[151] J. Kennedy and R. Eberhart. "Particle swarm optimization." In: *Proceedings of ICNN'95 - International Conference on Neural Networks*. Vol. 4. 1995, pp. 1942–1948. DOI: 10.1109/ICNN.1995.488968 (cit. on p. 56).

[152] Y. Shi and R. Eberhart. "A modified particle swarm optimizer." In: *1998 IEEE International Conference on Evolutionary Computation Proceedings. IEEE World Congress on Computational Intelligence (Cat. No.98TH8360)*. 1998, pp. 69–73. DOI: 10.1109/ICEC.1998.699146 (cit. on p. 56).

[153] R. Tiede. *Description of the New Machine Error Setting and Analysis Tools Available for the LORASR Beam Dynamics Code*. IAP Internal Note IAP-DYNA-070807. IAP, Goethe University Frankfurt, Germany, 2007 (cit. on p. 62).

[154] R. Tiede. *Description of the Lens Rotation Error Settings Implemented to the LORASR Beam Dynamics Code*. IAP Internal Note IAP-DYNA-211107. Institut für Angewandte Physik, Goethe-Universität Frankfurt am Main, 2007 (cit. on p. 62).

[155] V. Anferov. "Energy degrader optimization for medical beam lines." In: *Nuclear Instruments and Methods in Physics Research Section A: Accelerators, Spectrometers, Detectors and Associated Equipment* 496.1 (2003), pp. 222–227. ISSN: 0168-9002. DOI: 10.1016/S0168-9002(02)01625-X. URL: https://www.sciencedirect.com/science/article/pii/S016890020201625X (cit. on p. 69).

[156] M. Amberg, M. Busch, F.D. Dziuba, H. Podlech, U. Ratzinger, K. Aulenbacher, W.A. Barth, V. Gettmann, and S. Mickat. "The Fast Piezo-Based Frequency Tuner for SC CH-Cavities." In: *Proc. 27th Linear Accelerator Conf. (LINAC'14)* (Geneva, Switzerland). JACoW Publishing, 2014, pp. 214–216 (cit. on p. 73).

[157] M. Basten et al. "RD Status of the New Superconducting CW Heavy Ion LINAC@GSI." In: *Proc. 17th Int. Conf. RF Superconductivity (SRF'15)* (Whistler, Canada). 2015, pp. 258–261 (cit. on p. 73).

[158] M. Schwarz, D. Bade, J. Corbet, and H. Podlech. "LINAC-multitool - an Open Source Java-toolkit." In: *Proc. 29th Linear Accelerator Conference (LINAC'18), Beijing, China, 16-21 September 2018*. Linear Accelerator Conference 29. Geneva, Switzerland: JACoW Publishing, 2019, pp. 217–219. ISBN: 978-3-95450-194-6. DOI: 10.18429/JACoW-LINAC2018-MOPO101. URL: http://jacow.org/linac2018/papers/mopo101.pdf (cit. on p. 85).

[159] D. Bade. "LINAC-Multitool - Ein Java-basiertes Programm zur F&E von Teilchenbeschleunigern." MA thesis. IAP, Goethe University Frankfurt, Germany, 2019 (cit. on p. 85).

[160] J. Corbet. *LINAC-Multitool: Establishing an optimized workflow for the analysis of bead pull measurement data*. Bachelor Thesis. IAP, Goethe University Frankfurt, Germany, 2019 (cit. on p. 85).

[161] R. Tiede, D. Mäder, N. F. Petry, H. Podlech, U. Ratzinger, and C. Zhang. "Improvements of the LORASR Code and their Impact on Current Beam Dynamics Designs." In: *Proc. 27th Linear Accelerator Conf. (LINAC 2014)*. 2014, pp. 913–915 (cit. on p. 86).

[162] CST. *Computer Simulation Technology*. URL: http://www.cst.com (cit. on p. 88).

[163] R. Bringhurst. *The elements of typographic style. Version 4.0: 20th anniversary edition*. 4. ed. Point Roberts, WA [u.a.]: Hartley Marks, 2013. 398 pp. ISBN: 9780881792119 (cit. on p. 110).

No one can whistle a symphony.
It takes a whole orchestra to play it.

— Halford E. Luccock

ACKNOWLEDGMENTS

I would like to take this opportunity to thank all the people and organizations who made it possible for me to conduct the research summarized in this thesis and who have been very supportive over the years as I have faced a variety of scientific challenges.

First and foremost, I want to express my sincere gratitude to my supervisor Prof. Dr. H. Podlech for the opportunity to do my doctorate in his group, for the support in all phases of this thesis and for the trust he has placed in me.

Many thanks also to my second reviewer Prof. Dr. U. Ratzinger, who has always supported me with inspiring and helpful advice and a wealth of experience.

I would like to express my gratitude to all my colleagues at the Institute of Applied Physics who supported me and my work during these studies in many ways. In particular, I would like to mention Prof. Dr. O. Kester, Dr. M. Iberler, Dr. M. Baschke, Dr. D. Koser, Dr. M. Basten, Dr. A. Ateş, N. Petry, K. Kümpel, S. Lamprecht, T. Conrad, D. Bade, J. Corbet, P. Müller, S. Zimmermann, D. Bänsch, T. Metz, C. Wagner, J. Kaiser, E. Sunar, M. Syha and H. Wang. I would like to especially emphasize Dr. M. Busch for his continuous support as well as Dr. M. Schütt for the successful research stay in South Korea and further important academic travels.

Regarding the beam dynamics codes LORASR and TraceWin, I thank Dr. H. Hähnel and Dr. R. Tiede for their support and fruitful discussions.

Always prompt help in administrative matters I received from L. Quist, A. Hergt, M. Scholz, T. Harji, K. Brost and K. Schäfer. Thank you.

I would also like to thank my colleagues at GSI Darmstadt, HI Mainz and JGU Mainz for many years of good cooperation. I like to name in particular Prof. Dr. W. Barth, as well as Dr. S. Yaramyshev, Dr. M. Miski-Oglu, Dr. F. Dziuba, Dr. C. Burandt, Dr. T. Kürzeder, V. Gettmann, S. Lauber and J. List.

I deeply appreciate the level-headed, open-minded and supportive manner of Dr. G. Hahn, as well as of Dr. S. H. Nam, Dr. J.-G. Hwang, Dr. B.-J. Lee, M. Choi and G. N. Jung from Korea Institute of Radiological & Medical Sciences respectively Pohang Accelerator Laboratory during my research stay in the Republic of Korea.

I received fundamental support from the German Federal Ministry of Education and Research (BMBF, contr. nos. 05P15RFRBA and 05P18RFRBA), the Polytechnic Foundation of Frankfurt am Main (*main doctus* scholarship) and the Helmholtz Research Academy Hesse for FAIR (HFHF). Further support was granted by the German Academic Exchange Service (DAAD), the National Research Foundation of Korea (NRF), the Helmholtz International Center for FAIR (HIC for FAIR), the EU Framework Program HORIZON2020 (Grant IDs 662186 (MYRTE) and 730871 (ARIES)), the Wilhelm and Else Heraeus Foundation and the Hermann Willkomm Foundation. I would like to thank the organizers and sponsors of the International Particle Accelerator Conference (IPAC) series, the International Conference on RF Superconductivity (SRF) series and the Linear Accelerator Conference (LINAC) series for awarding me student grants at multiple international conferences.

Last but not least, I would like to thank my family, Marie and all other friends not mentioned here by name for their loving support, both inside and outside the university.

Most plots in this thesis were created using free and open-source software (FOSS), mainly the Python IDE Spyder[3] and the plotting library Matplotlib[4] with the perceptually uniform and CVD[5]-safe colormap *Plasma*.

This document was typeset using `classicthesis`[6] developed by André Miede and Ivo Pletikosić. The style was inspired by Robert Bringhurst's book on typography "*The Elements of Typographic Style*" [163].

3 https://spyder-ide.org/
4 https://matplotlib.org/
5 color vision deficiency
6 https://bitbucket.org/amiede/classicthesis/